

A FAR-ULTRAVIOLET ATLAS OF LOW-RESOLUTION *HST* SPECTRA OF T TAURI STARS¹

Hao Yang

JILA, University of Colorado and NIST, Boulder, CO 80309-0440

haoyang@jilau1.colorado.edu

Gregory J. Herczeg

Max-Planck-Institut für extraterrestrische Physik, Postfach 1312, 85741 Garching, Germany

gregoryh@mpe.mpg.de

Jeffrey L. Linsky

JILA, University of Colorado and NIST, Boulder, CO 80309-0440

jlinsky@jilau1.colorado.edu

Alexander Brown

CASA, University of Colorado, Boulder, CO 80309-0389

Alexander.Brown@colorado.edu

¹Based on observations made with the NASA/ESA *Hubble Space Telescope*, obtained from the data archive at the Space Telescope Science Institute. STScI is operated by the Association of Universities for Research in Astronomy, Inc. under NASA contract NAS 5-26555. This work also contains results from Chandra projects 09200763 and 10200804 supported by SAO grants GO8-9024X and GO9-0020B to the University of Colorado. This work was supported in part by NASA Swift grants NNX09AL59G and NNX10AK88G, and Smithsonian Institution Chandra grants GO8-9024X, GO9-0020B, GO0-11042X, and GO1-12031X to the University of Colorado.

Christopher M. Johns-Krull

Department of Physics and Astronomy, Rice University, 6100 Main Street, Houston, TX
77005

`cmj@rice.edu`

Laura Ingleby

Department of Astronomy, University of Michigan, 830 Dennison Building, 500 Church
Street, Ann Arbor, MI 48109

`lingleby@umich.edu`

Nuria Calvet

Department of Astronomy, University of Michigan, 830 Dennison Building, 500 Church
Street, Ann Arbor, MI 48109

`ncalvet@umich.edu`

Edwin Bergin

Department of Astronomy, University of Michigan, 830 Dennison Building, 500 Church
Street, Ann Arbor, MI 48109

`ebergin@umich.edu`

Received _____; accepted _____

ABSTRACT

We present a far-ultraviolet (FUV) spectral atlas consisting of spectra of 91 pre-main sequence stars. Most stars in this sample were observed with the Space Telescope Imaging Spectrograph (STIS) and Advanced Camera for Surveys (ACS) on the *Hubble Space Telescope* (*HST*). A few archival spectra from *International Ultraviolet Explorer* (*IUE*) and the Goddard High Resolution Spectrograph (GHRS) on the *HST* are included for completeness. We find strong correlations among the O I $\lambda 1304$ triplet, the Si IV $\lambda\lambda 1394/1403$ doublet, the C IV $\lambda 1549$ doublet, and the He II $\lambda 1640$ line luminosities. For classical T Tauri stars (CTTSs), we also find strong correlations between these lines and the accretion luminosity, suggesting that these lines form in processes related to accretion. These FUV line fluxes and X-ray luminosity correlate loosely with large scatters. The FUV emission also correlates well with H α , H β , and Ca II K line luminosities. These correlations between FUV and optical diagnostics can be used to obtain rough estimates of FUV line fluxes from optical observations. Molecular hydrogen (H₂) emission is generally present in the spectra of actively accreting CTTSs but not the weak-lined T Tauri stars (WTTSs) that are not accreting. The presence of H₂ emission in the spectrum of HD 98800 N suggests that the disk should be classified as actively accreting rather than a debris disk. We discuss the importance of FUV radiation, including the hydrogen Ly α line, on the photoevaporation of exoplanet atmospheres. We find that the Ca II/C IV flux ratios for more evolved stars are lower than those for less evolved accretors, indicating preferential depletion of refractory metals into dust grains.

Subject headings: atlases — accretion, accretion disks — stars: pre-main sequence — ultraviolet: stars

1. INTRODUCTION

Classical T Tauri stars (CTTSs) are young, pre-main sequence stars characterized by excess line and continuum emission produced by a circumstellar disk and accretion from the disk onto the central star. Their non-accreting counterparts, weak-lined (or naked) T Tauri stars (WTTSs or NTTSs), generally do not display excess infrared (IR) emission, indicating the absence of a dusty disk. The spectra of WTTSs also lack strong line and excess hydrogen continuum emission, indicating that no accretion is present. In recent years, large photometric and spectroscopic surveys of T Tauri stars (TTSs) at wavelengths spanning from X-rays through the millimeter range, utilizing many line and continuum diagnostics, have demonstrated that (i) most young stars lose their disks within a few million years (e.g. Haisch et al. 2001; Andrews & Williams 2005; Hernández et al. 2008), (ii) stars that do not show excess mid-IR emission, which indicates the presence of warm dust, also lack accretion signatures (White & Ghez 2001; Muzerolle et al. 2003; Fedele et al. 2010), (iii) accretion processes are similar for central objects with masses ranging from a solar mass down to brown-dwarf masses (Muzerolle et al. 2005; Mohanty et al. 2005), (iv) the Initial Mass Function peaks at $\sim 0.5 M_{\odot}$ (Luhman et al. 2003, 2010), and (v) all CTTSs and WTTSs are coronally active (e.g., Feigelson et al. 2005; Güdel et al. 2007). These surveys, often focusing on stars within the nearby Taurus Molecular Cloud, have provided the foundation for understanding the early evolution of our own and other planetary systems.

Although TTSs have been surveyed at most accessible wavelengths, the characterization of far-ultraviolet (FUV) emission remains sparse. FUV spectra of young stars offer intriguing diagnostics of accretion, magnetic activity, outflows, and disks (e.g., Johns-Krull et al. 2000; Herczeg et al. 2002; Lamzin et al. 2004; Johns-Krull & Herczeg 2007). The emission produced by these processes plays a particularly important role in the evolution of circumstellar disks where planetary systems originate. FUV emission produced by stellar

chromospheric* activity and accretion shocks causes the disk to photoevaporate at large distances during the accretion phase, removing gas in the outer disks and perhaps constricting the time a disk survives (e.g., Gorti & Hollenbach 2009) and thus the time available for planet formation. FUV emission also modulates the chemistry at the disk surface by dissociating H₂O, CO, and HCN molecules and ionizing some species (C, Si, S) with low-ionization potentials (Aikawa et al. 2002; Bergin et al. 2003, 2004; Bethell & Bergin 2009). Some important gas tracers, such as the prominent [O I] 63 μ m line, have fluxes that depend directly on the FUV luminosity of the central star (e.g., Voitke et al. 2009; Kamp 2011). The ionization at the disk surface may play a role in allowing the disk to accrete via the magneto-rotationally instability (Perez-Becker & Chiang 2011). Once accretion has ceased, FUV emission is produced only by stellar magnetic activity. Measuring FUV emission also provides important constraints on the amount of EUV emission produced by young stars, which controls the survival timescale for any small amount of gas in a remnant disk (Alexander et al. 2005, 2006). After a disk has dissipated and planets have formed, the EUV and FUV emission causes some evaporation of the atmospheres of “hot Jupiters” (Lecavelier des Etangs et al. 2003; Linsky et al. 2010) and remains an important input for atmospheric chemistry in planetary atmospheres (e.g., Yelle 2004).

The *International Ultraviolet Explorer* (*IUE*) pioneered UV spectroscopy of pre-main sequence (PMS) stars, revealing bright emission in many lines, including He II λ 1640, C IV λ 1549, C II λ 1335, O I λ 1304, and the rich fluorescent spectrum of molecular hydrogen (H₂) (Brown et al. 1981). Valenti et al. (2000), Johns-Krull et al. (2000), and Valenti et al.

*For convenience, in the paper we refer both chromospheric emission lines (e.g., Ca II and Balmer lines) and lines emitted from the transition region (e.g., C IV and Si IV lines) as chromospheric.

(2003) published the PMS archive of *IUE* far- and near-UV spectra of 137 TTSs and 97 Herbig Ae/Be (HAeBe) stars, although only 50 of the TTSs were observed in the FUV. Together, this trilogy has laid out the foundation for our understanding of UV radiation fields from young stars, including the strength and the physical processes responsible for such emission.

However, the *IUE* survey of FUV emission from young stars was limited to the FUV-brightest CTTSs and included only three WTTSs, of which the latest spectral type is K0. The survey is also limited by S/N, evident in the low detection rate of H₂ line emission (13/32 CTTSs, Valenti et al. 2000) despite subsequent observations showing that such emission is common to all CTTSs (Herczeg et al. 2006; Ingleby et al. 2009). Analysis of the location and kinematics of the gas that produces the FUV emission lines was also limited by the large aperture ($\sim 10'' \times 20''$) and low spectral resolution (6 Å) of the *IUE* SWP camera.

Since the launch of the *Hubble Space Telescope* (*HST*) 20 years ago, the Goddard High Resolution Spectrograph (GHRS), Space Telescope Imaging Spectrograph (STIS) and the Advanced Camera for Surveys (ACS) prisms have observed over 80 PMS stars. Analyses of small subsets of these observations (< 10 objects, and often only one) have been used to address specific issues, including (i) the details of Ly α -pumped H₂ emission (e.g. Ardila et al. 2002; Herczeg et al. 2002, 2004, 2006), (ii) the H₂ emission resulting from collisions with energetic electrons (Bergin et al. 2004; Herczeg et al. 2004; Ingleby et al. 2009; France et al. 2010b), (iii) the influence of Ly α emission and X-ray emission on disk chemistry (Bergin et al. 2003, 2004; Bethell & Bergin 2009), (iv) the ionization state of outflows (Johns-Krull & Herczeg 2007), (v) the possibility of metal depletion in the accretion flow (Herczeg et al. 2002; France et al. 2010a), and (vi) the origin of emission from ionized gas (e.g. Ardila et al. 2002; Herczeg et al. 2002; Lamzin et al. 2004). In a more complete analysis of ~ 40 CTTSs and WTTSs observed with the ACS PR130L prism,

Ingleby et al. (2009) placed very low limits on the amount of remnant H₂ gas around WTTSs by finding that H₂ continuum emission is always detected from CTTSs but never from WTTSs, including those that retain debris disks but are no longer accreting. Recently, Ingleby et al. (2011) analyzed ten new ACS/SBC spectra of Chamaeleon I and II regions along with archival HST data of ~45 TTSs and showed that the FUV emission decreases with age, correlating with the decline of accretion in CTTSs as they become nonaccretors. Of the many FUV observations of CTTSs and WTTSs obtained by *HST*, only a small subsample, those obtained with the E140M grating of STIS ($R \sim 40,000$), have also been published in a spectral atlas, the CoolCat catalog * (Ayres 2005).

In this paper, we present an atlas of FUV spectra and emission line fluxes of all PMS stars observed by STIS, GHRS and ACS. This atlas surveys the strength of FUV emission from WTTSs and includes CTTSs with a wide range of accretion rates and masses. Since *HST* will not be able to obtain large amounts of FUV observations to correlate with extensive ground-based observations, we search for correlations between the currently available FUV observations and optical observations of the same sample to serve as a good guide for future studies. With these correlations, large volumes of optical data sets (e.g., Barentsen et al. 2011) can be used to infer the FUV emission of more distant or heavily extinguished TTSs. In § 2, we describe sample selection and the details of FUV observations with various instruments. In § 3, we present flux measurements of strong atomic features, the correlation between the atomic line luminosities and stellar properties, and identification of molecular hydrogen features. In § 4, we discuss estimating FUV emission from optical observations, evolution of FUV emission from PMS stars, importance of FUV emission on the photoevaporation of exoplanet atmospheres, and the interesting special case of HD 98800 N. A summary of our findings is provided in § 5.

*<http://casa.colorado.edu/~ayres/CoolCAT>

2. SAMPLE SELECTION AND OBSERVATIONS

Table 1 lists the 91 PMS stars in our sample and information concerning their observations. The majority of the observations were obtained with the STIS G140L grating (24 stars) and ACS/SBC PR130L prism (54 stars). The observations also include eight stars observed with the STIS E140M grating and two stars observed only with the GHRS G160M grating. Three stars, CY Tau (ID: 9), DR Tau (ID: 38), and GM Aur (ID: 40) were observed with both the ACS/SBC PR130L prism and the STIS E140M grating. T Tau (ID: 14) was observed with both the STIS G140L and E140M gratings. For completeness, six stars that were observed with *IUE* but not with *HST* are included in our sample. Among the six stars, MML 34 (ID:73) was not published in the Valenti et al. (2000) *IUE* atlas of PMS stars.

2.1. Sample Description

Table 2 summarizes the basic properties of stars in our sample. The sample consists of a collection of CTTSs* and WTTSs that have been observed with *HST* in the FUV. The high-resolution STIS spectra and the IUE spectra are biased toward stars that are brightest in the UV. Most of the stars are members of the Taurus Molecular Cloud. A small number are members of other regions, such as the TW Hya association (TWA), or are isolated. (A few tight binaries in the sample are further discussed in Appendix A.) The spectral types in the sample range from F2 to M8, which corresponds to masses of $\sim 2 M_{\odot}$ down to $\sim 0.1 M_{\odot}$. Accretion rates of the objects range from 10^{-12} to $10^{-7} M_{\odot} \text{ yr}^{-1}$.

All members of a molecular cloud are assumed to have the same distance: 140 pc for

*For the purposes of this paper, the terms CTTSs and WTTSs are used to apply to objects with both stellar and brown dwarf masses.

Taurus (Bertout et al. 1999; Loinard et al. 2007), 125 pc for Ophiuchus (Lombardi et al. 2008; Loinard et al. 2008), 145 pc for Upper Sco (de Zeeuw et al. 1999), 130 pc for Corona Australis (Neuhäuser & Forbrich 2008), 150 pc for Lupus I (Comerón et al. 2009), 175 pc for Cha I (see discussion in Luhman et al. 2008), 250 pc for Perseus (Enoch et al. 2006), 440 pc for Ori OB1c, and 450 pc for λ Ori (Dolan & Mathieu 2001). TW Hya (ID: 57) has a *Hipparcos* distance of 56 pc from Perryman et al. (1997), and the brown dwarf 2M1207A (ID: 69) has a parallax distance of 52.4 pc from Ducourant et al. (2007). The remaining TW Hya association (TWA) members have kinematic distances calculated by Mamajek (2005).

In most cases, the spectral types and photospheric and accretion luminosities were adopted from the references listed in Table 2, with some changes to account for updated distance measurements. For cases where the accretion rate is obtained from White & Ghez (2001), we convert the accretion rate into the accretion luminosity using the listed accretion rate, stellar radius, and stellar mass and the formula $\dot{M}_{acc} = 1.25 L_{acc} R_* / (GM_*)$ from Gullbring et al. (1998). In several cases, e.g., DR Tau (ID: 38), DP Tau (ID: 36) and DL Tau (ID: 26), the photospheric luminosity is not listed because the detected optical/IR emission is dominated by emission from the accretion shocks and the disk. These objects are frequently listed as “continuum” objects in the literature, though some have spectral types that have been obtained by measuring heavily veiled photospheric absorption lines in high-resolution optical spectra.

Extinctions are obtained from the listed references in Table 2. The uncertainty in extinction estimates is often not listed. For the purposes of this paper, we assume that most extinctions are uncertain by ~ 0.5 mag, which introduces a factor of ~ 6 , ~ 4 , and ~ 2 error in luminosities of the O I $\lambda 1304$, C IV $\lambda 1549$, and Ca II K lines, respectively. In some cases, such as members of the TWA, the extinction is negligible and does not contribute

any uncertainty to the line luminosities.

For a few stars in the sample, two or four exposures were taken consecutively by STIS, as indicated by the third-to-last column (N = number of exposures) in Table 1. We examined the individual spectra and did not find substantial short-term variability between successive exposures. We therefore coadded the spectra, weighted by exposure time, and then measured the line fluxes. For AU Mic, there are ~ 180 spectra available in the archive, and we picked 32 spectra from two consecutive days and coadded them.

For the four stars observed with both STIS G140L and ACS or both STIS G140L and E140M gratings, we used the FUV luminosities from the STIS G140L spectra for correlations, because of its better balance between spectral resolution and signal-to-noise. The total FUV luminosities measured from *IUE* are typically unreliable for CTTSs and WTTSs because the noise is high relative to the continuum and the detector often saturates at longer wavelengths.

2.2. Observations with Different Instruments

Table 3 summarizes the properties of the different instruments that were used to obtain the data for this survey, including aperture size, wavelength coverage, spectral resolution R ($= \lambda/\delta\lambda$) and typical C IV flux levels below which the measurement uncertainty becomes greater than 10% (see discussion in §4.1 and Appendix B). Below, we describe briefly the characteristics of each instrument as well as its data access and reduction procedures.

2.2.1. *HST GHRIS*

GHRIS was a first-generation *HST* FUV spectrograph. The GHRIS observations of CTTSs were obtained at moderate resolution through the large ($\sim 2''$) aperture and covered only ~ 35 Å regions, which were centered on the bright C IV doublet at 1550 Å and the bright Si IV doublet at 1400 Å. The GHRIS spectra of eight CTTSs were published by Ardila et al. (2002). We obtained these spectra from the Multimission Archive at the Space Telescope Science Institute (MAST; <http://archive.stsci.edu>). The spectra were reduced using the standard On The Fly Reprocessing (OTFR) pipeline at MAST (Swade et al. 2001) before being downloaded from the archive.

2.2.2. *HST STIS E140M*

The second-generation *HST* instrument, STIS, is an echelle spectrograph that offers high spectral resolution ($R = \lambda/\delta\lambda \sim 40,000$) across the 1170–1700 Å wavelength region in the E140M mode. When observing the young stars, the echelle mode of STIS used very small apertures ($0.2'' \times 0.06''$, $0.2'' \times 0.2''$, and $0.5'' \times 0.5''$), which minimizes any contribution from spatially extended emission. STIS E140M spectra of six CTTSs were published by Herczeg et al. (2006). The eight young stars observed with STIS E140M grating in our sample were obtained from the CoolCAT spectral atlas of cool stars (Ayres 2005).

2.2.3. *HST STIS G140L*

The G140L grating on STIS is a low-resolution ($R \sim 2000$) spectrograph that covers the 1150–1700 Å wavelength region. A total of 24 CTTSs were observed with STIS/G140L, typically with the $52'' \times 2''$ aperture. The spectra were reduced using the standard OTFR pipeline before being downloaded from the MAST archive. Most STIS G140L spectra in

our sample were published by Calvet et al. (2004) and Bergin et al. (2004).

2.2.4. *HST ACS/SBC PR130L*

The Solar Blind Channel (SBC) on ACS observed 54 TTSs with the PR130L prism, which yields a spectral resolution of $R \sim 170$ near 1350 Å but decreasing to $R \sim 60$ at 1650 Å. Each visit consists of an image with one of several long-pass filters and a prism spectrum. The 2D images were obtained from the MAST archive, as calibrated by the OTFR pipeline. We extracted the spectra using custom IDL routines, with a wavelength solution and extraction window based on the positional offsets between the location of the object in the image and the slitless spectrum (Larsen 2006). The counts spectrum was obtained using a 9-pixel extraction window centered on the spectral trace and was then converted to a flux spectrum based on the sensitivity function calculated by Larsen (2006). Of the 54 ACS/SBC PR130L spectra, 30 spectra were published by Ingleby et al. (2009).

2.2.5. *FUSE and IUE Spectra of TW Hya and AU Mic*

The Far Ultraviolet Spectroscopic Explorer (*FUSE*) covers the 912–1184 Å region with $R \sim 20,000$ and a $30'' \times 30''$ aperture (Moos et al. 2000). We present fluxes from *FUSE* spectra of TW Hya (ID: 57), a CTTS, and AU Mic (ID: 90), a WTTS, to provide readers with an estimate of the total FUV flux down to 912 Å for both sources. *FUSE* observed AU Mic on 26 August 2000 and 10 October 2001 for a total of 43.8 ks (Redfield et al. 2003; France et al. 2007). *FUSE* observed TW Hya on 3 June 2000 and again, with a much deeper spectrum, on 20–21 February 2003 (Johns-Krull & Herczeg 2007).

We present the *IUE* LWR-LO spectra of TW Hya and AU Mic to show typical near-UV fluxes of TTSs from 1700 to 3000 Å. *IUE* observed TW Hya on 29 October 1979 for 3600 s.

IUE observed AU Mic at multiple epochs. We averaged the spectra from 18 exposures on 4–6 August 1980 for a total of 32.4 ks.

2.2.6. *Optical Spectra*

We supplemented the HST/FUV observations with ground-based optical spectra of many of the same targets, obtained with the Double Spectrograph (Oke & Gunn 1982) on the Hale 5m Telescope on Mount Palomar in January and December 2008. The optical spectra span most of the 3200–8700 Å range with $R \sim 1000$. Fluxes in H α , H β , and Ca II H lines were extracted for this paper, with an uncertainty in flux calibration of 10%. The full dataset will be described in a future paper.

2.2.7. *X-Ray Luminosity*

In Table 2, we include the available measurements of X-ray luminosity for the UV sample obtained from both the literature and new dedicated observations. Many of the measurements for stars in the Taurus-Auriga star formation region are taken from the XMM-Newton XEST survey (Güdel et al. 2007).

New Chandra ACIS observations of LkCa 4 (ID: 8), DE Tau (ID: 12), GM Aur (ID: 40), TWA 13 N and S (ID: 61 and 62), TWA 8 S and N (ID: 65 and 66), and TWA 9 N and S (ID: 67 and 68) and Swift observations of TWA 7 (ID: 55) and TWA 3 S and N (ID: 58 and 59) were analyzed for this paper and the derived X-ray luminosities are included in Table 2. The Chandra and Swift data were modeled using XSPEC (Version 12.5) and fluxes and luminosities over the energy range 0.3–10.0 keV were measured.

3. Results

Figure 1 shows the STIS G140L spectra for a few stars in our sample, and plots of the full sample are available in the online version of this paper. Figure 2 compares typical FUV spectra of CTTSs and WTTSs. The pattern of FUV emission from the WTTSs is similar to that of magnetically active dwarf stars, including bright emission in O I λ 1304, C II λ 1335, Si IV λ 1400, C IV λ 1549, and He II λ 1640 lines and no detectable continuum emission. (The ACS spectra of WTTSs appear to show continuum, but that is due to a combination of low spectral resolution and strong line emission and is not real .) The CTTSs show strong emission in these same lines, though the origin is likely an accretion-heated photosphere or funnel flow (Calvet & Gullbring 1998) rather than chromospheric emission. The CTTSs also show bright H₂ emission lines and, in many cases, continuum emission (France et al. 2011).

In the following subsections, we measure flux in emission lines and discuss several exceptional cases where at least some of the FUV emission is spatially extended in outflows rather than on or very near the star.

3.1. Line Flux Measurements

We measured line fluxes by subtracting the continuum estimated with a linear fit with wavelength, and subsequently integrating the emission remaining in the line. The uncertainties in our measurements are dominated by uncertainty in the placement of the continuum, with the error determined by measuring new fluxes after increasing and decreasing the estimated continuum by 20%. This arbitrary change in continuum estimate is an conservative estimate and makes only a minor contribution to the uncertainty in line luminosities, which are usually dominated by uncertainties in the FUV extinction.

Statistical errors propagated through the data reduction pipelines are also included. For previously published flux measurements, we adopt the values from Valenti et al. (2000), Pagano et al. (2000), Ardila et al. (2002), and Calvet et al. (2004). Table 4 lists the line flux measurements and associated uncertainties for the stars in our sample.

Accurately measuring line fluxes in the very low-resolution ACS/SBC PR130L spectra is complicated by line-blending and uncertain continuum subtraction. We created artificial ACS spectra by degrading 21 different STIS G140L spectra to the resolution of PR130L. Line fluxes were then measured in both the real and the degraded G140L spectra, and we show the differences between the two sets of measurements in Table 5. The line fluxes have differences of $< 10\%$ in most cases but can reach as high as 30% , especially for the C IV $\lambda 1549$ doublet where the ACS/SBC PR130L spectral resolution is lowest.

The FUV emission is typically consistent with a point source centered on the star, with some notable exceptions. Figure 3 compares the spectra of T Tau (ID: 14) obtained with a narrow, on-source extraction from the STIS G140L grating (degraded to the IUE spectral resolution) and with the IUE spectrum, obtained with a large aperture. The *IUE* spectrum shows much brighter H₂ emission than the on-source G140L spectrum. Bright H₂ emission is spatially extended in the G140L slit, consistent with emission produced in the outflow (see detailed analysis in Walter et al. (2003) and Saucedo et al. (2003)). DP Tau (ID: 36) was faintly detected in the F165LP acquisition image. Strong H₂ emission is located approximately at the stellar position and is spatially extended by $\sim 0''.11$ in the cross-dispersion direction (-30°) and $\sim 0''.14$ in the dispersion direction. Some faint emission may also be more extended in the spectral image. The ACS SBC acquisition image for 2MASS J04141188+2811535 (ID: 3), an accreting M6.5 brown dwarf, was obtained with the F140LP long-pass filter, which covers a spectral region that includes C IV and H₂ lines and the continuum. A second source is located $0''.34$ from the primary at a PA of $\sim 176^\circ$

with a brightness three times fainter than the primary.

3.2. Correlation of the Line Luminosities with Stellar Properties

Correlations of line luminosities with stellar properties can be used to infer the physical origin of the emission. Johns-Krull et al. (2000) found for a small sample of 12 CTTSs a correlation between mass accretion rate and C IV emission and ascribed the emission to accretion-related processes. In addition, Johns-Krull et al. (2000) and Ardila et al. (2002) suggested also from small samples that FUV emission from WTTSs is weaker than that from CTTSs. With a sample of 56 stars, Ingleby et al. (2011) found that both the C IV and the He II line luminosities correlate well with accretion luminosity, supporting the connection between the line formation and accretion. In this subsection, we look for correlations between FUV line emission and available optical chromospheric activity indicators: Ca II K, H α , and H β lines.

We convert the FUV line fluxes to line luminosities using the distances listed in Table 2, after correcting the line fluxes for interstellar extinction following the Cardelli et al. (1989) extinction law with a total-to-selective extinction coefficient of R_V of 3.09. The uncertainty in A_V and the extinction law contribute significant uncertainties to the line luminosities. The extinction law for dense molecular clouds typically has $R_V \sim 5.5$, indicating significant grain growth (e.g. Weingartner & Draine 2001; Indebetouw et al. 2005). However, these large values of R_V typically correspond to $A_V > 10$ (also see discussion in Calvet et al. (2004)), while most stars in our sample have $A_V < 2$. Some lines-of-sight may also pass through a disk atmosphere, which would likely have different grains and a different extinction curve than the ISM. Although we choose $R_V = 3.09$, selecting other values would be reasonable. A full assessment of different extinction laws would require recalculating A_V and is beyond the scope of this work. The extinction-corrected FUV luminosity between

1250–1700 Å is listed in the last column of Table 4.

Figures 4, 5, and 6 show the C IV $\lambda 1549$ line luminosity against $H\alpha$, $H\beta$, and Ca II K line luminosities, respectively. For WTTSs, the C IV $\lambda 1549$ luminosities are well correlated with the optical line luminosities. For CTTSs, the C IV $\lambda 1549$ and the optical line luminosities are loosely correlated, which is expected from non-simultaneous observations because the accretion rate varies significantly with time. The best linear-fit parameters and median scatters from the fits are listed in Table 6 where we also list the parameters for linear fits with a fixed slope of one. We find that the X-ray emission is loosely correlated with the C IV $\lambda 1549$ emission, as shown in Figure 7. Variability in both the FUV and X-ray emission from CTTSs should introduce a large scatter in any correlation. While the CTTSs show much stronger C IV emission than the WTTSs, mainly due to accretion, the CTTSs and the WTTSs display a similar range of X-ray emission.

Figures 8 and 9 show correlations of C IV $\lambda 1549$ line luminosity and total FUV luminosity with the accretion luminosity for 37 CTTSs, respectively. The C IV emission of CTTSs includes contributions from chromospheric activity and accretion, both of which can be variable. The large scatter in the fits likely results from variability between the C IV and accretion rate measurements obtained at different times, uncertainty in extinction, and perhaps different physical processes contributing to the C IV line flux. Nonetheless, the correlations between C IV and both the accretion and FUV luminosities are definitely real.

Figure 10 shows correlations among various FUV emission line luminosities for both CTTSs and WTTSs. The same linear fit applies to both CTTSs and WTTSs, which demonstrates that FUV line flux ratios do not depend on whether the emission is produced by chromospheric activity or by accretion. The line fluxes depend on the emission measure versus temperature. The same linear fit to the CTTSs and WTTSs in each panel indicate that the shape of the emission measure distribution must be similar for both chromospheric

activity and accretion.

3.3. Molecular Hydrogen Emission from CTTSs

Warm H₂ gas ($\sim 2,500$ K) can be excited to the B and C electronic states by strong Ly α and other UV emission lines and subsequently decays to the ground (X) electronic state. This H₂ fluorescence is commonly detected from CTTSs, likely originating at the surfaces of the circumstellar disks and from outflows shocking the surrounding molecular environment (e.g., Walter et al. 2003; Saucedo et al. 2003; Herczeg et al. 2006). The spectral window between 1430 Å and 1510 Å is particularly useful because it includes many strong H₂ lines but few stellar emission lines. Limited by the low spectral resolution in ACS data, we could only identify the H₂ features in the 1430–1510 Å wavelength region for the stars in our sample, and noted “Yes” or “No” in the second-to-last column of Table 4 to indicate whether or not the spectrum shows H₂ emission. A more quantitative assessment and analysis of H₂ emission from ACS/SBC spectra was provided by Ingleby et al. (2009).

Our results agree with Ingleby et al. (2009) who find that CTTSs generally display H₂ emission in the the 1430–1510 Å region while WTTSs do not. Of the 31 stars in our sample previously classified as WTTS, only one (HD 98800 N, ID: 63) shows the H₂ emission feature (see §4.2). For the near-equal mass binary system 2MASS J16141107-2305362 (Metchev & Hillenbrand 2009), the S component (ID: 83) produces stronger FUV emission lines but lacks detectable H₂ emission, characteristic of WTTSs. The N component (ID: 84), produces strong Ly α -pumped H₂ lines and excess FUV continuum emission, as expected for a CTTS. The system may therefore be a CTTS/WTTS binary.

4. DISCUSSION

4.1. Prescriptions for Calculating FUV luminosities

FUV emission affects the disk by photoevaporation and by driving a complex chemistry at the disk surface, including photodissociation of some molecules and ionization of atomic species with low first ionization potential energies. The FUV radiation field is needed as an input for disk modeling to help interpret emission line tracers of gas in the disk.

In this subsection, we offer prescriptions for estimating accretion and chromospheric emission produced in the FUV from optical emission lines. Figures 10 and 11 show that the luminosities of C IV $\lambda 1549$, O I $\lambda 1304$, C II $\lambda 1335$, Si IV $\lambda\lambda 1394/1403$ lines, and He II $\lambda 1640$ lines and of the FUV (1250–1700 Å bandpass) are all strongly correlated with each other. As a consequence, a measurement of only one of these parameters is needed to estimate the total FUV flux. Figures 4, 5, and 6 show that the C IV and, by implication, the FUV luminosities correlate with H α , H β , and Ca II K line emission for both CTTSs and WTTSs. Emission in H α , H β , and Ca II K lines can therefore be used to obtain rough estimates for the FUV emission using equations and parameters listed in Table 6.

Two exemplary cases, TW Hya (CTTS) and AU Mic, are selected for this analysis, because they have complete, high S/N spectra from the Lyman limit to 1700 Å (see Table 7) and the photospheric emission is negligible in this bandpass for both stars. The spectra from 912–1200 Å were observed by *FUSE* for these two stars but not for most of the stars presented in this atlas. However, because the correlation between FUV lines is very tight (Figure 10), we infer that these two template spectra can be scaled to the strength of C IV (or optical line) flux for each object.

For example, when a measurement of accretion luminosity is available, the equation $\log(L_{\text{FUV}}) = -1.670 + 0.836 \log(L_{\text{acc}})$ can be used to obtain an estimate of the total

FUV luminosity. Similarly, the equations $\log(L_{\text{FUV}}) = -1.632 + 0.760 \log(L_{\text{H}\alpha})$ and $\log(L_{\text{FUV}}) = -2.323 + 0.766 \log(L_{\text{H}\beta})$ provide estimates of total FUV luminosity from $\text{H}\alpha$ and $\text{H}\beta$ measurements of CTTSs, respectively. In Table 6, we give the relationships of optical diagnostics, L_{acc} , and other FUV lines, with respect to C IV emission or L_{FUV} .

This prescription outlined above provides estimates of the FUV luminosity, with an accuracy of $\sim 0.5 - 1.0$ dex. The luminosities refer only to chromospheric and accretion-related processes and do not include photospheric emission. For stars with spectral types G and earlier, the photospheric emission provides a significant fraction of the total FUV luminosity and needs to be included in such calculations. Since the FUV spectra of late-type stars are dominated by line emission, calculating excitation rates in discrete electronic transitions of various molecules, including H_2 and CO, may require use of real spectral templates rather than assumptions about a smooth distribution of flux with wavelength.

This discussion of FUV radiation fields neglects the $\text{Ly}\alpha$ $\lambda 1216$ line. The $\text{Ly}\alpha$ line is presumed to be strong, as much as 75-90% of the total FUV luminosity from CTTSs (see Table 7), based on direct detections from a few objects (Herczeg et al. 2004; Yang et al. 2011; France et al. 2011) and indirect detections from strong H_2 lines (e.g. Herczeg et al. 2006; Ingleby et al. 2009). The total stellar $\text{Ly}\alpha$ flux is not directly observable because neutral hydrogen in the ISM and circumstellar environment scatters $\text{Ly}\alpha$ photons out of our line of sight to the star. The $\text{Ly}\alpha$ line is also not covered by the ACS/SBC PR130L prism. For WTTSs, correlations with L_X provided by Wood et al. (2005) could be used to infer $\text{Ly}\alpha$ luminosities. For both CTTSs and WTTSs, reconstruction of the stellar $\text{Ly}\alpha$ line is needed to properly estimate the $\text{Ly}\alpha$ flux seen by the circumstellar gas.

4.2. Evolution of FUV Emission for PMS Stars

Figures 12 and 13 show the FUV luminosity, L_{FUV} , and its ratio to the bolometric luminosity, $L_{\text{FUV}}/L_{\text{bol}}$, versus spectral type, respectively. For stars with spectral type later than K0, where the extinction estimates are more accurate, the FUV luminosity, L_{FUV} , of CTTSs is $\sim 10^{-2.75}L_{\text{bol}}$, with a scatter of ~ 0.65 dex, and the FUV luminosity of WTTSs is $\sim 10^{-4.06}L_{\text{bol}}$ with a scatter of ~ 0.43 dex. The higher FUV luminosities of CTTSs are due to accretion and related processes. Many of the WTTSs in our sample are thought to be older than their CTTS counterparts and have smaller bolometric luminosities and, consequently, even lower absolute FUV luminosities. The WTTSs in Taurus generally show stronger FUV emission than the WTTSs of similar spectral types in TWA and other regions. Our sample is biased in age and mass. Many of the K stars are from the ~ 2 Myr old (Palla & Stahler 2000) Taurus Molecular Cloud, and all M dwarfs are located in the 10 Myr (Barrado Y Navascués 2006) TWA, while G stars are typically older field dwarfs.

Ingleby et al. (2011) showed for their sample that the FUV luminosity between 1230 and 1800 Å correlates well with L_{acc} and both quantities decrease with age from 1 Myr to 1 Gyr. As shown in Figure 9, despite the scatter, we also find that the FUV emission of CTTSs clearly scales with the accretion rate. The highest accretion rates likely occur in outbursts during the Class 0 and I stages (Dunham et al. 2010), when the accretion and any FUV emission are mostly or entirely obscured from our view by dense envelopes. During these stages, the mean accretion rate is likely higher than measured for CTTSs, with a correspondingly higher FUV luminosity. The CTTS stage includes stars with accretion rates of that range over 2 orders of magnitude at a given mass, with some suggestion that older CTTSs have lower accretion rates. As the accretion rate decreases, so does the FUV luminosity. The chromospheric emission provides the lower limit on the strength of FUV emission from young stars.

4.3. Importance of Far-UV Spectra for Photoevaporation and Photochemistry of Close-in Exoplanet Atmospheres

The discovery and characterization of Jupiter mass exoplanets close to their host stars by ground-based telescopes and the CoRoT and Kepler missions raises many questions concerning the photochemistry of their atmospheres and mass loss due to hydrodynamic and magnetohydrodynamic processes. For example, the well studied exoplanet HD 209458b, which has a semimajor axis of 0.045 AU and a 3.52 day orbital period about its G0 V host star (Knutson et al. 2007), receives a radiative flux 13,400 times that of Jupiter. Like many other hot Jupiters, HD 209458b is inflated with a radius 1.25 times that of Jupiter, which could be due in part to external heating. While the visual and near-UV (NUV) stellar flux dominates the external heating of the lower atmospheres of hot Jupiters, the stellar FUV, EUV, and X-ray fluxes will control ionization and dissociation processes in the outer atmosphere and drive mass loss through heating of the exosphere.

Models of hydromagnetic mass loss from hot Jupiters (Yelle 2004; Tian et al. 2005; García Muñoz 2007; Murray-Clay et al. 2009) assume that the mass loss is driven by absorption by H₂ and H I in the upper atmosphere. The inclusion of photoabsorption of UV photons by C, N, and O can greatly increase the mass loss rate (García Muñoz 2007). The FUV emission can also affect atmospheric chemistry by photodissociation of many molecules, including H₂, H₂O, and CH₄. Biologically-important O₂ is dissociated by $\lambda < 2500 \text{ \AA}$ radiation leading to the formation of O₃.

Realistic assessments of the FUV flux must be included in theoretical models to explain the large mass flux for HD 209458b (Linsky et al. 2010) and to accurately describe the photochemistry in the atmospheres of young or forming planets. During the active accretion phase, a Jovian-mass planet will migrate inward to where the disk is truncated. In this phase, the optically thick disk may shield the planet from direct irradiation from

the central star. Once the disk dissipates, the planets see bright emission from the central star. Ribas et al. (2005) have collected the available UV and X-ray fluxes (between 1 and 1200 Å) as a function of age for solar-mass stars older than 50 Myr and provided scaling laws for the age dependence of the flux in different bands. They found that the emission in all wavelength intervals decreases by a few orders of magnitude following power laws from 0.1 to 7 Gyr, and higher energy emissions display steeper decreases. Ingleby et al. (2011) extended this study to younger stars and found that the Ribas et al. (2005) power laws are valid for stars between 15 and 100 Myr for X-ray and FUV (1230–1800 Å bandpass) luminosities. The FUV emission of WTTSs in our sample have similar strengths as that reported in Ingleby et al. (2011) and thus a few orders of magnitude stronger than the much older solar analogs in Ribas et al. (2005).

The above analysis excludes Ly α emission, which dominates the total FUV emission from both WTTSs and CTTSs (Wood & Karovska 2004; Herczeg et al. 2004). For CTTSs, this emission can be scattered deeper into the disk than other FUV photons (Bethell & Bergin 2009, Herczeg 2006). However, most planets are located beyond the dust sublimation radius and will be shielded from any optically-thick radiation from the disk. Once the disk dissipates, any hot Jupiter will see the total FUV emission from the star, including Ly α . The incident radiation field for WTTSs should include both the 1250–1700 Å emission discussed here and the Ly α radiation, which can be estimated from the stellar X-ray luminosity (Wood et al. 2005).

4.4. HD 98800 N: a debris disk or an accretion disk?

HD 98800 (K5) is a quadruple system that consists of two spectroscopic binaries separated by 0''8 (Boden et al. 2005). An IR excess from the N component indicates the presence of a dust disk (Gehrz et al. 1999; Koerner et al. 2000; Prato et al. 2001). Both the

IR spectral energy distribution and high-resolution sub-mm images indicate a hole in the dust distribution in the disk, with an inner truncation radius of 3.5–6 AU from the central binary (Furlan et al. 2007; Akeson et al. 2007; Andrews et al. 2009). A low-resolution 3300–5500 Å spectrum (Figure 14) that includes both components shows no evidence for accretion, with $\log \dot{M} < -9.9$ (or $\log \dot{L}/L_{\odot} < -2.5$), following Herczeg & Hillenbrand (2008). Salyk et al. (2009) did not detect any CO rovibrational emission in a high-resolution M-band ($\sim 5 \mu\text{m}$) spectrum of HD 98800 N (ID: 63). Prior to this work, the absence of any gas or accretion signatures suggested that the disk should have been classified as a debris disk rather than a transition (or cold) disk with ongoing accretion.

The emission at 1420 and 1500 Å from HD 98800 N is Ly α -pumped H₂ emission (Figure 15). The general rise shortward of 1700 Å is likely explained, at least in part, by a combination of Ly α -pumped H₂ emission and H₂ emission following a collision with energetic electrons (Herczeg et al. 2002; Bergin et al. 2004; France et al. 2010b). Ingleby et al. (2009) detected this H₂ emission in the FUV spectrum of every classical T Tauri star but not for any star with a debris disk. FUV H₂ line emission has been previously detected around one debris disk, AU Mic (France et al. 2007). However, that emission produced in cold H₂ gas is faint, and could not explain the H₂ emission seen in the PR130L spectrum.

Our detection of bright FUV H₂ emission from HD 98800 N demonstrates that warm gas persists in its disk. This detection suggests that HD98800 N has ongoing accretion with a rate below previous detection limits. Ingleby et al. (2011) describes a similar case, RECX 11, which lacks any detectable excess U-band emission but has accretion detectable in several diagnostics, including the FUV.

4.5. Evidence for Depletion of Refractory Elements in Accretion Flows

Figure 16 compares the Ca II K and C IV line luminosities for WTTSs, CTTSs, and more evolved CTTSs. As defined here, these more evolved CTTSs include members of the TW Hya and Upper Sco Associations, the cold (or transitional) disks GM Aur, DM Tau, and LkCa 15, the settled disk V836 Tau, and SCH J0518, which is located off of the main Taurus fields in a region with a low disk fraction.

For WTTSs, the Ca II and C IV lines are both produced by chromospheric emission, while for CTTSs, these lines are produced by a combination of chromospheric emission and accretion-related processes. The correlation between Ca II and C IV line luminosities observed at different times is very tight for WTTSs, indicating that variability is moderate. Generally, extinctions for WTTSs are lower and less uncertain than for CTTSs, and that may contribute to the tighter relationship between Ca II and C IV line emission. Larger scatter is expected and observed for CTTSs because accretion can be highly variable and the extinctions are more uncertain.

The more evolved CTTSs almost all have low Ca II/C IV luminosity ratios relative to most other CTTSs in our sample. The exception is TWA 3N (ID: 59), which is only weakly accreting (Herczeg et al. 2009) at a low enough rate that emission in both lines could be dominated by the chromosphere. The low Ca II/C IV line ratios could be explained by the preferential depletion of refractory metals into grains that have settled into a dead zone below the surface layers in the disk and do not take part in accretion (Gammie 1996). For the 10 Myr old CTTSs, TW Hya and 2M1207 (TWA 27), the weakness in FUV Si lines and, for 2M1207, Mg II h & k lines, relative to C lines has been interpreted as possible evidence for Si depletion into dust grains in the disk (Herczeg et al. 2002; France et al. 2010a). This interpretation has some support from high-resolution X-ray spectroscopy of more evolved CTTSs that show anomalously high Ne/Fe and Ne/O abundance ratios, with line ratios

suggesting an origin in the accretion flow (Kastner et al. 2002; Stelzer & Schmitt 2004; Günther et al. 2007). Similarly, certain metals can be depleted in outflows (e.g. Nisini et al. 2005; Garcia Lopez et al. 2010), which may indicate that the gas in the wind launch region is similarly depleted in refractory elements.

The low Ca II/C IV ratios for the cold disks in Taurus support the idea that refractive metals are also depleted in the accretion flow in these disks. The disks have undergone some evolution relative to the typical disks seen in Taurus. The depletion of Ca may suggest that refractive metals have settled into large grains or planetessimals. This analysis is restricted to Ca because the Si lines are difficult to separate from H₂ emission in the low-resolution ACS PR130L spectra.

4.6. Spatially Extended Jets in the FUV

H₂ emission from young stars can be spatially extended and related to outflows, as is seen prominently around T Tau (see discussion in § 3.1; Walter et al. 2003; Saucedo et al. 2003). The stellar emission strengths of the Si IV and C IV lines are similar in both observations, but the larger *IUE* aperture detects much stronger H₂ emission, as expected for spatially extended emission (see Figure 3).

In most spectra presented here, the H₂ emission is centered on-source, with no significant contribution from spatially extended outflows. The lack of spatially extended emission does not necessarily indicate that the H₂ emission traces the disk. High angular-resolution spectra of RU Lup, T Tau, DG Tau, and DF Tau show that the on-source emission includes at least some emission from an outflow (Herczeg et al. 2006). Off-source H₂ emission is detected from two other sources, DP Tau and 2MASS J04141188+2811535. An asymmetric bipolar jet (HH 231) is associated with DP Tau (Mundt & Eisloffel 1998),

so results from the DP Tau spectrum are not included in any of the correlations presented in §3.2. Near-IR AO images of 2MASS J04141188+2811535 indicate that the object lacks a near-IR companion of similar brightness (Adam Kraus, private communication). The secondary component is likely an H₂ jet, which is also consistent with the presence of a weak emission between the primary and secondary positions and with the presence of bright optical forbidden lines (Herczeg & Hillenbrand 2008).

5. SUMMARY

In this paper, we present a FUV spectral atlas of 91 CTTSs and WTTSs, as observed by the GHRS, STIS, and ACS instruments on *HST*, including some observations by *IUE* and *FUSE*. We find that FUV line luminosities are well correlated with each other over a large range of luminosity. The same correlation applies to both CTTSs and WTTSs, which indicates that the emission measure has a similar distribution versus temperature for chromospheric activity and for accretion. Accretion significantly increases the strength of these lines and the total FUV luminosity, with $\log \frac{L_{\text{FUV}}}{L_{\text{bol}}} \sim -2.7$ for CTTSs and ~ -4.0 for WTTSs. For stars with evolved but accreting disks, including transition disks, the Ca II H & K lines are weaker than expected, which supports the suggestion that refractory elements may be depleted in accretion flows onto these stars. We provide easy-to-use prescriptions to obtain FUV luminosities from either optical line luminosities or from a known accretion rate. We also discuss several individual spectra, including the detection of warm H₂ emission from HD 98800 N, which suggests ongoing accretion for a disk that had been previously classified as a debris disk.

A. Tight Binaries in the UV

A.1. EZ Ori

The STIS acquisition image of EZ Ori reveals two components. The image was obtained with the STIS CCD ($0'0507$ pixels) and the F28x500 [O III] filter, which is centered at 5007 \AA and covers $\sim 12 \text{ \AA}$. The secondary is separated by $\sim 0'18$ from the primary with a $PA \sim 76^\circ$ and a flux in the bandpass equal to $\sim 8\%$ of the primary. The FUV and NUV spectra were obtained with a large slit that includes both stars. The extracted FUV and NUV spectra are consistent with the presence of a binary at that position, with the wavelength solution of the secondary shifted by four pixels because it was not centered in the wide ($2''$) slit. About 20% of the flux in FUV emission lines is from EZ Ori B, although C II emission is relatively weak. Also, 15% of NUV emission and 10% of the Mg II 2800 \AA doublet is from EZ Ori B. Both components are likely accreting based on the strength of these lines and the NUV continuum. For purposes of this paper the two sources are treated as a single star.

A.2. TWA 16

The acquisition image of TWA 16 was obtained with the F150LP long-pass filter. TWA 16 is resolved into two stars separated by $0'56$ at a $PA=316^\circ$ and with a brightness difference of 0.095 mag.

A.3. UZ Tau E

UZ Tau was acquired with the F165LP long-pass filter, which covers spectral regions dominated by the continuum emission. In this image, the northern component is stronger.

The two components of UZ Tau E have a flux ratio of ~ 1.95 and are separated by $0''.32$ mas at a PA=7.9. The two components of UZ Tau E are aligned close to the dispersion direction and are not resolved in the prism spectrum. H α measurements from Hartigan & Kenyon (2003) indicate that both components of UZ Tau E are accreting.

A.4. 2M1614

Metchev & Hillenbrand (2009) found 2MASS J16141107-2305362 (2M1614, or PZ 161411-230536) to be a nearly equal-mass binary separated by $0''.222$ with a PA=304.8°. We confirm the presence of two components, but find a separation of $0''.309$ with a PA=296.7°. The difference could be due to orbital motion. Accretion has been detected in unresolved optical spectra that includes both objects (Pascucci et al. 2007). The presence of strong H $_2$ emission from the N component and the lack of detectable H $_2$ emission from the S component suggests that the system is a CTTS+WTTS binary.

B. Uncertainties In Data From Different Instruments

We have presented PMS star spectra obtained from four instruments on HST with different spectral resolutions, sensitivities, and measurements uncertainties. Figure 17 compares the C IV 1549 Å doublet fluxes and percent errors of PMS stars measured by the four HST instruments and the IUE SWP-LO mode. The errors include both statistical errors in the spectra and flux measurement errors. The faintest PMS stars were observed by the instruments with the lowest spectral resolution (ACS and STIS G140L). For ACS the percent errors increased from typically 10% at high flux levels to $> 20\%$ at its flux limit of 10^{-15} ergs cm $^{-2}$ s $^{-1}$. Note, however, the large scatter in the errors relative to the least squares linear trend line. For STIS G140L observations the errors are roughly 5% at high

flux levels increasing to $> 20\%$ at the lowest flux levels, and the scatter about the linear trend line is relatively small. The moderate-resolution STIS E140M grating has provided fluxes with 5% or smaller errors for high flux level sources increasing to 20% for the lowest flux source at 10^{-14} ergs cm^{-2} s^{-1} . As the curved trend line shows, C IV spectra obtained with the IUE's SWP-LO camera typically show 5% flux errors for sources with high flux levels ($> 10^{-13}$ ergs cm^{-2} s^{-1}) but provide no useful data at flux levels a factor of 3 lower. Table 3 includes a rough estimate of the C IV flux levels for each instrument, below which measurement errors are generally greater than 10%.

REFERENCES

- Aikawa, Y., van Zadelhoff, G. J., van Dishoeck, E. F., & Herbst, E. 2002, *A&A*, 386, 622
- Akeson, R. L., Rice, W. K. M., Boden, A. F., Sargent, A. I., Carpenter, J. M., & Bryden, G. 2007, *ApJ*, 670, 1240
- Alexander, R. D., Clarke, C. J., & Pringle, J. E. 2005, *MNRAS*, 358, 283
- . 2006, *MNRAS*, 369, 216
- Andrews, S. M., & Williams, J. P. 2005, *ApJ*, 631, 1134
- Andrews, S. M., Wilner, D. J., Hughes, A. M., Qi, C., & Dullemond, C. P. 2009, *ApJ*, 700, 1502
- Ardila, D. R., Basri, G., Walter, F. M., Valenti, J. A., & Johns-Krull, C. M. 2002, *ApJ*, 566, 1100
- Ayres, T. R. 2005, in *ESA Special Publication, Vol. 560, 13th Cambridge Workshop on Cool Stars, Stellar Systems and the Sun*, ed. F. Favata, G. A. J. Hussain, & B. Battrick, 419
- Barentsen, G., Vink, J. S., Drew, J. E., Greimel, R., Wright, N. J., Drake, J. J., Martin, E. L., Valdivielso, L., & Corradi, R. L. M. 2011, *MNRAS*, 415, 103
- Barrado Y Navascués, D. 2006, *A&A*, 459, 511
- Basri, G., & Batalha, C. 1990, *ApJ*, 363, 654
- Bergin, E., Calvet, N., D’Alessio, P., & Herczeg, G. J. 2003, *ApJ*, 591, L159
- Bergin, E., Calvet, N., Sitko, M. L., Abgrall, H., D’Alessio, P., Herczeg, G. J., Roueff, E., Qi, C., Lynch, D. K., et al. 2004, *ApJ*, 614, L133

- Bertout, C., Robichon, N., & Arenou, F. 1999, *A&A*, 352, 574
- Bethell, T., & Bergin, E. 2009, *Science*, 326, 1675
- Boden, A. F., Sargent, A. I., Akeson, R. L., Carpenter, J. M., Torres, G., Latham, D. W., Soderblom, D. R., Nelan, E., Franz, O. G., & Wasserman, L. H. 2005, *ApJ*, 635, 442
- Bouvier, J. 1990, *AJ*, 99, 946
- Brown, A., Herczeg, G. J., Brown, J. M., Walter, F. M., Valenti, J., Ardila, D., Hillenbrand, L. A., Edwards, S., Johns-Krull, C. M., Alexander, R., Bergin, E. A., Calvet, N., Bethell, T. J., Ingleby, L., Bary, J. S., Audard, M., Baldwin, C., Roueff, E., Abgrall, H., Gregory, S. G., Ayres, T. R., & Linsky, J. L. 2010, in *Bulletin of the American Astronomical Society*, Vol. 42, AAS/High Energy Astrophysics Division #11, 684–+
- Brown, A., Jordan, C., Millar, T. J., Gondhalekar, P., & Wilson, R. 1981, *Nature*, 290, 34
- Browning, M. K., Basri, G., Marcy, G. W., West, A. A., & Zhang, J. 2010, *AJ*, 139, 504
- Calvet, N., & Gullbring, E. 1998, *ApJ*, 509, 802
- Calvet, N., Muzerolle, J., Briceño, C., Hernández, J., Hartmann, L., Saucedo, J. L., & Gordon, K. D. 2004, *AJ*, 128, 1294
- Cardelli, J. A., Clayton, G. C., & Mathis, J. S. 1989, *ApJ*, 345, 245
- Cohen, M., & Kuhl, L. V. 1979, *ApJS*, 41, 743
- Comerón, F., Spezzi, L., & López Martí, B. 2009, *A&A*, 500, 1045
- de Zeeuw, P. T., Hoogerwerf, R., de Bruijne, J. H. J., Brown, A. G. A., & Blaauw, A. 1999, *AJ*, 117, 354
- Dolan, C. J., & Mathieu, R. D. 2001, *AJ*, 121, 2124

- Donati, J.-F., Jardine, M. M., Gregory, S. G., Petit, P., Bouvier, J., Dougados, C., Ménéard, F., Collier Cameron, A., Harries, T. J., et al. 2007, *MNRAS*, 380, 1297
- Ducourant, C., Teixeira, R., Hambly, N. C., Oppenheimer, B. R., Hawkins, M. R. S., Rapaport, M., Modolo, J., & Lecampion, J. F. 2007, *A&A*, 470, 387
- Dunham, M. M., Evans, N. J., Terebey, S., Dullemond, C. P., & Young, C. H. 2010, *ApJ*, 710, 470
- Enoch, M. L., Young, K. E., Glenn, J., Evans, II, N. J., Golwala, S., Sargent, A. I., Harvey, P., Aguirre, J., Goldin, A., et al. 2006, *ApJ*, 638, 293
- Fedele, D., van den Ancker, M. E., Henning, T., Jayawardhana, R., & Oliveira, J. M. 2010, *A&A*, 510, 72
- Feigelson, E. D., Getman, K., Townsley, L., Garmire, G., Preibisch, T., Grosso, N., Montmerle, T., Muench, A., & McCaughrean, M. 2005, *ApJS*, 160, 379
- France, K., Linsky, J. L., Brown, A., Froning, C. S., & Béland, S. 2010a, *ApJ*, 715, 596
- France, K., Roberge, A., Lupu, R. E., Redfield, S., & Feldman, P. D. 2007, *ApJ*, 668, 1174
- France, K., Stocke, J. T., Yang, H., Linsky, J. L., Wolven, B. C., Froning, C. S., Green, J. C., & Osterman, S. N. 2010b, *ApJ*, 712, 1277
- France, K., Yang, H., & Linsky, J. L. 2011, *ApJ*, 729, 7
- Furlan, E., Sargent, B., Calvet, N., Forrest, W. J., D’Alessio, P., Hartmann, L., Watson, D. M., Green, J. D., Najita, J., & Chen, C. H. 2007, *ApJ*, 664, 1176
- Gammie, C. F. 1996, *ApJ*, 457, 355
- Garcia Lopez, R., Nisini, B., Eisloffel, J., Giannini, T., Bacciotti, F., & Podio, L. 2010, *A&A*, 511, A5+

- García Muñoz, A. 2007, *Planet. Space Sci.*, 55, 1426
- Gehrz, R. D., Smith, N., Low, F. J., Krautter, J., Nollenberg, J. G., & Jones, T. J. 1999, *ApJ*, 512, L55
- Gorti, U., & Hollenbach, D. 2009, *ApJ*, 690, 1539
- Güdel, M., Briggs, K. R., Arzner, K., Audard, M., Bouvier, J., Feigelson, E. D., Franciosini, E., Glauser, A., Grosso, N., et al. 2007, *A&A*, 468, 353
- Gullbring, E., Calvet, N., Muzerolle, J., & Hartmann, L. 2000, *ApJ*, 544, 927
- Gullbring, E., Hartmann, L., Briceno, C., & Calvet, N. 1998, *ApJ*, 492, 323
- Günther, H. M., Schmitt, J. H. M. M., Robrade, J., & Liefke, C. 2007, *A&A*, 466, 1111
- Haisch, Jr., K. E., Lada, E. A., & Lada, C. J. 2001, *ApJ*, 553, L153
- Hartigan, P., & Kenyon, S. J. 2003, *ApJ*, 583, 334
- Herbig, G. H., & Bell, K. R. 1988, *Third Catalog of Emission-Line Stars of the Orion Population : 3 : 1988* (Santa Cruz, CA: Lick Observatory)
- Herczeg, G. J., Cruz, K. L., & Hillenbrand, L. A. 2009, *ApJ*, 696, 1589
- Herczeg, G. J., & Hillenbrand, L. A. 2008, *ApJ*, 681, 594
- Herczeg, G. J., Linsky, J. L., Valenti, J. A., Johns-Krull, C. M., & Wood, B. E. 2002, *ApJ*, 572, 310
- Herczeg, G. J., Linsky, J. L., Walter, F. M., Gahm, G. F., & Johns-Krull, C. M. 2006, *ApJS*, 165, 256
- Herczeg, G. J., Walter, F. M., Linsky, J. L., Gahm, G. F., Ardila, D. R., Brown, A., Johns-Krull, C. M., Simon, M., & Valenti, J. A. 2005, *AJ*, 129, 2777

- Heczeg, G. J., Wood, B. E., Linsky, J. L., Valenti, J. A., & Johns-Krull, C. M. 2004, *ApJ*, 607, 369
- Hernández, J., Hartmann, L., Calvet, N., Jeffries, R. D., Gutermuth, R., Muzerolle, J., & Stauffer, J. 2008, *ApJ*, 686, 1195
- Hughes, J., Hartigan, P., Krautter, J., & Kelemen, J. 1994, *AJ*, 108, 1071
- Indebetouw, R., Mathis, J. S., Babler, B. L., Meade, M. R., Watson, C., Whitney, B. A., Wolff, M. J., Wolfire, M. G., Cohen, M., et al. 2005, *ApJ*, 619, 931
- Ingleby, L., Calvet, N., Bergin, E., Yerasi, A., Espaillat, C., Heczeg, G., Roueff, E., Abgrall, H., Hernández, J., et al. 2009, *ApJ*, 703, L137
- Ingleby, L., Calvet, N., Hernández, J., Briceño, C., Espaillat, C., Miller, J., Bergin, E., & Hartmann, L. 2011, *AJ*, 141, 127
- Johns-Krull, C. M., & Heczeg, G. J. 2007, *ApJ*, 655, 345
- Johns-Krull, C. M., Valenti, J. A., & Linsky, J. L. 2000, *ApJ*, 539, 815
- Kamp, I. 2011, ArXiv e-prints
- Kastner, J. H., Huenemoerder, D. P., Schulz, N. S., Canizares, C. R., & Weintraub, D. A. 2002, *ApJ*, 567, 434
- Kenyon, S. J., & Hartmann, L. 1995, *ApJS*, 101, 117
- Knutson, H. A., Charbonneau, D., Noyes, R. W., Brown, T. M., & Gilliland, R. L. 2007, *ApJ*, 655, 564
- Koerner, D. W., Jensen, E. L. N., Cruz, K. L., Guild, T. B., & Gultekin, K. 2000, *ApJ*, 533, L37

- Lamzin, S. A., Kravtsova, A. S., Romanova, M. M., & Batalha, C. 2004, *Astronomy Letters*, 30, 413
- Larsen, S. S. 2006, Instrument Science Report ACS-2006-02 (Baltimore, MD: Space Telescope Science Institute), 9
- Lecavelier des Etangs, A., Deleuil, M., Vidal-Madjar, A., Roberge, A., Le Petit, F., Hébrard, G., Ferlet, R., Feldman, P. D., Désert, J., & Bouret, J. 2003, *A&A*, 407, 935
- Linsky, J. L., Yang, H., France, K., Froning, C. S., Green, J. C., Stocke, J. T., & Osterman, S. N. 2010, *ApJ*, 717, 1291
- Loinard, L., Torres, R. M., Mioduszewski, A. J., & Rodríguez, L. F. 2008, *ApJ*, 675, L29
- Loinard, L., Torres, R. M., Mioduszewski, A. J., Rodríguez, L. F., González-Lópezlira, R. A., Lachaume, R., Vázquez, V., & González, E. 2007, *ApJ*, 671, 546
- Lombardi, M., Lada, C. J., & Alves, J. 2008, *A&A*, 480, 785
- Luhman, K. L., Allen, L. E., Allen, P. R., Gutermuth, R. A., Hartmann, L., Mamajek, E. E., Megeath, S. T., Myers, P. C., & Fazio, G. G. 2008, *ApJ*, 675, 1375
- Luhman, K. L., Allen, P. R., Espaillat, C., Hartmann, L., & Calvet, N. 2010, *ApJS*, 186, 111
- Luhman, K. L., Stauffer, J. R., Muench, A. A., Rieke, G. H., Lada, E. A., Bouvier, J., & Lada, C. J. 2003, *ApJ*, 593, 1093
- Mamajek, E. E. 2005, *ApJ*, 634, 1385
- Mamajek, E. E., Meyer, M. R., & Liebert, J. 2002, *AJ*, 124, 1670
- Metchev, S. A., & Hillenbrand, L. A. 2009, *ApJS*, 181, 62

- Mohanty, S., Jayawardhana, R., & Basri, G. 2005, *ApJ*, 626, 498
- Moos, H. W., Cash, W. C., Cowie, L. L., Davidsen, A. F., Dupree, A. K., Feldman, P. D.,
Friedman, S. D., Green, J. C., Green, R. F., et al. 2000, *ApJ*, 538, L1
- Mundt, R., & Eislöffel, J. 1998, *AJ*, 116, 860
- Murray-Clay, R. A., Chiang, E. I., & Murray, N. 2009, *ApJ*, 693, 23
- Muzerolle, J., Hillenbrand, L., Calvet, N., Briceño, C., & Hartmann, L. 2003, *ApJ*, 592, 266
- Muzerolle, J., Luhman, K. L., Briceño, C., Hartmann, L., & Calvet, N. 2005, *ApJ*, 625, 906
- Neuhäuser, R., & Forbrich, J. 2008, *The Corona Australis Star Forming Region*, ed.
Reipurth, B., 735–+
- Nguyen, D. C., Jayawardhana, R., van Kerkwijk, M. H., Brandeker, A., Scholz, A., &
Damjanov, I. 2009, *ApJ*, 695, 1648
- Nisini, B., Bacciotti, F., Giannini, T., Massi, F., Eislöffel, J., Podio, L., & Ray, T. P. 2005,
A&A, 441, 159
- Oke, J. B., & Gunn, J. E. 1982, *PASP*, 94, 586
- Pagano, I., Linsky, J. L., Carkner, L., Robinson, R. D., Woodgate, B., & Timothy, G. 2000,
ApJ, 532, 497
- Palla, F., & Stahler, S. W. 2000, *ApJ*, 540, 255
- Pascucci, I., Hollenbach, D., Najita, J., Muzerolle, J., Gorti, U., Herczeg, G. J., Hillenbrand,
L. A., Kim, J. S., Carpenter, J. M., et al. 2007, *ApJ*, 663, 383
- Perez-Becker, D., & Chiang, E. 2011, *ApJ*, 727, 2

- Perryman, M. A. C., Lindegren, L., Kovalevsky, J., Hoeg, E., Bastian, U., Bernacca, P. L., Crézé, M., Donati, F., Grenon, M., et al. 1997, *A&A*, 323, L49
- Prato, L., Ghez, A. M., Piña, R. K., Telesco, C. M., Fisher, R. S., Wizinowich, P., Lai, O., Acton, D. S., & Stomski, P. 2001, *ApJ*, 549, 590
- Preibisch, T., & Zinnecker, H. 1999, *AJ*, 117, 2381
- Redfield, S., Ayres, T. R., Linsky, J. L., Ake, T. B., Dupree, A. K., Robinson, R. D., & Young, P. R. 2003, *ApJ*, 585, 993
- Ribas, I., Guinan, E. F., Güdel, M., & Audard, M. 2005, *ApJ*, 622, 680
- Salyk, C., Blake, G. A., Boogert, A. C. A., & Brown, J. M. 2009, *ApJ*, 699, 330
- Santos, N. C., Israelian, G., Mayor, M., Bento, J. P., Almeida, P. C., Sousa, S. G., & Ecuivillon, A. 2005, *A&A*, 437, 1127
- Saucedo, J., Calvet, N., Hartmann, L., & Raymond, J. 2003, *ApJ*, 591, 275
- Stelzer, B., & Schmitt, J. H. M. M. 2004, *A&A*, 418, 687
- Sterzik, M. F., Alcalá, J. M., Covino, E., & Petr, M. G. 1999, *A&A*, 346, L41
- Swade, D. A., Hopkins, E., & Swam, M. S. 2001, in *Astronomical Society of the Pacific Conference Series*, Vol. 238, *Astronomical Data Analysis Software and Systems X*, ed. F. R. Harnden, Jr., F. A. Primini, & H. E. Payne, 295
- Tian, F., Toon, O. B., Pavlov, A. A., & De Sterck, H. 2005, *ApJ*, 621, 1049
- Valenti, J. A., Basri, G., & Johns, C. M. 1993, *AJ*, 106, 2024
- Valenti, J. A., Fallon, A. A., & Johns-Krull, C. M. 2003, *ApJS*, 147, 305
- Valenti, J. A., & Fischer, D. A. 2005, *ApJS*, 159, 141

- Valenti, J. A., Johns-Krull, C. M., & Linsky, J. L. 2000, *ApJS*, 129, 399
- Walter, F. M., Herczeg, G., Brown, A., Ardila, D. R., Gahm, G. F., Johns-Krull, C. M.,
Lissauer, J. J., Simon, M., & Valenti, J. A. 2003, *AJ*, 126, 3076
- Walter, F. M., Vrba, F. J., Mathieu, R. D., Brown, A., & Myers, P. C. 1994, *AJ*, 107, 692
- Webb, R. A., Zuckerman, B., Platais, I., Patience, J., White, R. J., Schwartz, M. J., &
McCarthy, C. 1999, *ApJ*, 512, L63
- Weingartner, J. C., & Draine, B. T. 2001, *ApJ*, 548, 296
- White, R. J., Gabor, J. M., & Hillenbrand, L. A. 2007, *AJ*, 133, 2524
- White, R. J., & Ghez, A. M. 2001, *ApJ*, 556, 265
- Woitke, P., Kamp, I., & Thi, W. 2009, *A&A*, 501, 383
- Wood, B. E., & Karovska, M. 2004, *ApJ*, 601, 502
- Wood, B. E., Redfield, S., Linsky, J. L., Müller, H., & Zank, G. P. 2005, *ApJS*, 159, 118
- Yang, H., Linsky, J. L., & France, K. 2011, *ApJ*, 730, L10+
- Yelle, R. V. 2004, *Icarus*, 170, 167
- Zuckerman, B., Song, I., Bessell, M. S., & Webb, R. A. 2001, *ApJ*, 562, L87

Table 1. Summary of Observations.

ID ^a	HBC ^b	Name	Alternate Name	$\alpha(2000)$	$\delta(2000)$	Instrument	UT Date	N ^c	t_{exp} (s) ^d	Program ID ^e
1	...	DK Cet	HD 12039	01 57 48.98	-21 54 05.3	ACS PR130L	2007 JUL 13	1	2440.0	10810
2	20	LkH α 330	...	03 45 48.28	+32 24 11.9	ACS PR130L	2007 SEP 25	1	1786.0	11151
3	...	2M0414 ^f	XEST 20-OM-002	04 14 11.98	+28 12 00.2	ACS PR130L	2008 NOV 08	1	1769.0	11151
4	23	FM Tau	Haro 6-1	04 14 13.44	+28 12 51.1	ACS PR130L	2007 OCT 31	1	2482.0	10840
5	26	FP Tau	MH α 259-23	04 14 47.00	+26 46 26.5	ACS PR130L	2007 AUG 15	1	2482.0	10840
6	27	CX Tau	MH α 259-22	04 14 47.86	+26 48 11.0	ACS PR130L	2007 AUG 08	1	2482.0	10840
7	368	LkCa 3	V1098 Tau	04 14 47.94	+27 52 35.8	STIS G140L	2003 SEP 20	1	1859.2	9790
8	370	LkCa 4	V1068 Tau	04 16 28.04	+28 07 35.9	STIS G140L	2004 MAR 01	1	1859.2	9790
9	28	CY Tau	MH α 259-5	04 17 33.72	+28 20 46.8	STIS E140M	2000 DEC 06	1	5178.0	8206
						ACS PR130L	2007 NOV 04	1	890.0	10864
10	32	BP Tau	HD 281934	04 19 15.86	+29 06 27.2	STIS G140L	2002 JAN 12	1	1841.0	9081
11	379	LkCa 7	V1070 Tau	04 19 41.35	+27 49 49.0	STIS G140L	2004 FEB 04	1	1859.2	9790
12	33	DE Tau	MH α 259-8	04 21 55.57	+27 55 07.0	ACS PR130L	2007 AUG 14	1	2482.0	10840
13	34	RY Tau	HD 283571	04 21 57.44	+28 26 36.0	STIS G140L	2000 SEP 20	1	1440.0	8317
14	35	T Tau	HD 284419	04 21 59.42	+19 32 06.4	STIS G140L	2000 FEB 07	1	1622.0	8317
						STIS E140M	2000 SEP 08	1	12080.8	8157
15	385	IP Tau	LkCa 8	04 24 57.08	+27 11 56.6	ACS PR130L	2007 AUG 14	1	2482.0	10840
16	36	DF Tau	HD 283654	04 27 02.79	+25 42 22.6	STIS E140M	1999 SEP 18	2	9390.1	8157
17	388	V1072 Tau	Tap 35	04 27 10.57	+17 50 42.6	GHRIS G160M	1995 SEP 09	1	5984.0	5875
18	399	V827 Tau	Tap 42	04 32 14.55	+18 20 15.0	STIS G140L	2004 JAN 26	1	1859.2	9790
19	400	V826 Tau	Tap 43	04 32 15.82	+18 01 39.1	STIS G140L	2003 SEP 08	1	1859.2	9790
20	...	MHO 6	...	04 32 22.10	+18 27 42.6	ACS PR130L	2007 OCT 01	1	1773.0	11151
21	53	UZ Tau W	Elia 3-11	04 32 42.83	+25 52 31.4	ACS PR130L	2007 AUG 15	1	2182.0	10840
22	52	UZ Tau E	Elia 3-11	04 32 43.04	+25 52 31.1	ACS PR130L	2007 AUG 15	1	2182.0	10840

Table 1—Continued

ID ^a	HBC ^b	Name	Alternate Name	$\alpha(2000)$	$\delta(2000)$	Instrument	UT Date	N ^c	t_{exp} (s) ^d	Program ID ^e
23	405	V830 Tau	Tap 46	04 33 10.02	+24 33 43.3	STIS G140L	2003 OCT 26	1	1859.2	9790
24	56	GI Tau	Haro 6-21	04 33 34.06	+24 21 17.0	ACS PR130L	2007 SEP 10	1	2300.0	10840
25	57	GK Tau	Haro 6-22	04 33 34.56	+24 21 05.9	ACS PR130L	2007 SEP 10	1	2300.0	10840
26	58	DL Tau	MH α 259-13	04 33 39.02	+25 20 38.9	ACS PR130L	2007 AUG 15	1	2480.0	10840
27	60	HN Tau A	Haro 6-24	04 33 39.36	+17 51 52.3	ACS PR130L	2007 AUG 31	1	2476.0	10840
28	406	HN Tau B	Haro 6-24	04 33 39.36	+17 51 52.3	ACS PR130L	2007 AUG 31	1	2476.0	10840
29	62	DM Tau	MH α 257-6	04 33 48.72	+18 10 10.1	STIS G140L	2003 FEB 05	2	3882.0	9374
30	61	CI Tau	Haro 6-25	04 33 52.00	+22 50 30.2	ACS PR130L	2007 AUG 15	1	2300.0	10840
31	63	AA Tau	MH α 259-17	04 34 55.42	+24 28 53.2	ACS PR130L	2007 AUG 15	1	2480.0	10840
32	65	DN Tau	MH α 259-18	04 35 27.37	+24 14 59.5	ACS PR130L	2007 AUG 15	1	2300.0	10840
33	67	DO Tau	MH α 259-15	04 38 28.58	+26 10 49.4	ACS PR130L	2007 SEP 20	1	2568.0	10840
34	...	2M0439 ^f	...	04 39 01.63	+23 36 03.0	ACS PR130L	2008 SEP 11	1	1767.0	11151
35	419	LkCa 15	V1079 Tau	04 39 17.73	+22 21 03.8	STIS G140L	2003 FEB 13	4	11357.0	9374
36	70	DP Tau	MH α 259-19	04 42 37.70	+25 15 37.5	ACS PR130L	2006 DEC 06	1	2400.0	10840
37	...	2M0444 ^f	...	04 44 27.13	+25 12 16.4	ACS PR130L	2008 SEP 11	1	1418.0	11151
38	74	DR Tau	MH α 257-8	04 47 06.22	+16 58 42.1	STIS E140M	2000 AUG 29	1	5794.0	8206
						ACS PR130L	2007 NOV 26	1	2298.0	10840
39	75	DS Tau	MH α 259-2	04 47 48.59	+29 25 11.5	STIS E140M	2000 AUG 24	1	5846.0	8206
40	77	GM Aur	MH α 259-1	04 55 10.97	+30 21 59.7	STIS G140L	2003 APR 01	2	4173.0	9374
						ACS PR130L	2007 SEP 15	1	1036.0	10864
41	79	SU Aur	HD 282624	04 55 59.38	+30 34 01.7	STIS G140L	2000 FEB 13	2	4400.0	8317
42	427	V397 Aur	Tap 57	04 56 02.03	+30 21 04.1	STIS G140L	2004 JAN 20	1	1859.0	9790
43	429	V836 Tau	Tap 59	05 03 06.59	+25 23 20.0	STIS E140M	2001 FEB 14	1	9390.3	8157
44	80	RW Aur AB	HD 240764	05 07 49.56	+30 24 05.2	GHRS G160M	1993 AUG 10	1	897.6	3845

Table 1—Continued

ID ^a	HBC ^b	Name	Alternate Name	$\alpha(2000)$	$\delta(2000)$	Instrument	UT Date	N ^c	t_{exp} (s) ^d	Program ID ^e
45	...	2M0518 ^f	...	05 18 02.85	+23 27 12.7	ACS PR130L	2007 OCT 06	1	1767.0	11151
46	84	CO Ori	Haro 6-44	05 27 38.20	+11 25 39.1	STIS G140L	2000 FEB 25	2	4212.0	8317
47	85	GW Ori	HD 244138	05 29 08.38	+11 52 12.7	STIS G140L	2000 FEB 22	1	4308.0	8317
48	113	V1044 Ori	Parenago 1404	05 34 16.38	-05 36 45.3	STIS G140L	2000 FEB 15	1	1555.0	8317
49	114	EZ Ori	Parenago 1409	05 34 18.48	-05 04 47.6	STIS G140L	2000 FEB 25	1	1515.0	8317
50	464	CQ Tau	HD 36910	05 35 58.47	+24 44 54.1	ACS PR130L	2007 OCT 06	1	890.0	10846
51	167	Parenago 2441	BD -04 1191	05 36 51.27	-04 25 40.0	STIS G140L	2000 SEP 20	1	1608.0	8317
52	...	HD 53143	SAO 249700	06 59 59.65	-61 20 10.3	ACS PR130L	2007 MAR 20	1	2480.0	10810
53	...	HD 61005	SAO 198166	07 35 47.46	-32 12 14.0	ACS PR130L	2007 SEP 11	1	2460.0	10810
54	...	TWA 6	TYC 7183-1477-1	10 18 28.70	-31 50 02.9	ACS PR130L	2008 NOV 03	1	1936.0	11151
55	...	TWA 7	TYC 7190-2111-1	10 42 30.11	-33 40 16.2	ACS PR130L	2007 MAR 31	1	2456.0	10810
56	...	V419 Hya	HD 92945	10 43 28.27	-29 03 51.4	ACS PR130L	2007 MAR 29	1	2454.0	10810
57	568	TW Hya	CD -34°7151	11 01 51.86	-34 42 17.1	STIS E140M	2000 MAY 07	1	2300.2	8041
						IUE SWP-LO	1984 JUL 16	1	6000.0	TTGJL
						IUE LWR-LO	1979 OCT 29	1	3600.0	TTGBH
58	...	TWA 3 S	HEN 3-600	11 10 27.81	-37 31 53.2	ACS PR130L	2008 JUL 17	1	2012.0	11151
59	...	TWA 3 N	HEN 3-600	11 10 27.88	-37 31 52.0	ACS PR130L	2008 JUL 17	1	2012.0	11151
60	...	2M1111 ^f	CHXX 37	11 11 44.00	-76 20 10.0	ACS PR130L	2008 NOV 19	1	2148.0	11151
61	...	TWA 13 N	...	11 21 17.24	-34 46 45.5	ACS PR130L	2007 JUN 23	1	2456.0	10810
62	...	TWA 13 S	...	11 21 17.45	-34 46 49.8	ACS PR130L	2007 JUN 23	1	2456.0	10810
63	...	HD 98800 N	...	11 22 05.29	-24 46 39.8	ACS PR130L	2007 JUN 21	1	2420.0	10810
64	...	HD 98800 S	...	11 22 05.29	-24 46 39.8	ACS PR130L	2007 JUN 21	1	2420.0	10810
65	...	TWA 8 S	...	11 32 41.16	-26 52 09.0	ACS PR130L	2007 JUL 13	1	1934.0	11151
66	...	TWA 8 N	...	11 32 41.25	-26 51 55.9	ACS PR130L	2007 JUL 13	1	1934.0	11151

Table 1—Continued

ID ^a	HBC ^b	Name	Alternate Name	$\alpha(2000)$	$\delta(2000)$	Instrument	UT Date	N ^c	t_{exp} (s) ^d	Program ID ^e
67	...	TWA 9 N	...	11 48 23.73	-37 28 48.5	ACS PR130L	2008 NOV 29	1	1944.0	11151
68	...	TWA 9 S	...	11 48 24.23	-37 28 49.2	ACS PR130L	2008 NOV 29	1	1944.0	11151
69	...	TWA 27	2M1207A ^f	12 07 33.46	-39 32 54.0	STIS G140L	2004 JUL 25	1	5050.0	9841
70	...	TWA 16 N	...	12 34 56.29	-45 38 07.5	ACS PR130L	2008 JUL 10	1	2008.0	11151
71	...	TWA 16 S	...	12 34 56.29	-45 38 07.5	ACS PR130L	2008 JUL 10	1	2008.0	11151
72	...	MML 28	...	13 01 50.69	-53 04 58.2	ACS PR130L	2007 JAN 24	1	2466.0	10810
73	...	MML 34	MP Mus	13 22 07.55	-69 38 12.2	IUE SWP-LO	1995 JUL 06	1	1260.0	USSBS
74	...	MML 36	...	13 37 57.30	-41 34 41.8	ACS PR130L	2007 FEB 23	1	2418.0	10810
75	251	RU Lup	HD 142560	15 56 42.26	-37 49 15.7	STIS E140M	2000 JUL 12	1	2970.1	8157
76	...	V1146 Sco	SCO PMS 15	15 57 20.18	-23 38 48.5	STIS G140L	2004 APR 15	1	1859.0	9790
77	608	V1149 Sco	HD 143006	15 58 36.93	-22 57 14.9	IUE SWP-LO	1993 JUL 19	1	6000.0	QC071
78	252	RY Lup	...	15 59 28.39	-40 21 51.3	STIS G140L	2000 AUG 25	1	4724.0	8205
79	...	V1154 Sco	SCO PMS 23	16 02 10.44	-22 41 28.3	STIS G140L	2003 SEP 17	1	1859.2	9790
80	612	HO Lup	Hen 3-1140	16 07 00.61	-39 02 19.4	IUE SWP-LO	1986 APR 24	1	12600.0	PMHTS
81	...	V1157 Sco	SCO PMS 45	16 11 20.55	-18 20 54.1	STIS G140L	2003 SEP 15	1	1859.2	9790
82	254	V866 Sco	MH α 365-14	16 11 31.40	-18 38 24.5	IUE SWP-LO	1979 JUN 06	1	15060.0	CC110
83	...	2M1614N ^f	...	16 14 11.07	-23 05 36.2	ACS PR130L	2008 MAR 13	1	1861.0	11151
84	...	2M1614S ^f	...	16 14 11.07	-23 05 36.2	ACS PR130L	2008 MAR 13	1	1861.0	11151
85	264	V2129 Oph	SR 9	16 27 40.32	-24 22 02.7	IUE SWP-LO	1987 APR 13	1	18900.0	IC129
86	270	V1121 Oph	MH α 362-3	16 49 15.31	-14 22 08.6	IUE SWP-LO	1981 SEP 11	1	5100.0	UK417
87	...	V4046 Sgr	HD 319139	18 14 10.47	-32 47 34.5	ACS PR130L	2005 AUG 03	1	630.0	10348
88	...	2M1842 ^f	Hen 3-1722	18 42 57.97	-35 32 42.7	ACS PR130L	2008 APR 21	1	2012.0	11151
89	...	2M1852 ^f	...	18 52 17.30	-37 00 11.9	ACS PR130L	2008 APR 22	1	2032.0	11151
90	...	AU Mic	HD 197481	20 45 09.53	-31 20 27.3	IUE LWR-LO	1980 AUG 05	18	32400.0	multiple ^g

Table 1—Continued

ID ^a	HBC ^b	Name	Alternate Name	$\alpha(2000)$	$\delta(2000)$	Instrument	UT Date	N ^c	t_{exp} (s) ^d	Program ID ^e
						IUE SWP-LO	1980 AUG 04	14	151200.0	multiple ^g
91	...	HD 202917	SAO 246975	21 20 49.96	−53 02 03.1	ACS PR130L	2007 MAR 24	1	2504.0	10810

^aInternal identification number for cross-referencing.

^bCatalog number from Herbig & Bell (1988).

^cNumber of exposures.

^dExposure time.

^eHST and IUE program ID's.

^fName Abbreviations: 2M0414 for 2MASS J04141188+2811535; 2MJ0439 for 2MASS J04390163+2336029; 2MASS J04442713+2512164; 2M0518 for 2MASS J05180285+2327127; 2M1111 for 2MASS J11114632-7620092; 2M1207A for 2MASS J12073347-3932540; 2M1614N for 2MASS J16141107-2305362 N; 2M1614S for 2MASS J16141107-2305362 S; 2M1842 for 2MASS J18425797-3532427; 2M1852 for 2MASS J18521730-3700119.

^gMultiple program IDs: MR381, FSCJL and UK353.

Table 2. Pre-Main Sequence Stars.

ID	Name	Region	Distance (pc)	Type ^a	Category	A_V	$\log L_{phot}$ ^b	$\log L_{acc}$ ^c	$\log L_X$ ^d	H β ^e	Ca II K ^e	Reference ^f
1	DK Cet	field	42	G4	WTTS	0.0	-0.05	1,2
2	LkH α 330	Per	250	G3	CTTS	1.8	1.2	3
3	2M0414	Taurus	140	M6.25	CTTS	0.7	-1.90	-2.50	...	2.50	1.90	4
4	FM Tau	Taurus	140	M1	CTTS	0.3	-0.77	-1.7	29.69	17.8	3.32	5,33
5	FP Tau	Taurus	140	M4	CTTS	0.0	-0.57	-2.8	...	10.7	1.54	5
6	CX Tau	Taurus	140	M2.5	CTTS	0.2	-0.48	-2.6	...	14.9	2.12	5
7	LkCa 3	Taurus	140	M1	WTTS	0.4	0.04	2.42	4.35	6
8	LkCa 4	Taurus	140	K7	WTTS	1.2	-0.02	...	30.30	5.86	4.30	5,34
9	CY Tau	Taurus	140	M2	CTTS	0.3	-0.34	-1.39	29.18	54.8	8.89	7,33
10	BP Tau	Taurus	140	K7	CTTS	0.5	-0.03	-0.75	30.17	85.5	20.5	7,33
11	LkCa 7	Taurus	140	M0+M3.5	WTTS	0.6	-0.14	5.40	3.65	6
12	DE Tau	Taurus	140	M2	CTTS	0.6	-0.06	-1.15	28.4	6.58	5.68	7,36
13	RY Tau	Taurus	140	F8	CTTS	1.8	0.89	...	30.72	8,33
14	T Tau	Taurus	140	K0	CTTS	1.5	0.86	-0.29	30.97	517	261	5,33
15	IP Tau	Taurus	140	M0	CTTS	0.3	-0.39	-2.15	...	14.7	4.26	7
16	DF Tau	Taurus	140	M2	CTTS	0.6	0.16	-0.75	...	1567	31.7	4
17	HBC 388	Taurus	140	K1	WTTS?	0.0	0.13	5
18	V827 Tau	Taurus	140	K7	WTTS	1.1	0.04	...	30.57	6.22	5.02	5,33
19	V826 Tau	Taurus	140	K7	WTTS	0.3	-0.10	...	30.62	6.09	4.31	6,33
20	MHO 6	Taurus	140	M5	CTTS	1.0	-0.85	-2.80	...	1.60	0.45	4
21	UZ Tau W	Taurus	140	M1+M4	CTTS	1.0	-0.20	-1.5	29.87	16.5	2.86	5,33
22	UZ Tau E	Taurus	140	M2+M3	CTTS	0.3	-0.51	-1.6	[W+E]	34.8	33.6	5,33
23	V830 Tau	Taurus	140	K7	WTTS	0.7	-1.01	...	30.68	4.08	4.63	5,33
24	GI Tau	Taurus	140	K7	CTTS	1.3	-0.07	-1.03	29.94	3.11	0.74	7,33

Table 2—Continued

ID	Name	Region	Distance (pc)	Type ^a	Category	A_V	$\log L_{phot}$ ^b	$\log L_{acc}$ ^c	$\log L_X$ ^d	$H\beta$ ^e	Ca II K ^e	Reference ^f
25	GK Tau AB	Taurus	140	K7	CTTS	0.9	0.03	-1.46	30.09	11.1	4.14	7,33
26	DL Tau	Taurus	140	K7	CTTS	1.3	...	-0.65	...	60.9	38.1	9
27	HN Tau A	Taurus	140	K5	CTTS	0.6	-0.72	-1.45	29.26	28.8	38.9	7,33
28	HN Tau B	Taurus	140	M4.5	CTTS	0.9	-1.60	...	[A+B]	2.47	1.84	5,33
29	DM Tau	Taurus	140	M1	CTTS	0.6	-0.61	-1.5	29.26	24.1	2.98	5,33
30	CI Tau	Taurus	140	K7	CTTS	1.8	-0.08	-0.57	...	44.4	29.4	5
31	AA Tau	Taurus	140	K7	CTTS	0.74	-0.13	-1.60	30.02	10.4	3.67	7,33
32	DN Tau	Taurus	140	M0	CTTS	1.9	-0.06	-1.79	30.03	10.5	5.01	7,33
33	DO Tau	Taurus	140	M0	CTTS	2.3	0.00	-0.20	...	48.2	42.1	7
34	2M0439	Taurus	140	M5	CTTS	0.0	-1.05	-3.20	...	1.54	0.59	4
35	LkCa 15	Taurus	140	K5	CTTS	1.0	-0.13	-1.6	6.64	5
36	DP Tau	Taurus	140	M0.5	CTTS	1.2	...	-1.4	9
37	2M0444	Taurus	140	M7.25	CTTS	0.0	-1.92	-4.60	...	0.34	0.053	7
38	DR Tau	Taurus	140	K7	CTTS	1.2	...	-0.13	...	71.4	119	10
39	DS Tau	Taurus	140	K5	CTTS	0.3	-0.24	-0.70	...	47.1	13.7	7
40	GM Aur	Taurus	140	K5	CTTS	0.3	-0.13	-1.15	29.84	66.4	10.2	7,34
41	SU Aur	Taurus	140	G2	CTTS	0.9	0.89	-1.00	31.07	11,33
42	V397 Aur	Taurus	140	K5	WTTS	0.0	-0.10	...	30.51	...	3.89	6,33
43	V836 Tau	Taurus	140	K7	CTTS	1.1	-0.49	-2.50	...	9.44	1.46	4
44	RW Aur AB	Taurus	140	K4	CTTS	1.2	...	0.64	...	126	521	9
45	2M0518	Taurus	140	M5	CTTS	1.0	0.016	-2.55	...	1.51	0.43	4
46	CO Ori	λ Ori	450	G0	CTTS	2.0	1.35	0.22	11
47	GW Ori	λ Ori	450	G0	CTTS	1.3	1.79	0.67	11
48	V1044 Ori	Ori OB 1c	440	G2	CTTS	2.0	0.83	-0.22	11

Table 2—Continued

ID	Name	Region	Distance (pc)	Type ^a	Category	A_V	$\log L_{phot}^b$	$\log L_{acc}^c$	$\log L_X^d$	$H\beta^e$	Ca II K ^e	Reference ^f
49	EZ Ori	Ori OB 1c	440	G3	CTTS	0.6	0.77	-1.00	11
50	CQ Tau		130	F2	CTTS	1.9	0.82	12
51	Parenago 2441	Ori OB 1c	440	F9	CTTS	0.4	1.06	-0.40	11
52	HD 53143	field	18.4	G8	WTTS	0.0	-0.30	2,13
53	HD 61005	field	35	G4	WTTS	0.0	-0.25	2,1
54	TWA 6	TWA	51	K7	WTTS	0.0	-0.93	19.9	9.71	14,15
55	TWA 7	TWA	27	M1	WTTS	0.0	-1.09	...	29.46	29.8	22.9	14,15,35
56	V419 Hya	field	22	K0	WTTS	0.0	-0.43	2,16
57	TW Hya	TWA	56	K7	CTTS	0.0	-0.77	-1.50	...	462	65.0	2,4
58	TWA 3 S	TWA	34	M3.5	WTTS	0.0	-1.27	...	29.17	6.92	6.46	14,17,35
59	TWA 3 N	TWA	34	M3	CTTS	0.0	-1.10	-2.50	[S+N]	47.9	12.3	14,17,35
60	2M1111	Cha I	175	K1	CTTS	1.3	0.33	...	30.6	p07
61	TWA 13 N	TWA	53	M1	WTTS	0.0	-0.77	...	29.87	20.2	14.7	14,18,36
62	TWA 13 S	TWA	53	M2	WTTS	0.0	-0.79	...	29.97	39.2	2.54	14,18,36
63	HD 98800 N	TWA	40	K5(SB)	WTTS	0.0	-0.38	14,15
64	HD 98800 S	TWA	40	K5(SB)	WTTS	0.0	-0.35	14,15
65	TWA 8 S	TWA	39	M5	WTTS	0.0	-1.66	...	28.56	2.65	1.47	14,15,36
66	TWA 8 N	TWA	38	M2	WTTS	0.0	-1.04	...	29.76	22.5	14.8	14,15,36
67	TWA 9 N	TWA	56	M1	WTTS	0.0	-0.82	...	28.85	3.09	2.10	14,15,36
68	TWA 9 S	TWA	69	K5	WTTS	0.0	-0.52	...	30.08	18.8	8.74	14,15,36
69	TWA 27	TWA	52.4	M8.25	BD	0.0	-2.72	-5.30	...	0.341	0.0128	19,17
70	TWA 16 N	TWA	72	M1.5	WTTS	0.0	-0.74	14,20
71	TWA 16 S	TWA		Included in primary component								
72	MML 28	field	108	K2	WTTS	0.6	-0.37	...	30.0	21

Table 2—Continued

ID	Name	Region	Distance (pc)	Type ^a	Category	A_V	$\log L_{phot}$ ^b	$\log L_{acc}$ ^c	$\log L_X$ ^d	H β ^e	Ca II K ^e	Reference ^f
73	MML 34	isolated?	86	K1	CTTS	1.2	0.10	...	30.2	2
74	MML 36	field	81	K0	WTTS	0.0	0.0	...	30.4	21
75	RU Lup	Lup	140	K7	CTTS	0.1	-0.22	-0.50	...	361	492	22
76	V1146 Sco	USco	145	M0(B)	WTTS	0.0	-0.41	1.27	23,24,25
77	HD 143006	USco	145	G6	CTTS	1.6	0.39	...	30.1	23,26
78	RY Lup	Lup	140	K4	CTTS	0.65	0.42	27
79	V1154 Sco	USco	145	K5(B)	WTTS	0.4	0.08	23,24,25
80	HO Lup	Lup	140	M1	CTTS	1.3	0.30	28
81	V1157 Sco	USco	145	K5	WTTS	1.0	-0.14	0.756	23,24,25
82	V866 Sco	Oph	125	K0	CTTS	2.2	...	0.16	...	171	132	29,9
83	2M1614N	USco	145	K0	CTTS	1.5	0.50	...	30.5	23,26
84	2M1614S	USco		Included in primary component								
85	V2129 Oph	Oph	125	K6	CTTS	0.6	0.23	56.0	22.3	29,30,
86	V1121 Oph	Oph	125	K5	CTTS	1.2	redo	-0.6	29,31,9
87	V4046 Sgr	isolated	83	K5(SB)	CTTS	0.0	-0.09	
88	2M1842	CrA	130	K2	CTTS	1.0	0.12	...	30.3	33.0	17.0	1,26,32
89	2M1852	CrA	130	K3	CTTS	0.9	-0.24	...	30.5	22.9	9.49	1,26,32
90	AU Mic	β Pic	9.9	M1	WTTS	-0.9	29.5			20
91	HD 202917	TucHor	46	G7	WTTS	0.0	-0.18	16

^a“SB” stands for spectroscopic binary and “B” stands for binary.

^bPhotospheric luminosity in units of solar luminosity.

^cAccretion luminosity in units of solar luminosity.

^dX-ray (0.3 - 10.0 keV) luminosity in units of erg s^{-1} .

^eFluxes of the $\text{H}\beta$ and Ca II K lines in units of $10^{-14} \text{ erg s}^{-1} \text{ cm}^{-2}$.

^fReferences: 1: White et al. (2007); 2: Perryman et al. (1997); 3: Cohen & Kuhi (1979);
4: Herczeg & Hillenbrand (2008); 5: White & Ghez (2001); 6: Kenyon & Hartmann (1995);
7: Gullbring et al. (1998); 8: Nguyen et al. (2009); 9: Valenti et al. (1993);
10: Gullbring et al. (2000); 11: Calvet et al. (2004); 12: Garcia Lopez et al. (2010);
13: Santos et al. (2005); 14: Mamajek (2005); 15: Webb et al. (1999);
16: Valenti & Fischer (2005); 17: Herczeg et al. (2009); 18: Sterzik et al. (1999);
19: Ducourant et al. (2007); 20: Zuckerman et al. (2001); 21: Mamajek et al. (2002);
22: Herczeg et al. (2005); 23: de Zeeuw et al. (1999); 24: Walter et al. (1994);
25: Preibisch & Zinnecker (1999); 26: Pascucci et al. (2007); 27: Bouvier (1990);
28: Hughes et al. (1994); 29: Loinard et al. (2008); 30: Donati et al. (2007);
31: Basri & Batalha (1990); 32: Neuhäuser & Forbrich (2008); 33: Güdel et al. (2007);
34: Brown et al. (2010); 35: this paper from Swift data; 36: this paper from Chandra data.

Table 3. Summary of FUV Instruments.

Observatory	Instrument	Setting	Wavelength Range	Aperture	Resolution	$\log F_{\text{C IV}}^{\text{a}}$
HST	STIS	E140M	1150–1700	$0.2'' \times 0.06''$	45,800	-13.2
HST	STIS	G140L	1150–1700	$52'' \times 2''$	935–1440	-14.0
HST	ACS/SBC	PR130L	1250–2000	$28'' \times 31''$	60–150	-12.7
HST	GHR	G160M	1382–1420	$2'' \times 2''$	18,000	N/A
			1532–1568	$2'' \times 2''$	19,000	N/A
IUE		SWP-LO	1150–1975	$10'' \times 20''$	~ 300	-13.0

^aC IV flux levels below which the measurement errors are typically $\geq 10\%$.

Table 4. Line Flux Measurements.

ID	Name	Instrument	O I 1304	C II 1335	O I 1355	Si IV 1394	Si IV 1403	C IV 1549	He II 1640	H ₂ emission	L_{FUV}
1	DK Cet	ACS	10.3(1.5)	13.4(1.7)	...	16.9(2.9)	—	40.7(8.1)	28.0(8.5)	No	2.21×10^{-5}
2	LkH α 330	ACS	0.83(0.11)	...	No	3.61×10^{-4}
3	2M0414	ACS	0.94(0.20)	2.50(0.38)	...	4.16(0.76)	—	17.8(3.9)	4.16(0.76)	No	3.46×10^{-4}
4	FM Tau	ACS	16.2(3.8)	21.4(7.0)	No	3.37×10^{-4}
5	FP Tau	ACS	0.48(0.08)	1.22(0.13)	...	1.91(0.20)	—	1.72(0.35)	...	Yes	5.76×10^{-5}
6	CX Tau	ACS	0.41(0.08)	0.83(0.13)	1.71(0.23)	...	Yes	4.67×10^{-5}
7	LkCa 3	STIS G140L	3.85(0.42)	3.41(0.32)	0.46(0.16)	1.03(0.19)	0.63(0.17)	5.95(0.67)	3.89(0.75)	No	5.89×10^{-5}
8	LkCa 4	STIS G140L	7.31(0.54)	10.3(0.6)	1.10(0.26)	4.39(0.41)	2.79(0.36)	28.8(1.5)	12.6(1.4)	No	1.40×10^{-3}
9	CY Tau	STIS E140M	40.0(1.7)	14.3(0.7)	...	9.0(0.5)	6.7(0.6)	79.1(4.5)	33.6(2.2)	Yes	9.20×10^{-4}
	CY Tau	ACS	9.35(0.89)	7.02(0.71)	...	12.4(1.9)	—	19.5(2.2)	22.7(2.2)	Yes	5.05×10^{-4}
10	BP Tau	STIS G140L	104(07)	35.6(3.6)	...	31.6(2.9)	27.5(4.3)	246(08)	135(08)	Yes	4.05×10^{-3}
11	LkCa 7	STIS G140L	4.40(0.39)	5.55(0.42)	0.84(0.21)	1.24(0.23)	0.96(0.23)	12.0(1.0)	10.0(1.3)	No	1.83×10^{-4}
12	DE Tau	ACS	55.3(3.6)	13.5(1.3)	...	18.2(1.8)	—	70.8(9.9)	25.0(4.5)	Yes	2.10×10^{-3}
13	RY Tau	STIS G140L	79(3)	49.7(5.0)	11.8(5.0)	38.6(3.0)	50.5(2.0)	59.3(3.0)	28.6(3.0)	Yes	7.20×10^{-2}
14	T Tau	STIS G140L	176(2)	33.7(6.0)	15.0(2.0)	51.9(3.0)	60.7(6.0)	215(10)	56.4(2.0)	Yes	6.01×10^{-2}
	T Tau	STIS E140M	170(2)	19.3(0.8)	12.9(0.4)	31.0(1.0)	16.2(1.4)	165(3)	48.1(2.3)	Yes	3.75×10^{-2}
15	IP Tau	ACS	2.36(0.41)	2.24(0.31)	...	4.97(0.64)	—	27.8(2.2)	16.6(3.2)	No	2.80×10^{-4}
16	DF Tau	STIS E140M	15.0(0.7)	9.0(0.9)	...	9.0(1.2)	7.6(0.4)	28.9(3.0)	4.5(0.9)	Yes	6.88×10^{-4}
17	V1072 Tau	GHRS G160M	7(1)	4(1)	14(2)
18	V827 Tau	STIS G140L	4.25(0.38)	4.37(0.36)	1.06(0.21)	1.51(0.24)	1.22(0.24)	10.8(0.9)	8.8(1.1)	No	5.32×10^{-4}
19	V826 Tau	STIS G140L	2.63(0.33)	4.21(0.35)	0.86(0.18)	1.42(0.23)	0.94(0.21)	10.9(0.9)	7.6(1.0)	No	6.65×10^{-5}
20	MHO 6	ACS	Yes	2.19×10^{-4}
21	UZ Tau W	ACS	4.04(0.56)	1.38(0.28)	...	1.12(0.27)	—	8.0(1.1)	6.4(1.2)	Yes	7.59×10^{-4}
22	UZ Tau E	ACS	5.1(1.3)	6.5(1.4)	...	12.7(2.3)	—	13.7(2.7)	...	Yes	5.56×10^{-4}

Table 4—Continued

ID	Name	Instrument	O I 1304	C II 1335	O I 1355	Si IV 1394	Si IV 1403	C IV 1549	He II 1640	H ₂ emission	L_{FUV}
23	V830 Tau	STIS G140L	3.56(0.35)	4.13(0.35)	0.67(0.17)	1.10(0.20)	0.91(0.20)	8.76(0.81)	7.1(1.0)	No	1.67×10^{-4}
24	GI Tau	ACS	0.91(0.19)	—	2.97(0.66)	1.77(0.54)	Yes	6.09×10^{-4}
25	GK Tau	ACS	2.42(0.33)	2.31(0.33)	...	3.00(0.61)	—	14.3(2.1)	12.1(2.8)	No	8.68×10^{-4}
26	DL Tau	ACS	0.76(0.08)	0.34(0.07)	...	3.35(0.30)	—	6.12(0.91)	...	No	9.64×10^{-4}
27	HN Tau A	ACS	2.66(0.35)	7.1(1.2)	...	16.7(3.7)	—	6.9(1.7)	...	Yes	1.47×10^{-3}
28	HN Tau B	ACS	0.69(0.15)	0.39(0.09)	2.79(0.66)	1.10(0.27)	No	1.51×10^{-4}
29	DM Tau	STIS G140L	25.0(4.6)	24.3(5.3)	10.7(5.0)	25.5(6.9)	—	62.2(7.1)	64.9(8.4)	Yes	4.02×10^{-3}
30	CI Tau	ACS	0.40(0.06)	0.13(0.05)	...	0.36(0.10)	—	0.62(0.24)	...	Yes	9.21×10^{-4}
31	AA Tau	ACS	...	5.4(1.4)	...	6.7(1.3)	—	Yes	1.99×10^{-3}
32	DN Tau	ACS	27.5(1.6)	7.7(1.2)	...	7.6(1.3)	—	41.9(4.7)	37.6(6.4)	No	4.49×10^{-4}
33	DO Tau	ACS	...	1.56(0.59)	...	3.66(0.77)	—	Yes	3.25×10^{-2}
34	2M0439	ACS	1.15(0.24)	0.91(0.26)	Yes	5.59×10^{-6}
35	V1079 Tau	STIS G140L	8.7(1.1)	8.3(1.2)	...	24.1(2.2)	—	80.3(4.7)	15.5(1.9)	Yes	3.67×10^{-3}
36	DP Tau	ACS	5.16(0.87)	15.5(1.5)	...	8.7(1.4)	—	Yes	6.66×10^{-3}
37	2M0444	ACS	Yes	1.18×10^{-5}
38	DR Tau	STIS E140M	29.0(1.5)	...	4.70(0.60)	4.19(0.45)	4.34(0.44)	11.3(2.3)	7.5(1.5)	Yes	1.15×10^{-3}
	DR Tau	ACS	27.8(2.9)	18.5(2.7)	—	28.7(6.0)	...	Yes	1.25×10^{-2}
39	DS Tau	STIS E140M	32.5(2.1)	23.5(2.6)	...	23.5(1.5)	18.2(1.0)	287(10)	85.7(5.6)	Yes	3.44×10^{-3}
40	GM Aur	STIS G140L	91.9(7.6)	35.9(5.8)	...	53.8(8.6)	—	168(12)	50.8(6.7)	Yes	1.95×10^{-3}
	GM Aur	ACS	56.8(6.0)	21.8(2.6)	...	28.9(3.6)	—	118(13)	48.0(5.7)	Yes	1.75×10^{-3}
41	SU Aur	STIS G140L	137(5)	74.7(3.0)	36.8(3.0)	41.1(3.0)	53(5)	242(10)	55.9(6.0)	Yes	8.83×10^{-3}
42	V397 Aur	STIS G140L	3.95(0.35)	4.84(0.38)	0.85(0.20)	1.94(0.27)	1.53(0.28)	10.9(0.9)	8.3(1.1)	No	3.75×10^{-5}
43	V836 Tau	STIS E140M	2.0(0.8)	1.0(1.0)	16.4(1.3)	4.0(1.5)	Yes	...
44	RW Aur AB	GHRS G160M	190(20)	250(20)	230(64)	...	N/A	...

Table 4—Continued

ID	Name	Instrument	O I 1304	C II 1335	O I 1355	Si IV 1394	Si IV 1403	C IV 1549	He II 1640	H ₂ emission	L_{FUV}
45	2M0518	ACS	1.19(0.08)	1.28(0.10)	...	0.72(0.10)	—	7.10(0.67)	...	No	2.14×10^{-4}
46	CO Ori	STIS G140L	8.6(0.5)	7.8(0.8)	1.8(0.5)	3.1(0.5)	2.8(2.0)	7.1(0.8)	2.3(0.8)	Yes	1.83×10^{-1}
47	GW Ori	STIS G140L	175(10)	43.7(3.0)	15.2(7.0)	50.1(10.0)	49.1(3.0)	166(5)	45.7(5.0)	Yes	3.32×10^{-1}
48	V1044 Ori	STIS G140L	66(20)	20.1(0.2)	9.3(2.0)	44.4(1.0)	44.6(1.0)	113(10)	22.0(3.0)	No	9.58×10^{-1}
49	EZ Ori	STIS G140L	56.0(7.0)	14.3(1.9)	11.7(1.7)	14.9(1.0)	17.0(0.5)	47.7(3.0)	11.4(1.0)	No	1.39×10^{-2}
50	CQ Tau	ACS	107(12)	82(11)	...	27.4(2.5)	—	153(13)	...	No	9.38×10^{-2}
51	Parenago 2441	STIS G140L	17.5(2.0)	10.8(2.0)	5.6(0.1)	11.5(0.1)	10.3(1.0)	26.2(2.0)	10.9(2.0)	No	7.40×10^{-3}
52	HD 53143	ACS	13.0(0.9)	18.6(1.1)	...	14.2(1.5)	—	38.8(4.4)	26.5(3.5)	Yes	3.92×10^{-6}
53	HD 61005	ACS	5.71(0.49)	10.3(0.7)	...	9.55(0.78)	—	25.5(3.2)	18.7(2.2)	No	8.41×10^{-6}
54	TWA 6	ACS	7.84(0.71)	15.5(0.9)	...	12.0(0.9)	—	59.8(4.0)	30.5(3.2)	No	2.18×10^{-5}
55	TWA 7	ACS	10.7(0.8)	13.2(1.0)	...	8.42(0.86)	—	42.2(3.6)	47.4(3.6)	No	5.98×10^{-6}
56	V419 Hya	ACS	11.6(0.8)	19.1(1.2)	...	10.0(1.0)	—	37.0(4.7)	36.2(4.5)	No	4.24×10^{-6}
57	TW Hya	STIS E140M	706(15)	469(5)	23.3(4.5)	164(9)	86.5(5.9)	4472(166)	1195(41)	Yes	1.86×10^{-3}
58	TWA 3S	ACS	5.7(1.0)	10.5(0.9)	...	7.92(0.75)	—	36.6(3.8)	22.4(2.2)	No	7.23×10^{-6}
59	TWA 3N	ACS	9.8(1.3)	14.6(1.9)	...	9.14(1.4)	—	55.8(10.5)	...	Yes	2.78×10^{-5}
60	2M1111	ACS	0.64(0.17)	1.61(0.27)	...	2.11(0.46)	—	9.4(1.3)	7.8(1.7)	Yes	2.65×10^{-3}
61	TWA 13 N	ACS	5.62(0.40)	7.83(0.62)	...	3.24(0.39)	—	18.1(1.6)	21.2(2.3)	No	1.07×10^{-5}
62	TWA 13 S	ACS	5.52(0.57)	6.61(0.57)	...	4.11(0.42)	—	21.5(1.8)	22.4(2.4)	No	1.14×10^{-5}
63	HD 98800 N	ACS	4.15(0.73)	5.17(0.71)	...	2.97(0.64)	—	24.2(2.6)	12.8(2.3)	Yes	1.07×10^{-5}
64	HD 98800 S	ACS	10.6(0.9)	13.5(0.8)	...	6.79(0.76)	—	34.5(2.9)	40.5(2.7)	No	1.18×10^{-5}
65	TWA 8 S	ACS	1.67(0.13)	1.80(0.21)	...	1.27(0.17)	—	4.49(0.48)	4.92(0.59)	No	1.25×10^{-6}
66	TWA 8 N	ACS	7.73(0.66)	9.97(0.93)	...	4.11(0.50)	—	23.6(1.8)	25.5(1.7)	No	6.22×10^{-6}
67	TWA 9 N	ACS	0.99(0.08)	0.86(0.11)	...	0.64(0.10)	—	2.68(0.29)	3.53(0.35)	Yes	1.41×10^{-6}
68	TWA 9 S	ACS	5.81(0.49)	7.06(0.72)	...	4.97(0.46)	—	25.3(2.0)	28.0(2.6)	No	2.10×10^{-5}

Table 4—Continued

ID	Name	Instrument	O I 1304	C II 1335	O I 1355	Si IV 1394	Si IV 1403	C IV 1549	He II 1640	H ₂ emission	L_{FUV}
69	TWA 27	STIS G140L	0.47(0.20)	0.62(0.12)	3.12(0.39)	0.67(0.25)	Yes	1.28×10^{-6}
70	TWA 16 N	ACS	1.47(0.12)	1.47(0.13)	...	0.89(0.10)	—	3.55(0.37)	5.52(0.51)	No	4.26×10^{-6}
71	TWA 16 S	ACS	1.42(0.12)	2.03(0.19)	...	1.29(0.15)	—	4.79(0.54)	5.19(0.73)	No	4.51×10^{-6}
72	MML 28	ACS	1.66(0.13)	1.41(0.13)	...	1.41(0.14)	—	6.24(0.84)	7.5(1.3)	Yes	6.08×10^{-5}
73	MML 34	IUE	365(39)	256(31)	1172(67)	...	Yes	2.46×10^{-2}
74	MML 36	ACS	1.07(0.22)	...	No	1.02×10^{-6}
75	RU Lup	STIS E140M	261(2)	118(2)	35.5(1.2)	390(4)	303(4)	705(7)	75.7(2.1)	Yes	5.27×10^{-3}
76	V1146 Sco	STIS G140L	0.87(0.18)	1.16(0.18)	...	0.44(0.12)	—	2.46(0.44)	1.99(0.54)	No	8.15×10^{-6}
77	V1149 Sco	IUE	130(10)	...	No	8.17×10^{-2}
78	RY Lup	STIS G140L	50.6(2.4)	50.0(2.3)	11.0(1.7)	20.3(2.8)	—	82.8(3.7)	11.0(2.5)	266	2.19×10^{-3}
79	V1154 Sco	STIS G140L	3.20(0.35)	5.42(0.41)	0.74(0.18)	2.64(0.37)	—	7.25(0.79)	8.46(1.1)	No	8.72×10^{-5}
80	HO Lup	IUE	75(10)	26(8)	121(15)	38(12)	Yes	2.87×10^{-2}
81	V1157 Sco	STIS G140L	0.17(0.09)	0.17(0.07)	...	0.14(0.06)	0.07(0.06)	1.09(0.28)	0.83(0.37)	No	3.61×10^{-5}
82	V866 Sco	IUE	34.0(6.3)	30.9(4.5)	21.4(4.5)	50(13)	...	No	1.13×10^{-1}
83	2M1614N	ACS	...	1.13(0.19)	...	1.33(0.26)	—	6.37(0.90)	3.39(0.54)	Yes	2.15×10^{-3}
84	2M1614S	ACS	1.46(0.27)	2.16(0.27)	...	2.95(0.40)	—	12.6(1.4)	6.4(1.5)	No	2.29×10^{-3}
85	V2129 Oph	IUE	18.1(4.0)	19.4(4.0)	195(17)	89(17)	No	2.14×10^{-3}
86	V1121 Oph	IUE	18.1(4.0)	19.6(4.0)	77(13)	...	No	8.76×10^{-3}
87	V4046 Sgr	ACS	56.7(7.0)	84.7(9.1)	...	49.0(7.7)	—	227(19)	130(11)	Yes	7.23×10^{-4}
88	2M1842	ACS	77.9(0.72)	54.9(6.8)	...	84.3(9.3)	—	221(23)	55.7(9.6)	Yes	1.25×10^{-2}
89	2M1852	ACS	4.54(0.53)	6.68(0.96)	...	5.96(0.80)	—	16.0(2.3)	...	Yes	1.64×10^{-3}
90	AU Mic	STIS E140M	98.8	21.28	5.2	49.3	29.2	327.0	263.5	No	4.07×10^{-6}
91	HD 202917	ACS	11.0(1.2)	23.9(2.3)	...	19.8(2.4)	—	68.6(8.2)	51(13)	No	3.04×10^{-5}

Note. — The flux values are in units of 10^{-15} erg s⁻¹cm⁻². “...” indicates that the line is not apparent in the spectrum. “—” indicates that the Si IV 1403 line is not resolved and the flux in the Si IV 1394 column represents the total flux of the doublet. The total FUV luminosity between 1250 and 1700Å, L_{FUV} , are in solar units.

Table 5. FUV line fluxes extracted from synthetic ACS PR130L spectra and their corresponding percent differences to the line fluxes in the actual STIS G140L Data.

ID	Object	O I 1304	%	C II 1335	%	Si IV 1394 + Si IV 1403	%	C IV 1549	%
7	LkCa 3	3.91	1.6	3.56	4.3	1.69	1.8	6.90	16.0
8	LkCa 4	7.21	-1.4	10.0	-2.9	7.46	3.9	32.1	11.5
10	BP Tau	109	5.3	45.0	26.7	64.7	9.6	247	0.5
11	LkCa 7	4.51	2.5	5.21	-6.1	2.28	3.6	12.5	4.2
13	RY Tau	71.7	-5.0	45.4	-0.8	76.8	-10.3	698	3.9
14	T Tau	253	-1.6	31.2	-17.7	108	0.0	225	4.7
18	V827 Tau	4.43	4.2	4.55	4.1	2.25	-17.6	12.7	17.2
19	V826 Tau	2.62	-0.4	4.24	0.7	2.16	-8.5	11.3	3.7
23	V830 Tau	3.88	9.0	4.10	-0.7	1.97	-2.0	9.25	5.6
29	DM Tau	20.3	-15.4	20.9	-16.7	28.3	28.6	61.6	-1.0
35	LkCa 15	11.9	36.2	11.6	39.3	23.0	-4.5	75.1	-6.5
40	GM Aur	88.9	-3.3	35.5	-1.2	46.6	-14.2	145	-13.7
41	SU Aur	166	-2.9	66.5	-10.4	89.4	-1.4	267	3.7
42	V397 Aur	4.06	2.8	4.75	-1.9	3.59	3.4	12.4	13.6
46	CO Ori	8.23	-5.3	6.85	-4.2	9.23	9.2	9.55	8.9
47	GW Ori	206	4.4	40.5	-3.7	94.7	-1.6	188	-9.4
48	V1044 Ori	97.1	-2.9	19.6	-3.1	97.2	0.4	128	7.2
40	EZ Ori	63.4	-3.5	12.2	-14.9	29.6	-1.8	50.9	10.5
51	Paranago 2441	65.8	-3.2	8.81	-16.9	22.9	14.5	3.10	6.5

Table 5—Continued

ID	Object	O I 1304	%	C II 1335	%	Si IV 1394 + Si IV 1403	%	C IV 1549	%
69	TWA 27	0.62	9.0	0.67	9.1	2.79	-10.6
76	V1146 Sco	0.84	-4.1	1.09	-5.6	0.52	20.5	2.93	18.9
78	RY Lup	61.8	22.1	47.9	-4.1	21.5	5.9	86.2	4.1
79	V1154 Sco	2.76	-13.9	5.42	0.0	2.28	-13.8	10.4	43.2
81	V1157 Sco	0.15	-13.0	0.19	12.8	0.27	28.5	0.96	-11.8

Note. — The flux values are in units of 10^{-15} erg s $^{-1}$ cm $^{-2}$.

Table 6: Best Linear Fits of Line Luminosities and Stellar Properties.

Equation	Best Fit			1:1 Fit ^w		r^x
	a	b	σ^y	a	σ	
$\log(L_{C\ IV}) = a + b \log(L_{acc})^z$	-2.766	0.877	0.60	-2.609	0.56	0.84
$\log(L_{FUV}) = a + b \log(L_{C\ IV})$	1.059	1.023	0.19	0.960	0.20	0.97
$\log(L_{FUV}) = a + b \log(L_{acc})$	-1.670	0.836	0.38	-1.433	0.47	0.85
CTTS: $\log(L_{C\ IV}) = a + b \log(L_{Ca\ K})$	-1.508	0.673	0.22	-0.223	0.57	0.78
WTTS: $\log(L_{C\ IV}) = a + b \log(L_{Ca\ K})$	0.609	1.232	0.19	-0.509	0.26	0.93
CTTS: $\log(L_{C\ IV}) = a + b \log(L_{H\alpha})$	-0.677	0.877	0.45	-0.197	0.41	0.77
$\log(L_{FUV}) = a + b \log(L_{H\alpha})$	-1.632	0.760	0.46	-0.888	0.46	0.80
WTTS: $\log(L_{C\ IV}) = a + b \log(L_{H\alpha})$	-0.308	0.968	0.39	-0.141	0.37	0.76
$\log(L_{FUV}) = a + b \log(L_{H\alpha})$	-2.312	0.623	0.25	-0.608	0.28	0.78
CTTS: $\log(L_{C\ IV}) = a + b \log(L_{H\beta})$	-0.406	0.826	0.50	0.389	0.49	0.77
$\log(L_{FUV}) = a + b \log(L_{H\beta})$	-2.323	0.766	0.48	-1.678	0.49	0.80
WTTS: $\log(L_{C\ IV}) = a + b \log(L_{H\beta})$	2.436	1.354	0.19	0.407	0.32	0.91
$\log(L_{FUV}) = a + b \log(L_{H\beta})$	-3.190	0.564	0.13	-1.197	0.35	0.89
$\log(L_{O\ I}) = a + b \log(L_{C\ IV})$	0.349	1.161	0.15	-0.363	0.23	0.98
$\log(L_{C\ II}) = a + b \log(L_{C\ IV})$	-0.409	1.010	0.14	-0.450	0.14	0.98
$\log(L_{Si\ IV}) = a + b \log(L_{C\ IV})$	-0.321	1.051	0.17	-0.542	0.18	0.98
$\log(L_{He\ II}) = a + b \log(L_{C\ IV})$	-0.932	0.853	0.14	-0.278	0.22	0.97
$\log(L_X) = a + b \log(L_{C\ IV})$	0.21

^wThe 1:1 fits have the slope of the lines, b , fixed at 1.

^x r is the Pearson linear correlation coefficient. The associated false-alarm probability is zero, except that it

Table 7: Luminosity in FUV Bandpasses^a

Bandpass	TW Hya	AU Mic
$\log L_{phot}$	-0.77	-0.89
L_{FUV}^b (912–2000)	-2.52	-4.77
L_{FUV} (1250–1700)	-2.73	-5.18
$L_{Ca\ K}$	-4.18	-5.39 ^x
$L_{H\beta}$	-3.33	–
$L_{H\alpha}$	-2.34	-4.56 ^x
912–1000	-4.08	-5.91
C III $\lambda 977$	-4.61	-6.39
1000–1100	-3.95	-5.68
O VI $\lambda 1032$	-4.62	-6.15
1100–1200	-3.89	-5.89
C III $\lambda 1177$	-4.49	-6.23
1200–1300 ^b	-3.47	-5.80
Ly α $\lambda 1216$	-1.95 ^z	-4.49 ^y
1300–1400	-3.43	-5.75
C II $\lambda 1335$	-4.45	-6.15
1400–1500	-3.57	-6.19
1500–1600	-3.21	-5.71
C IV $\lambda 1549$	-3.54	-5.92
1600–1700	-3.31	-5.72
He II $\lambda 1640$	-3.85	-6.04
1700–1800	-3.31	-5.86
1800–1900	-3.29	-5.67
1900–2000	-3.37	-5.89
2000–3000	-2.23	-4.22
Mg II	-3.41	-4.98

^aLuminosities in $\log L_{\lambda}/L_{bol}$; ^bExcluding Ly α ;

^xPrunings et al. (2010); ^yWood et al. (2005);

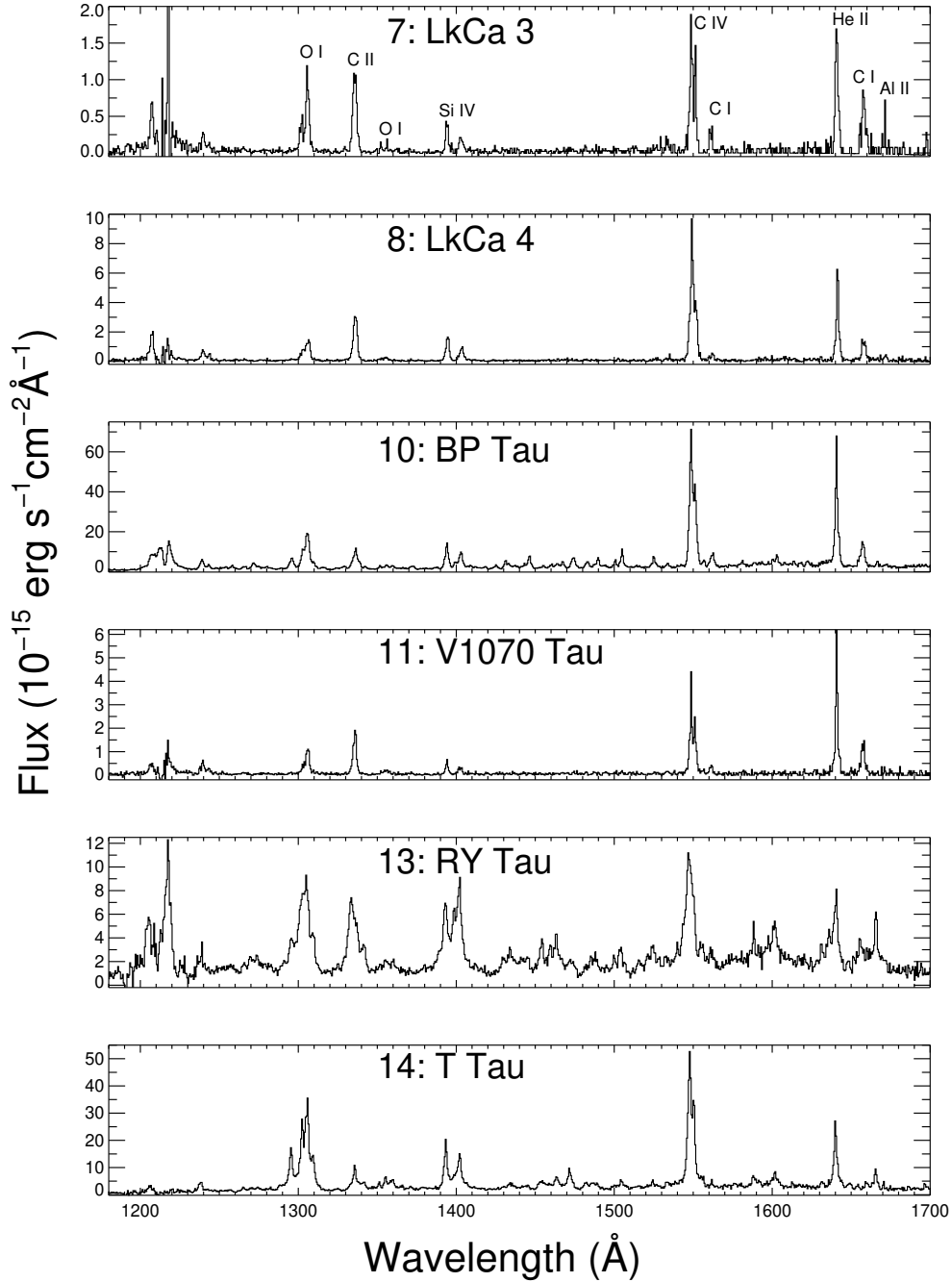


Fig. 1.— The STIS G140L spectra for a few stars in our sample are shown. Plots of the full sample are available in the online version of this paper.

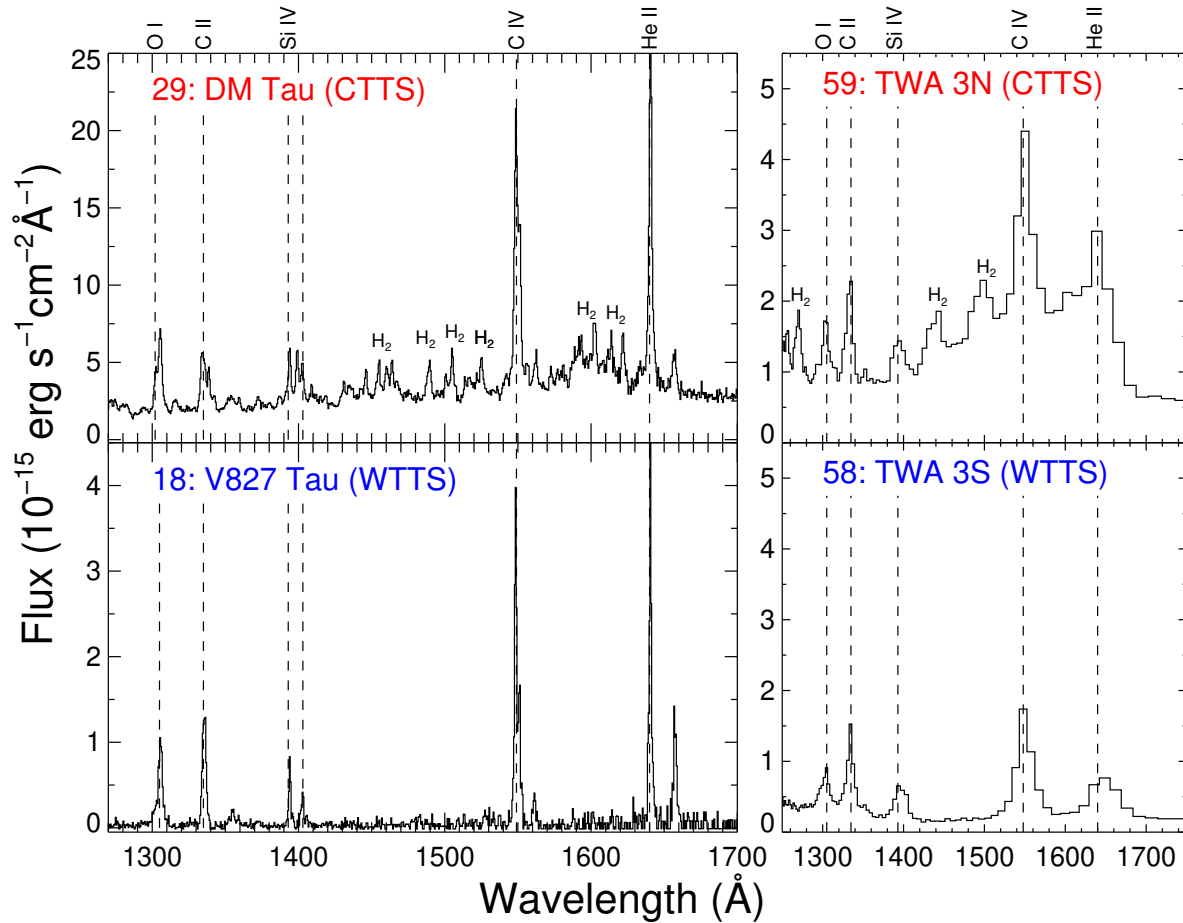


Fig. 2.— STIS G140L spectra of DM Tau and V827 Tau are shown in the left panels, and ACS PR130L spectra of TWA 3N and TWA 3S are shown in the right panels. Prominent atomic and molecular emission features are marked. Plots of the full sample are available in the online version of this paper.

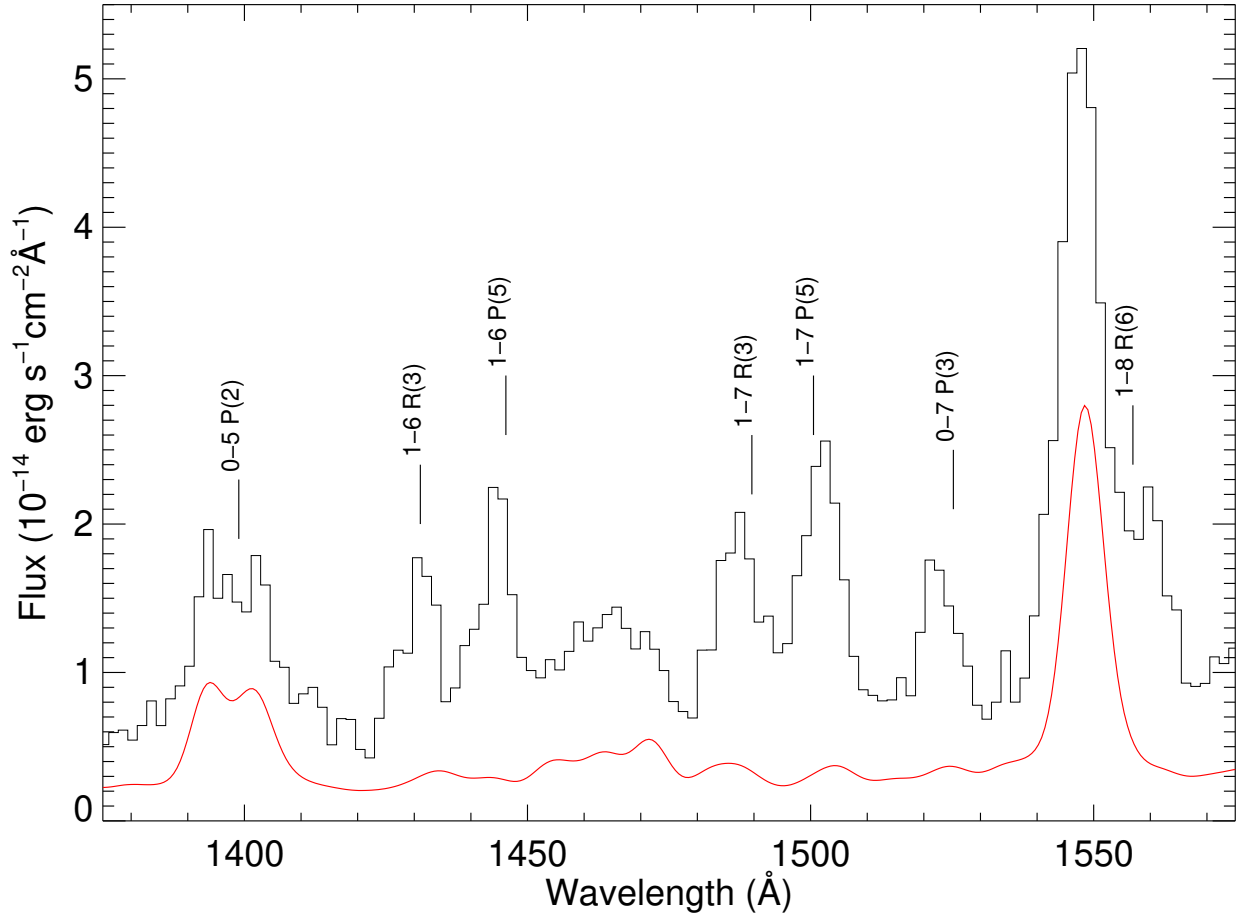


Fig. 3.— FUV spectra of T Tau observed with two different instruments and aperture sizes. The histogram is the observation with the *IUE* SWP-LO grating using the large ($10'' \times 20''$) aperture, and the solid red curve is a STIS G140L spectrum observed with a $52'' \times 0.2''$ slit and degraded to the *IUE* spectral resolution. Several notable H_2 features in the *IUE* spectrum are identified with solid vertical lines, and the transitions are also noted.

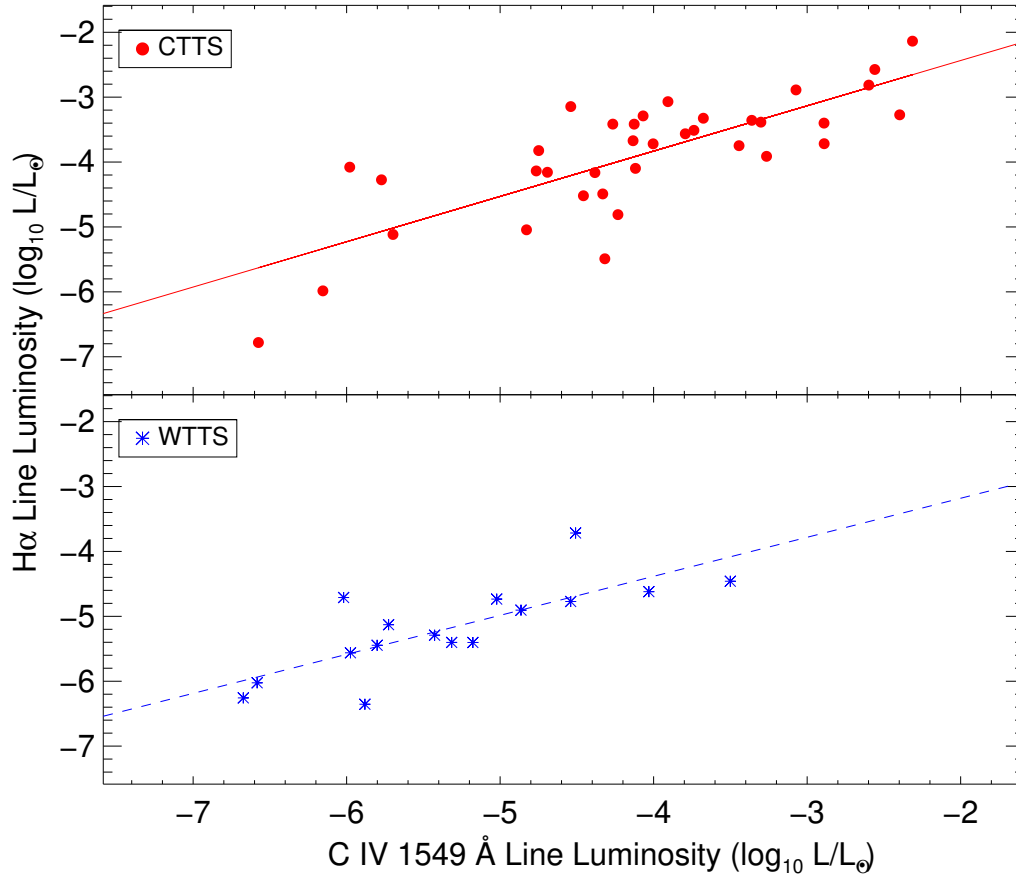


Fig. 4.— $H\alpha$ line luminosity is plotted against the C IV $\lambda 1549$ doublet luminosity for CTTSs (*top panel*) and WTTSs (*bottom panel*). The red solid and blue dashed lines are the best fits in logarithmic space for CTTSs and WTTSs, respectively.

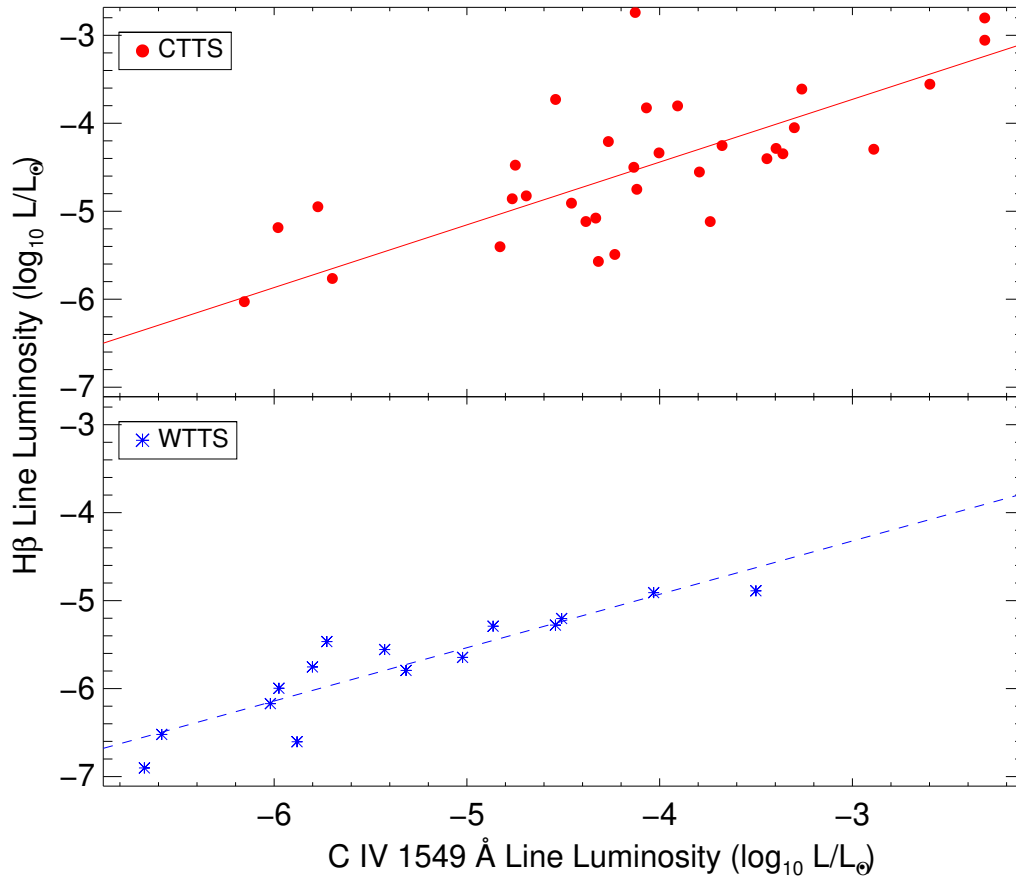


Fig. 5.— $H\beta$ line luminosity is plotted against the C IV $\lambda 1549$ doublet luminosity for CTTSs (*top panel*) and WTTSs (*bottom panel*). The red solid and blue dashed lines are the best fits in logarithmic space for CTTSs and WTTSs, respectively.

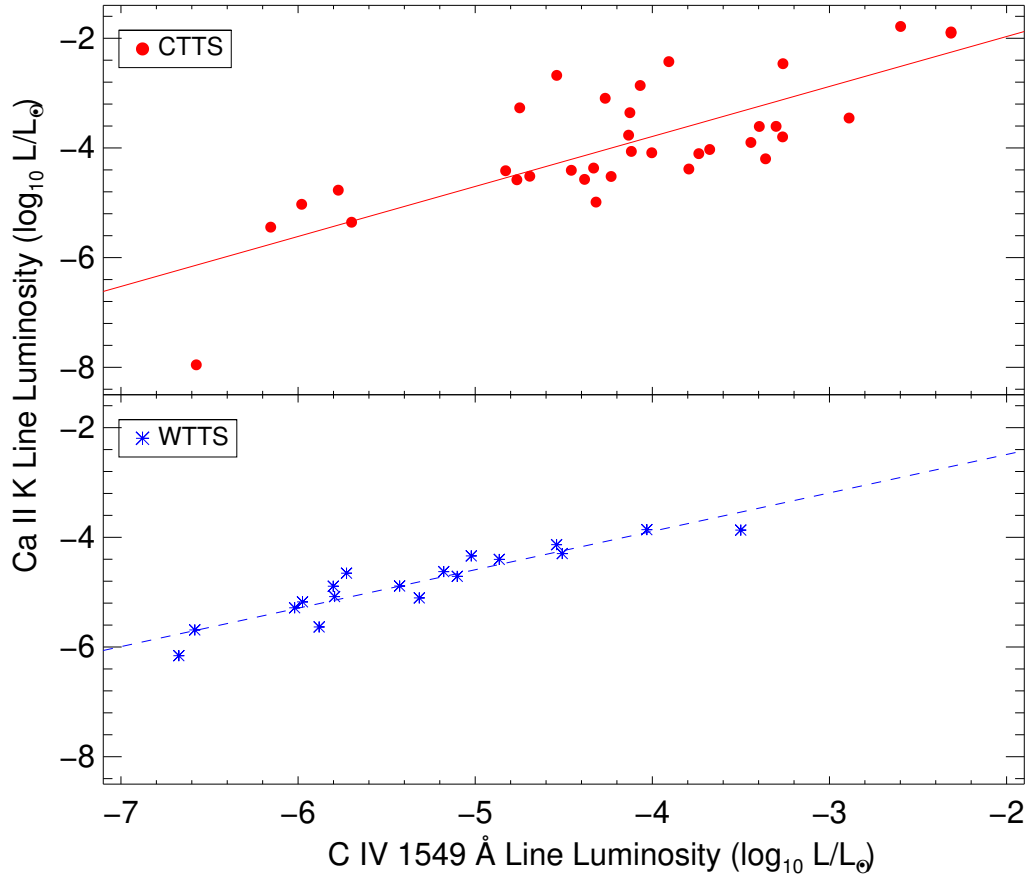


Fig. 6.— The Ca II K line luminosity is plotted against the C IV $\lambda 1549$ doublet luminosity for CTTSs (*top panel*) and WTTSs (*bottom panel*). The red solid and blue dashed lines are the best fit in logarithmic space for CTTSs and WTTSs, respectively.

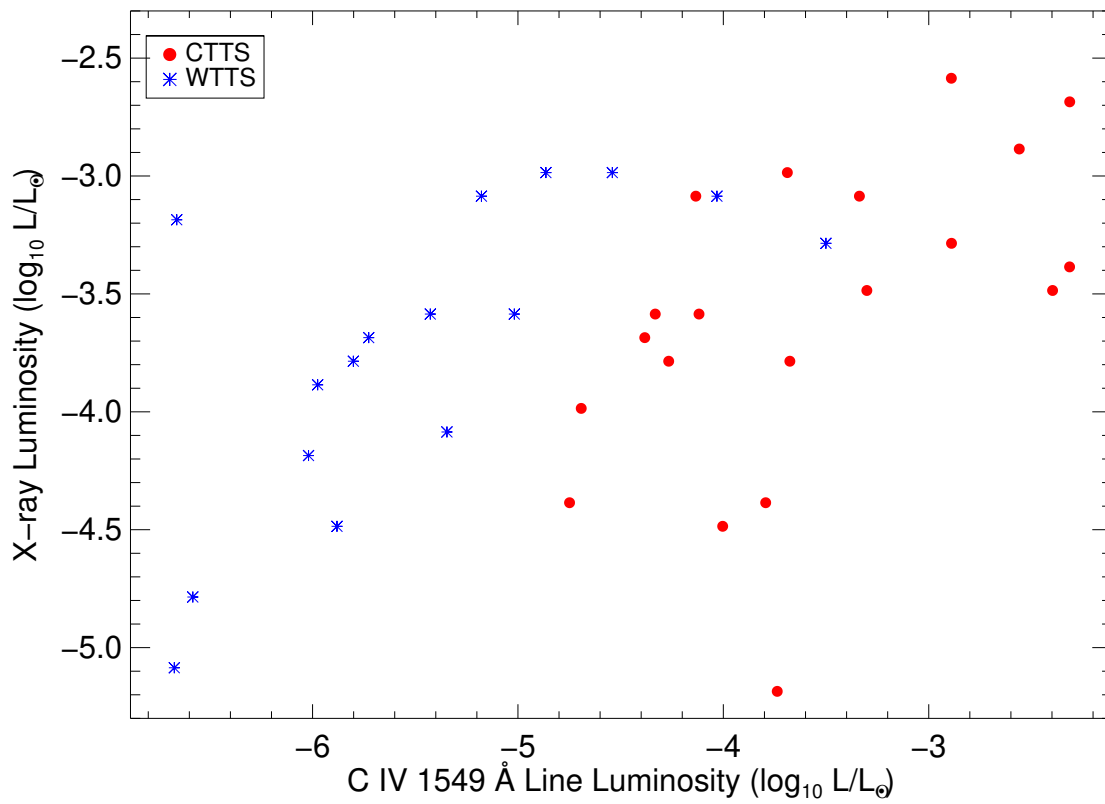


Fig. 7.— The X-ray luminosity is plotted against the C IV $\lambda 1549$ doublet luminosity. CTTSs are plotted as red filled circles and WTTSs are plotted as blue asterisks.

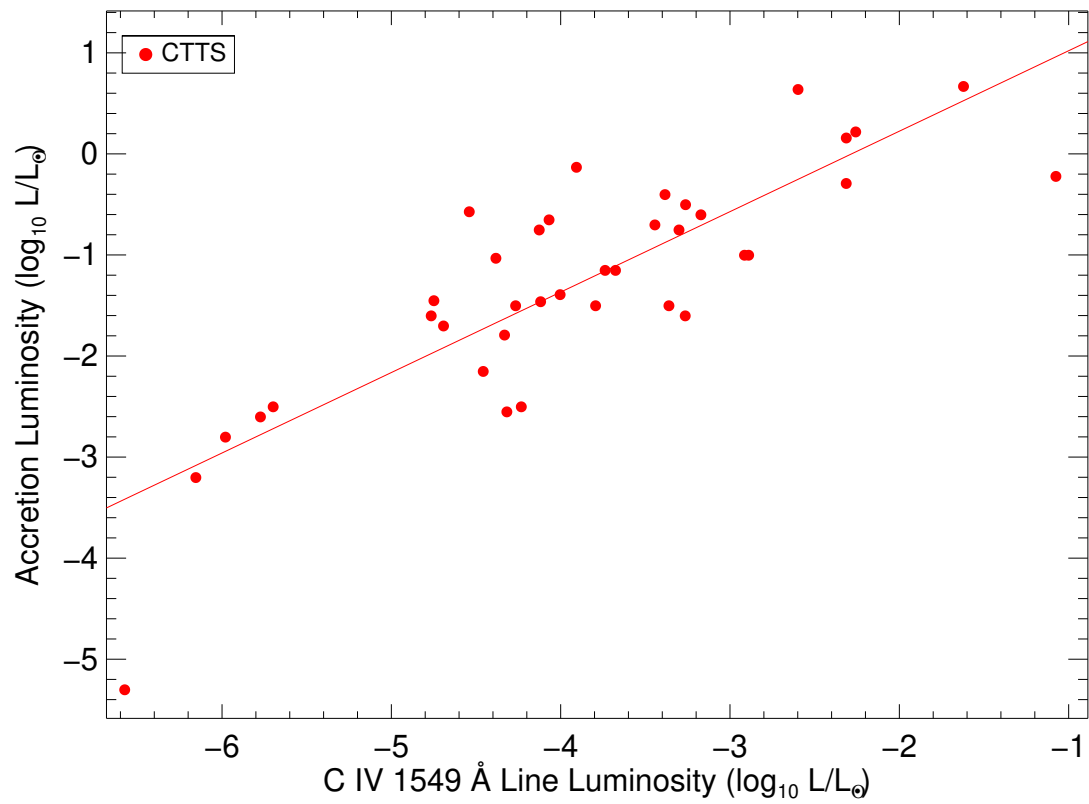


Fig. 8.— The accretion luminosity is plotted against the C IV $\lambda 1549$ doublet luminosity for CTTSs. The red solid line is the best fit in logarithmic space.

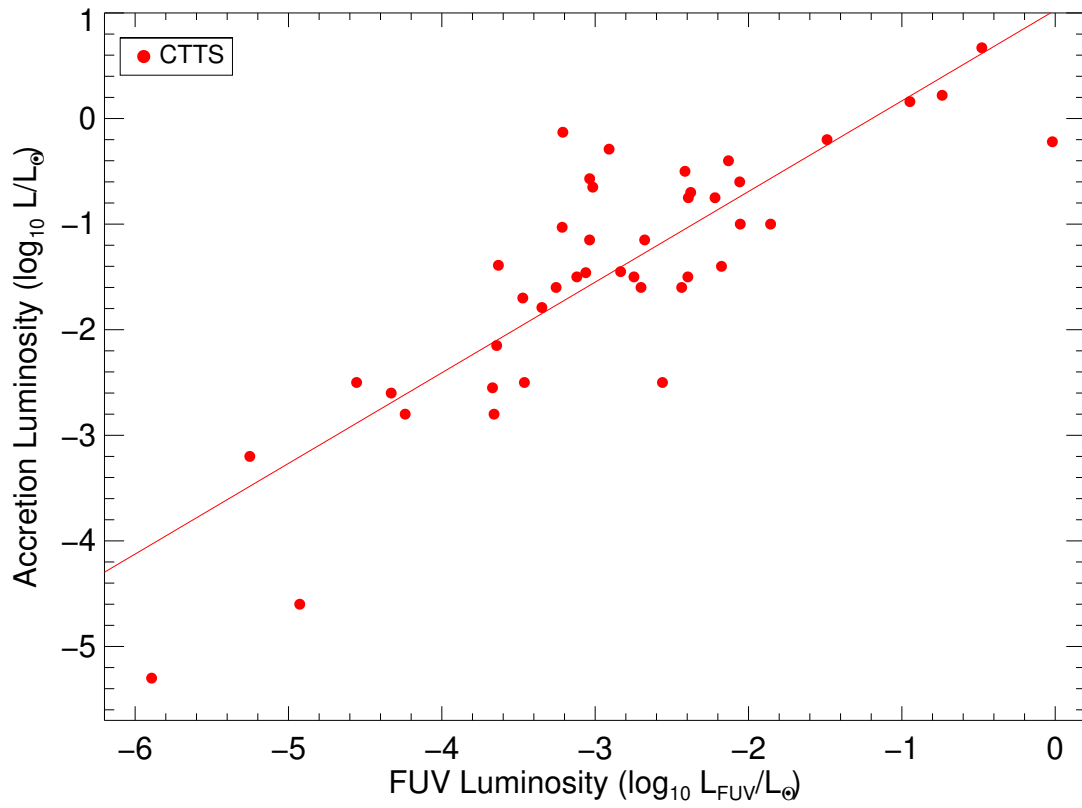


Fig. 9.— The accretion luminosity is plotted against the FUV luminosity for CTTSs. The red solid line is the best fit in logarithmic space.

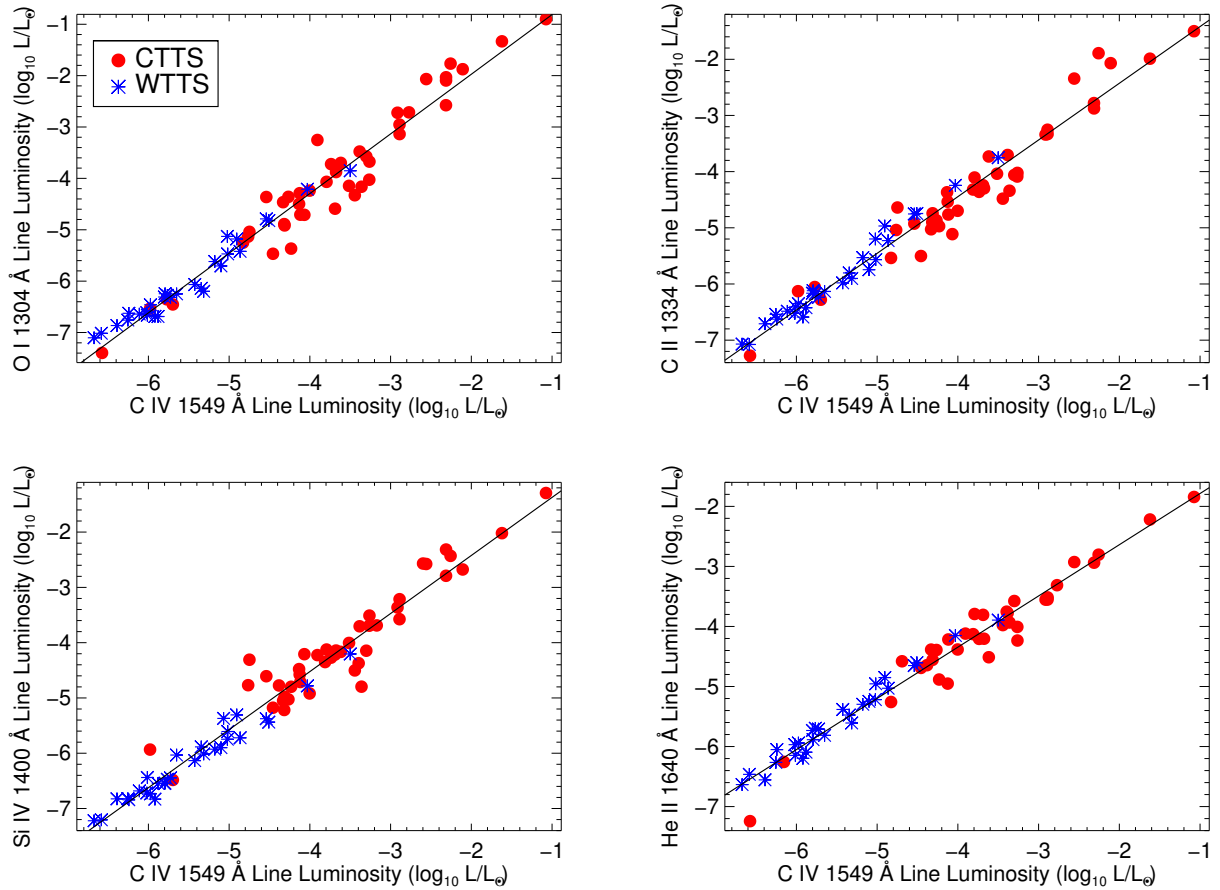


Fig. 10.— The C IV $\lambda 1549$ doublet luminosity is plotted against the O I $\lambda 1304$ multiplet, C II $\lambda 1335$ doublet, Si IV $\lambda 1400$ doublet, and He II $\lambda 1640$ line luminosities. CTTSs are plotted as red filled circles and WTTSs are plotted as blue asterisks. The solid line in each panel is the best fit to all of the data in logarithmic space.

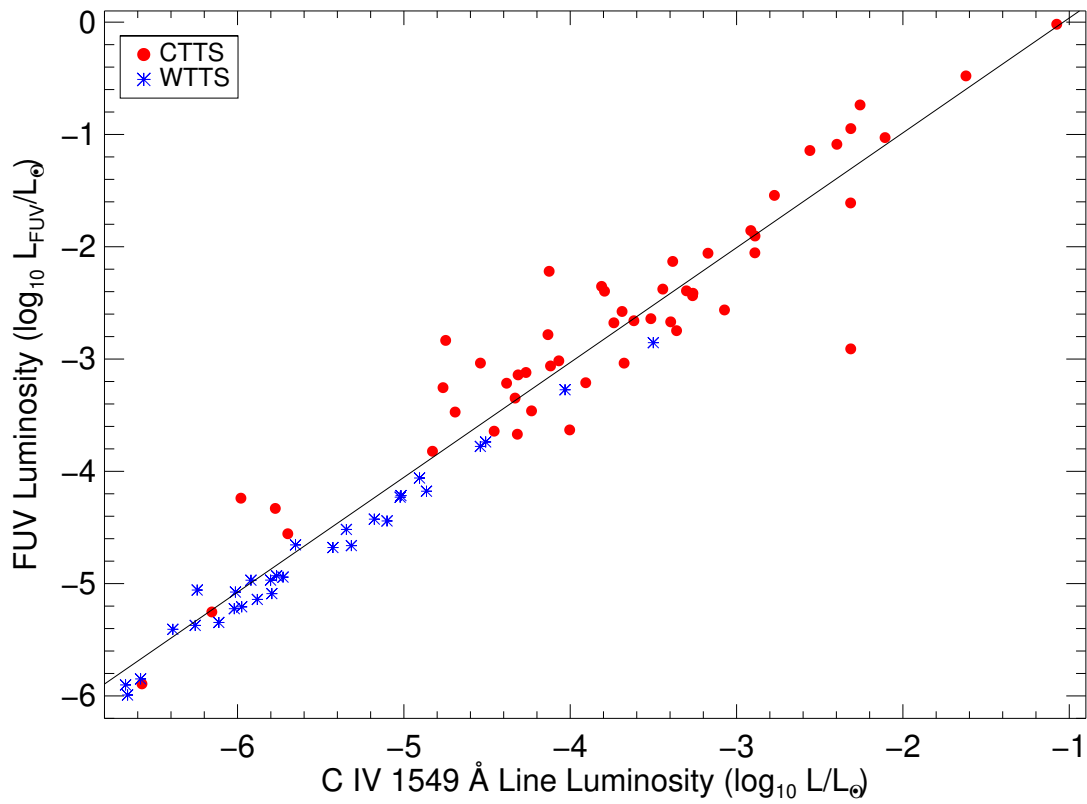


Fig. 11.— FUV luminosity is plotted against C IV $\lambda 1549$ doublet luminosity. CTTSs are plotted as red filled circles. WTTSs are plotted as blue asterisks. The solid line is a best fit to all of the data in logarithmic space.

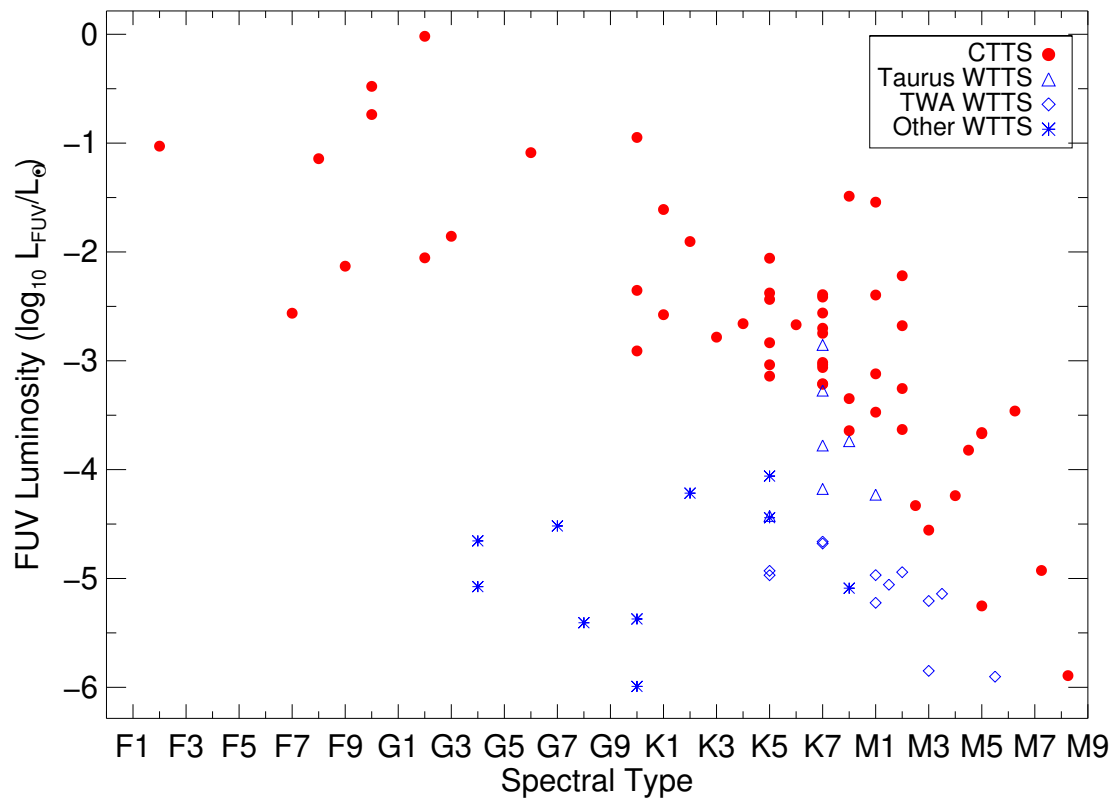


Fig. 12.— FUV luminosity is plotted against spectral type. CTTSs are plotted as red filled circles. WTTs in different regions are plotted in blue as different symbols. The triangles are WTTs in Taurus, the diamonds are WTTs in TWA, and the asterisks represent WTTs in other regions.

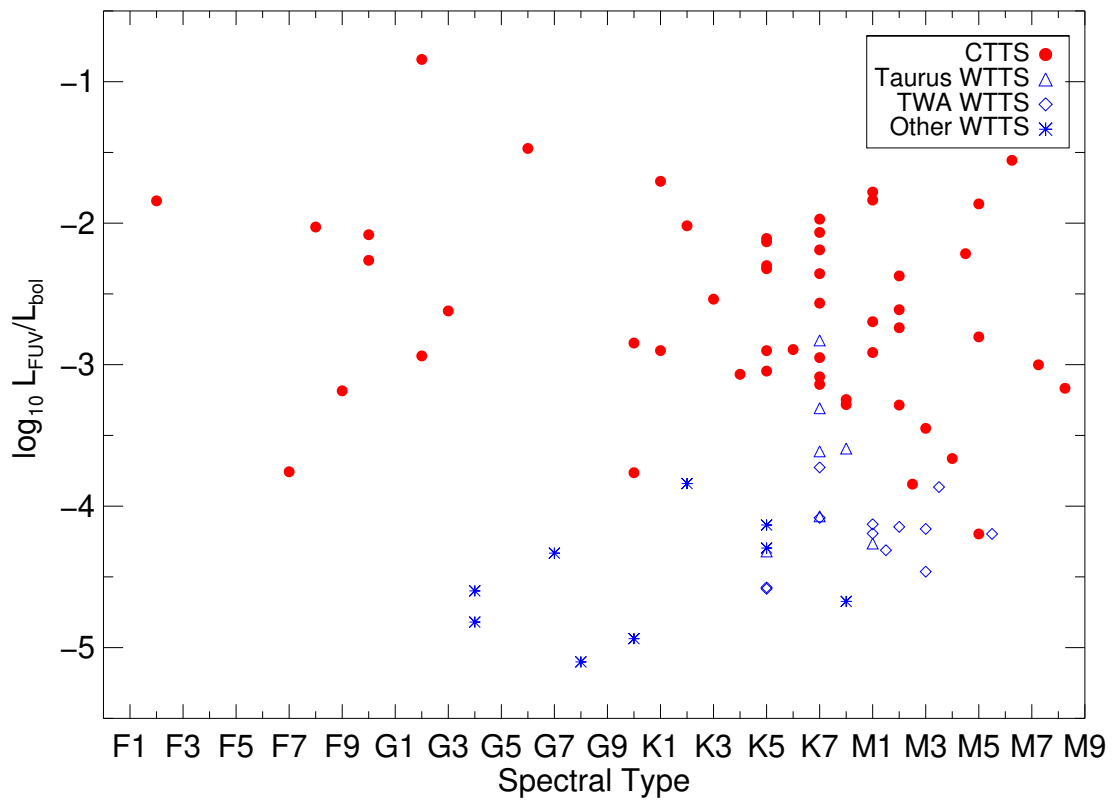


Fig. 13.— Ratios of FUV luminosity to bolometric luminosity are plotted against spectral types. CTTSs are plotted as red filled circles. WTTs in different regions are plotted in blue as different symbols. The triangles are WTTs in Taurus, the diamonds are WTTs in TWA, and the asterisks represent WTTs in other regions.

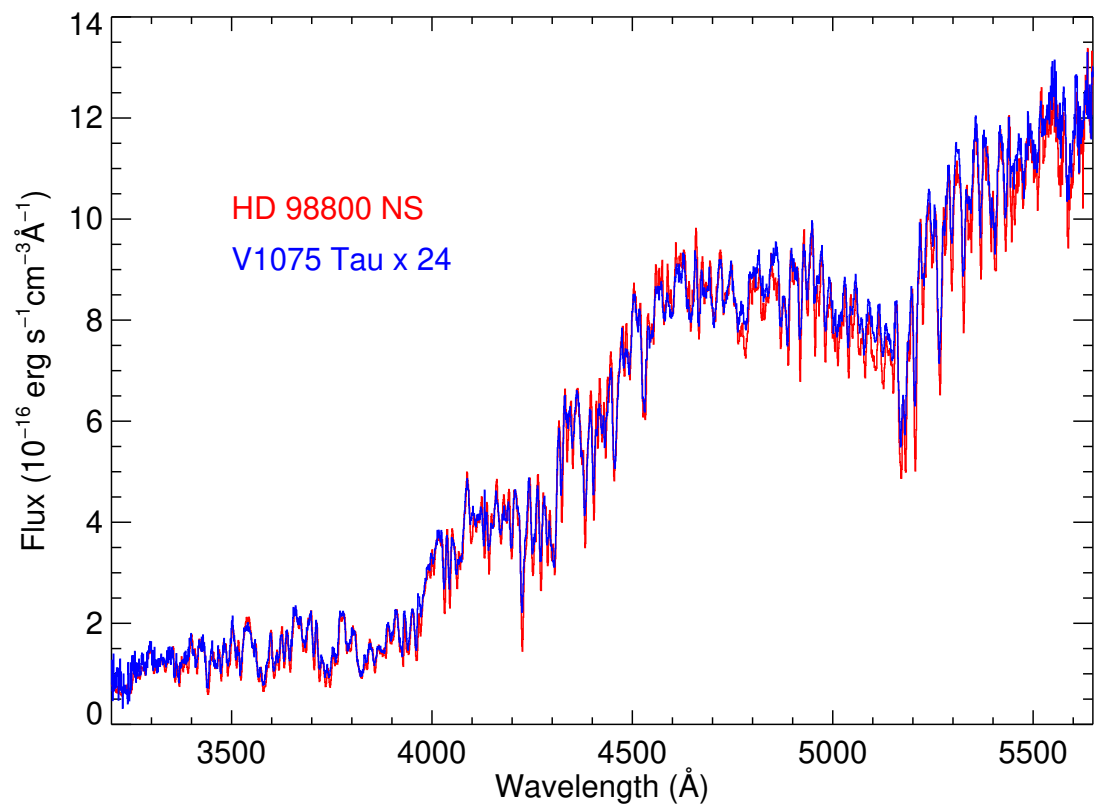


Fig. 14.— The optical spectra of HD 98800 and V1075 Tau.

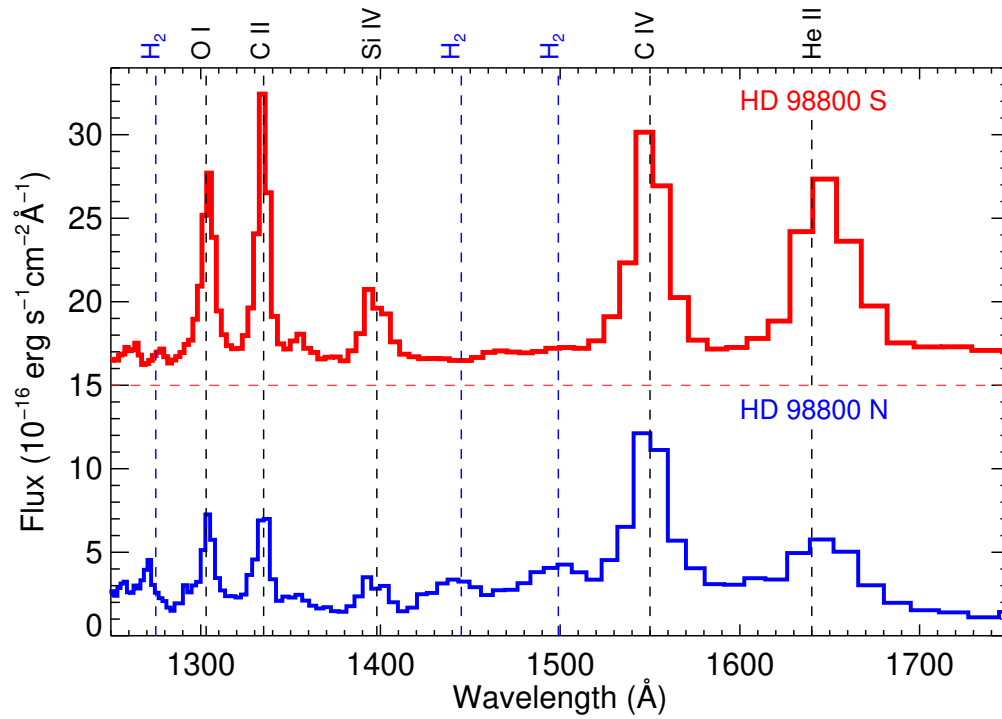


Fig. 15.— Spectra of HD 98800 N and S are shown. The spectrum of HD 98800 S is shifted by $+1.5 \times 10^{-15} \text{ erg s}^{-1} \text{ cm}^{-2} \text{ \AA}^{-1}$ for better viewing. Strong atomic emission lines are labeled, and a few H_2 emission features shown in HD 98800 N are also identified.

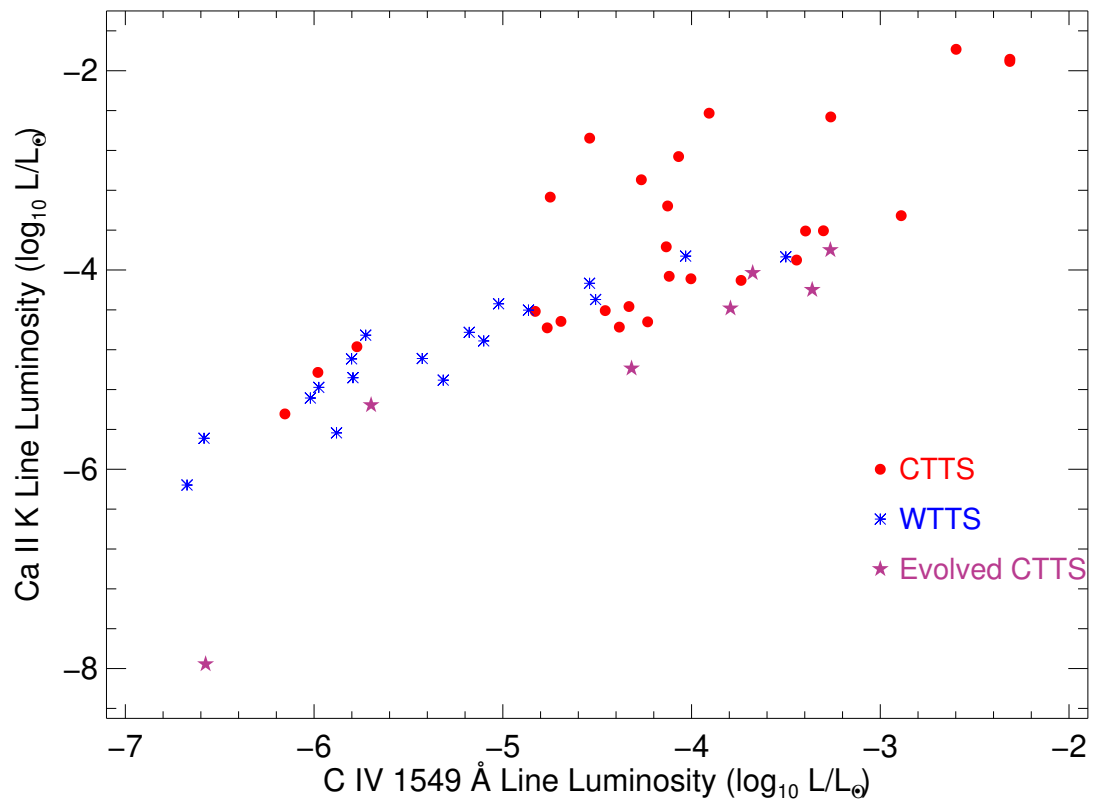


Fig. 16.— The Ca II K line luminosity is plotted against the C IV $\lambda 1549$ doublet luminosity for WTTSs (blue asterisks), CTTSs (red filled circles), and evolved CTTSs (purple stars) as defined in §4.5.

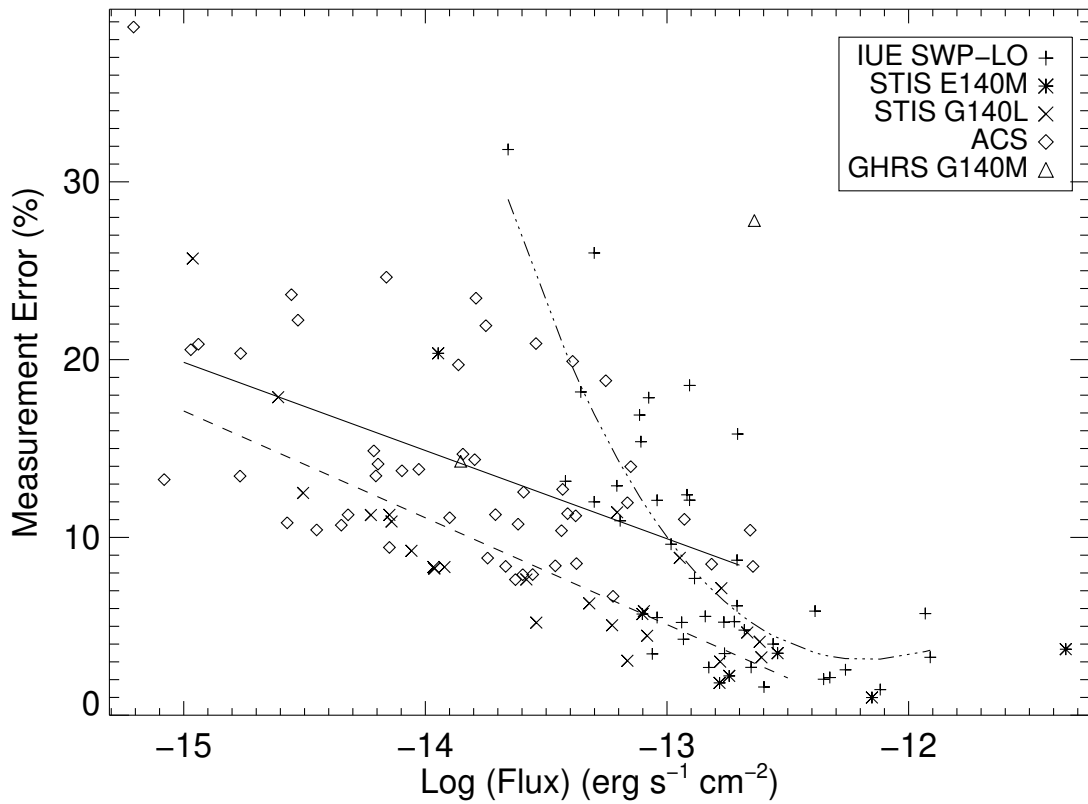


Fig. 17.— The percentage errors in flux measurements are plotted against fluxes for the C IV doublet listed in Table 4 of this work and the IUE data listed in Table 6 of Valenti et al. (2000). The different data sets are indicated by different symbols noted in the legend. The solid line is a linear least-squares fit to the ACS data, and the dashed line is a fit to the STIS G140L data. The curved line is a rough fit to the IUE data.

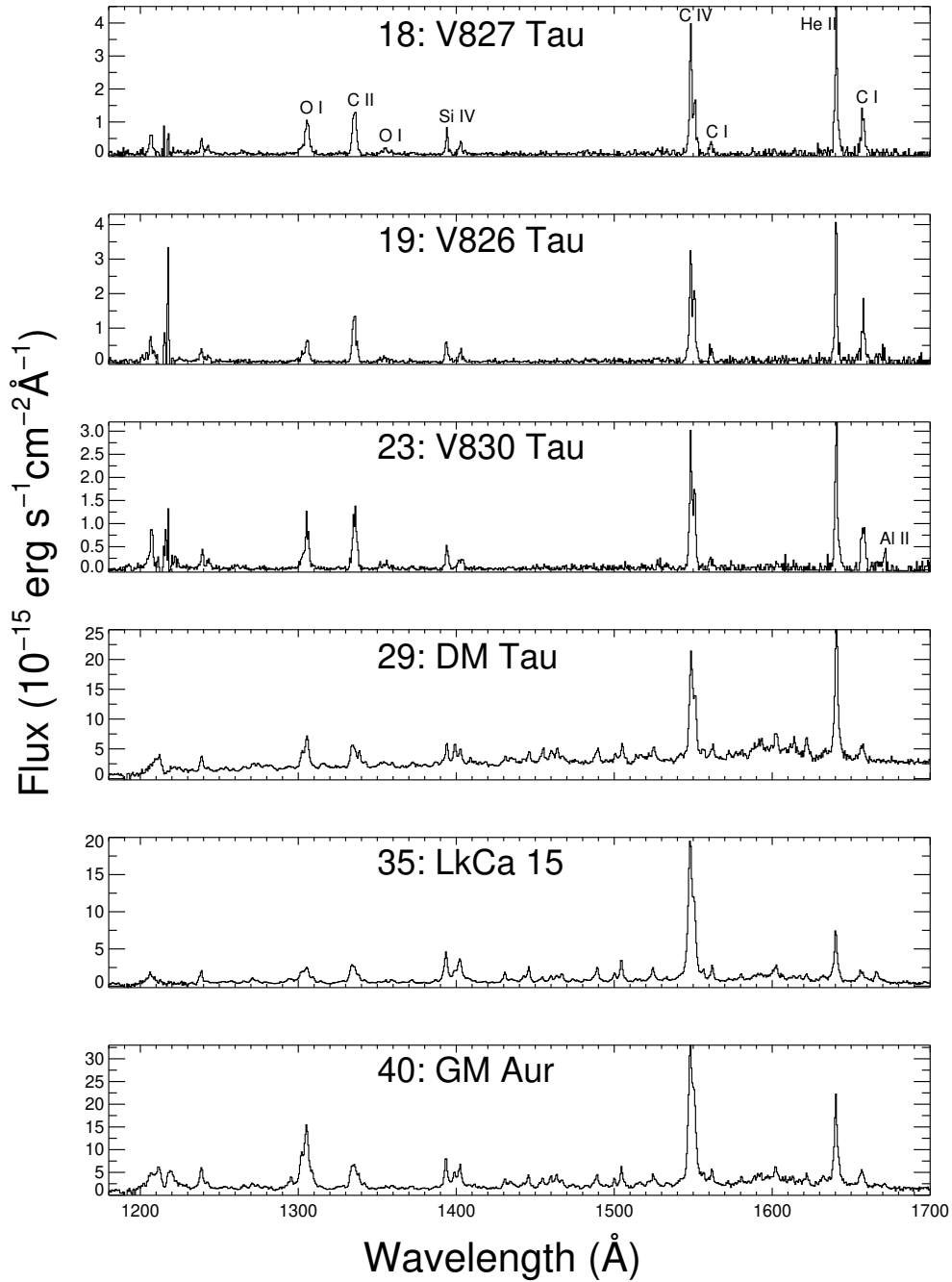


Fig. 18.— *Online-only figure STIS G140L plot 2.*

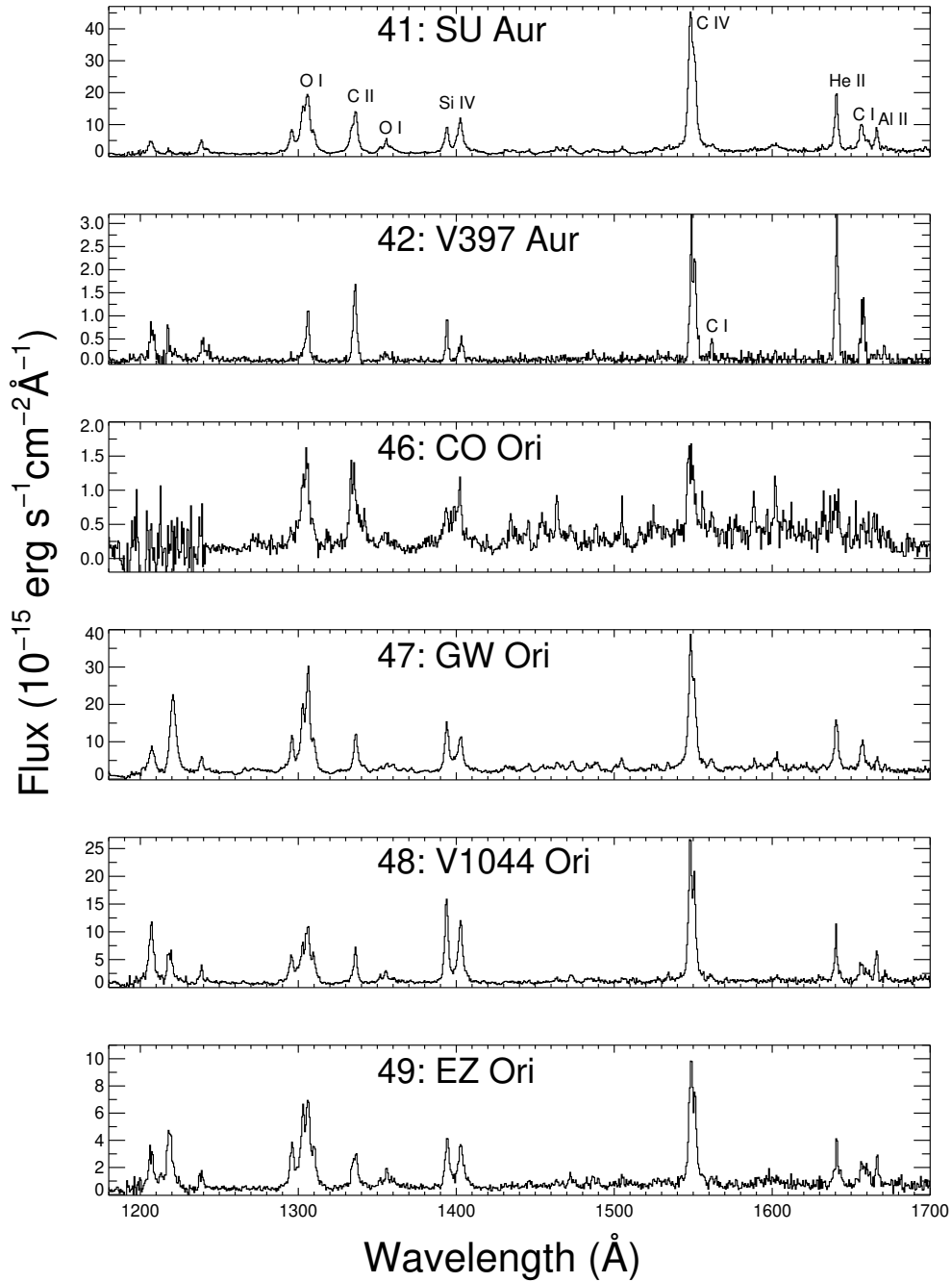


Fig. 19.— *Online-only figure STIS G140L plot 3.*

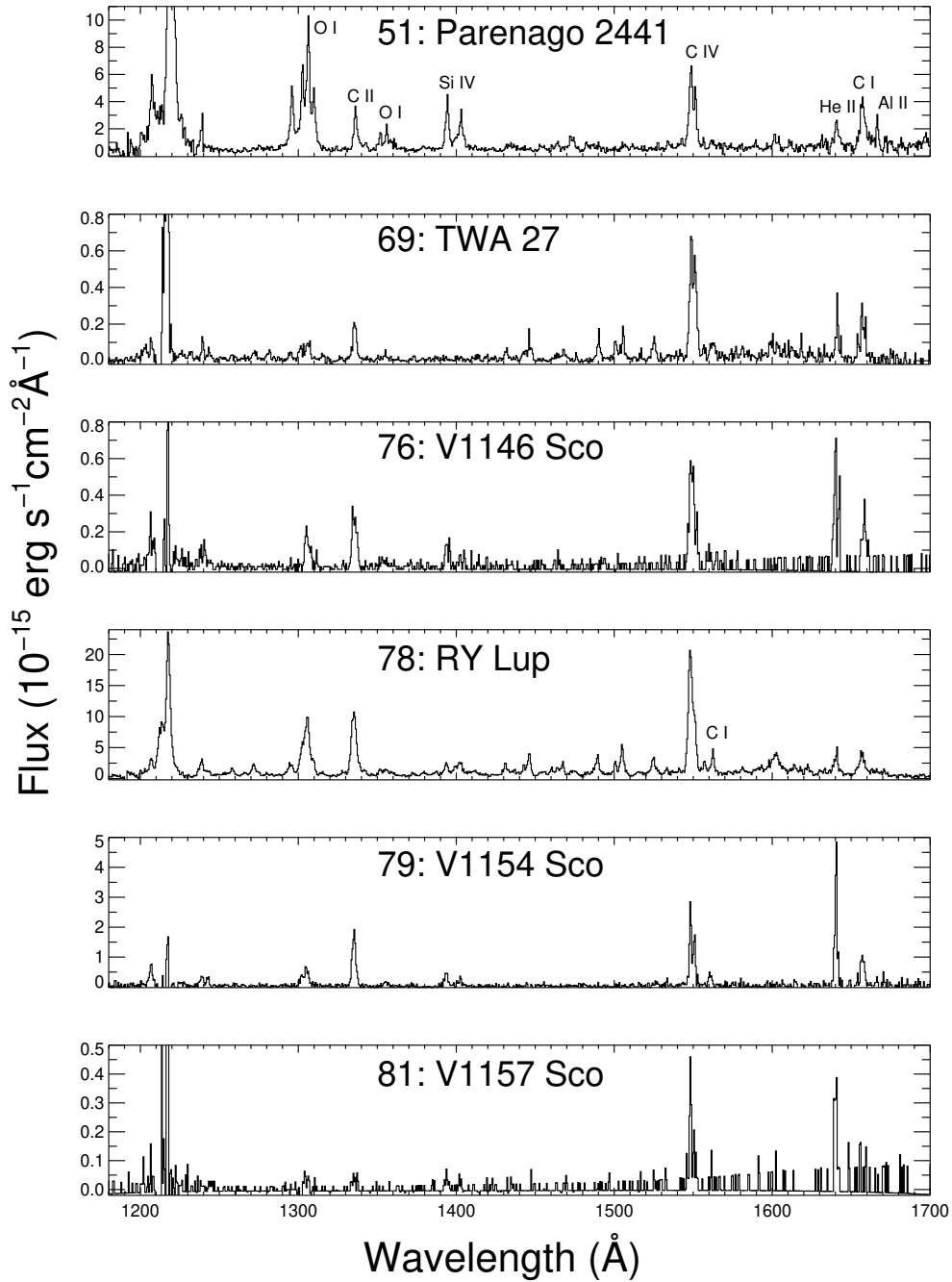


Fig. 20.— *Online-only figure STIS G140L plot 4.*

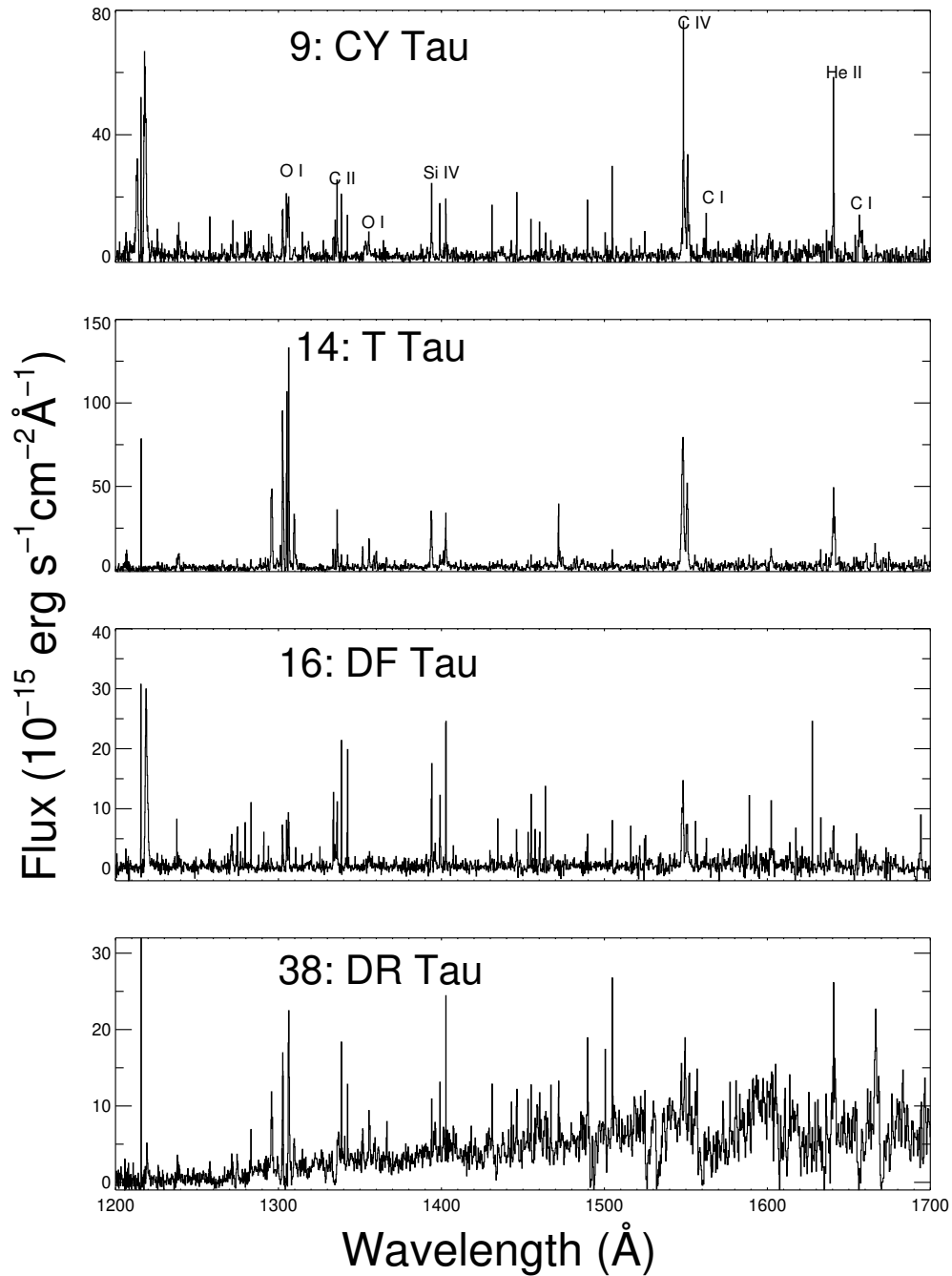


Fig. 21.— *Online-only figure STIS E140M plot 1.*

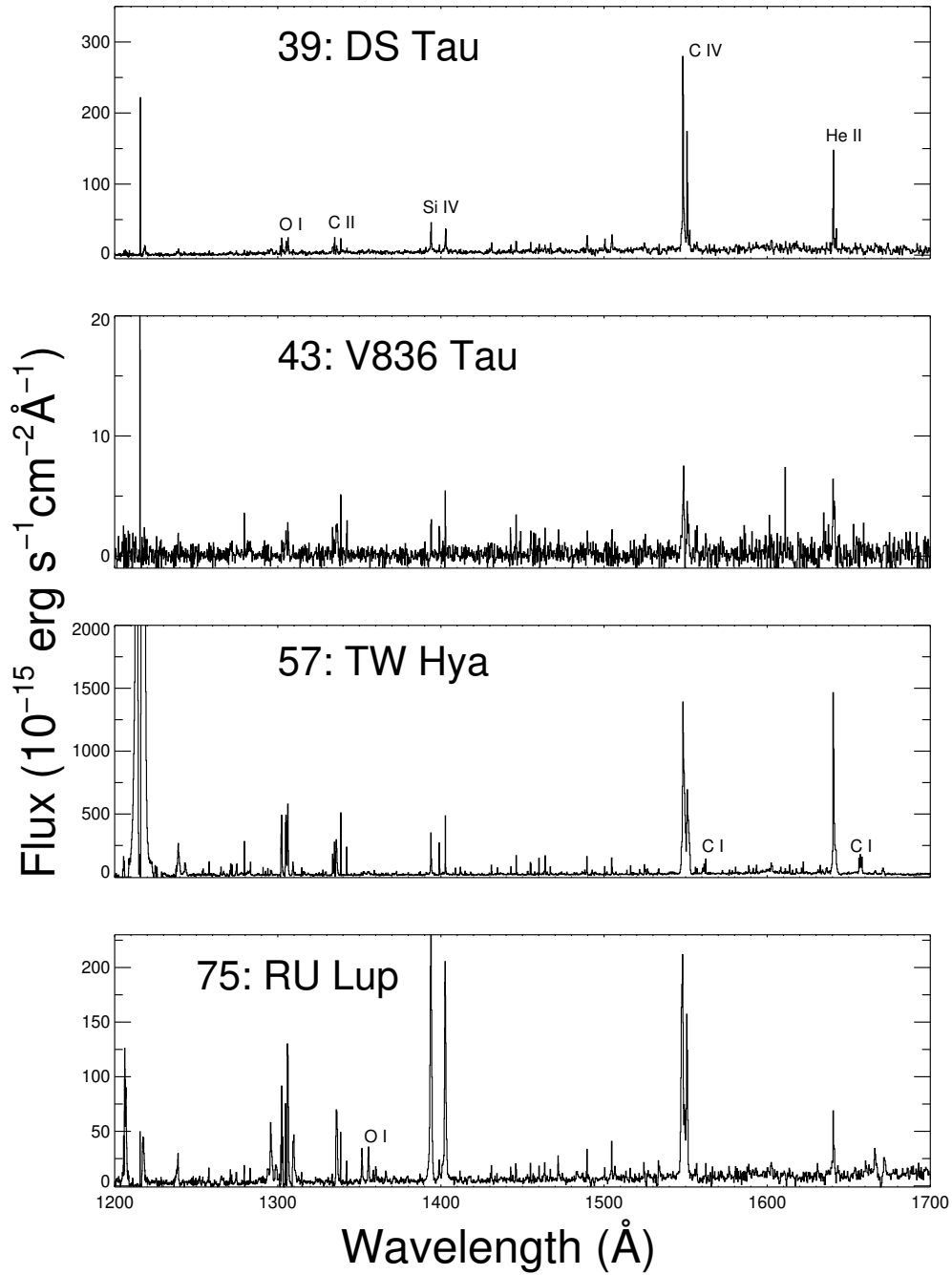


Fig. 22.— *Online-only figure STIS E140M plot 2.*

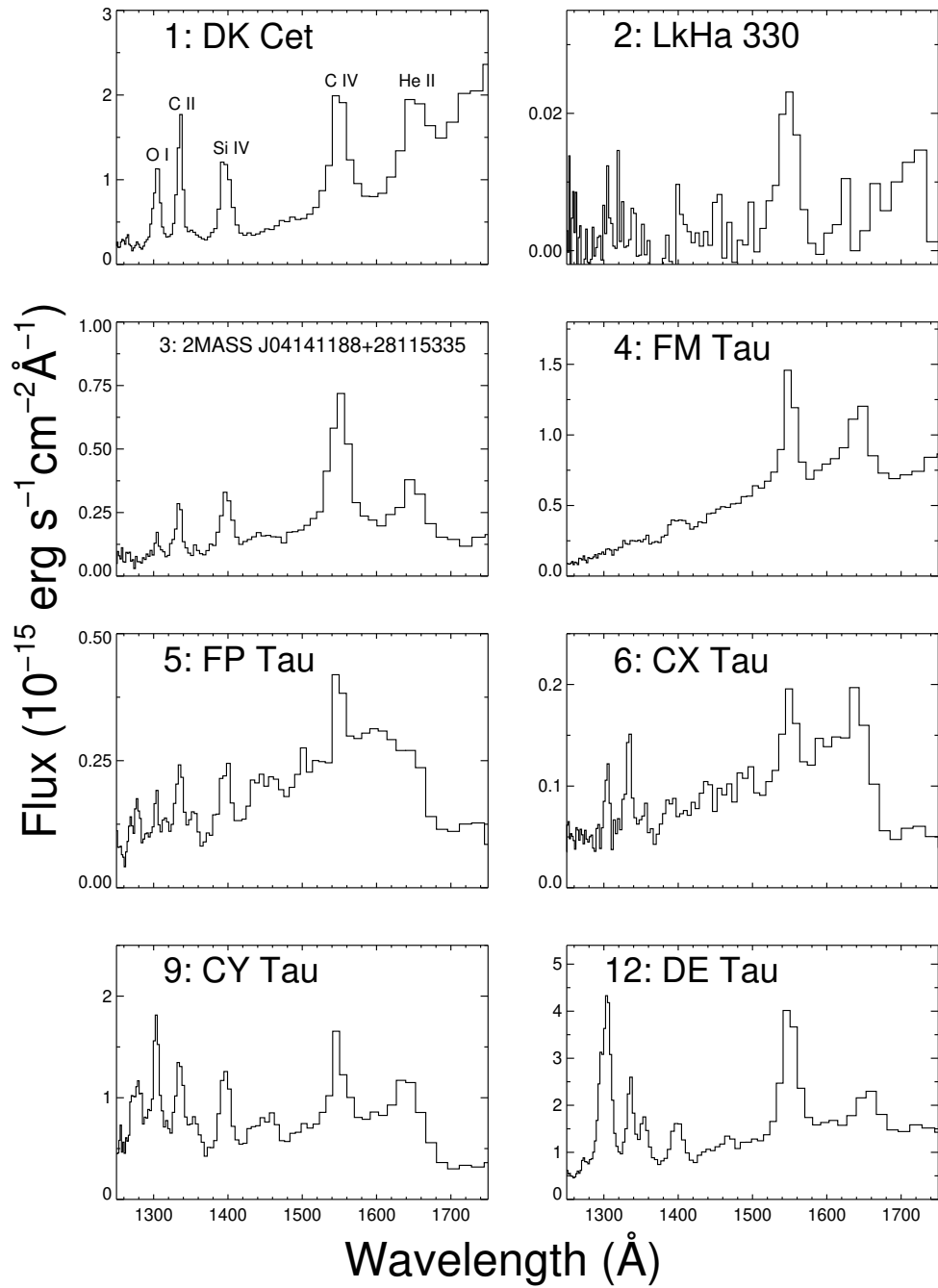


Fig. 23.— *Online-only figure ACS plot 1.*

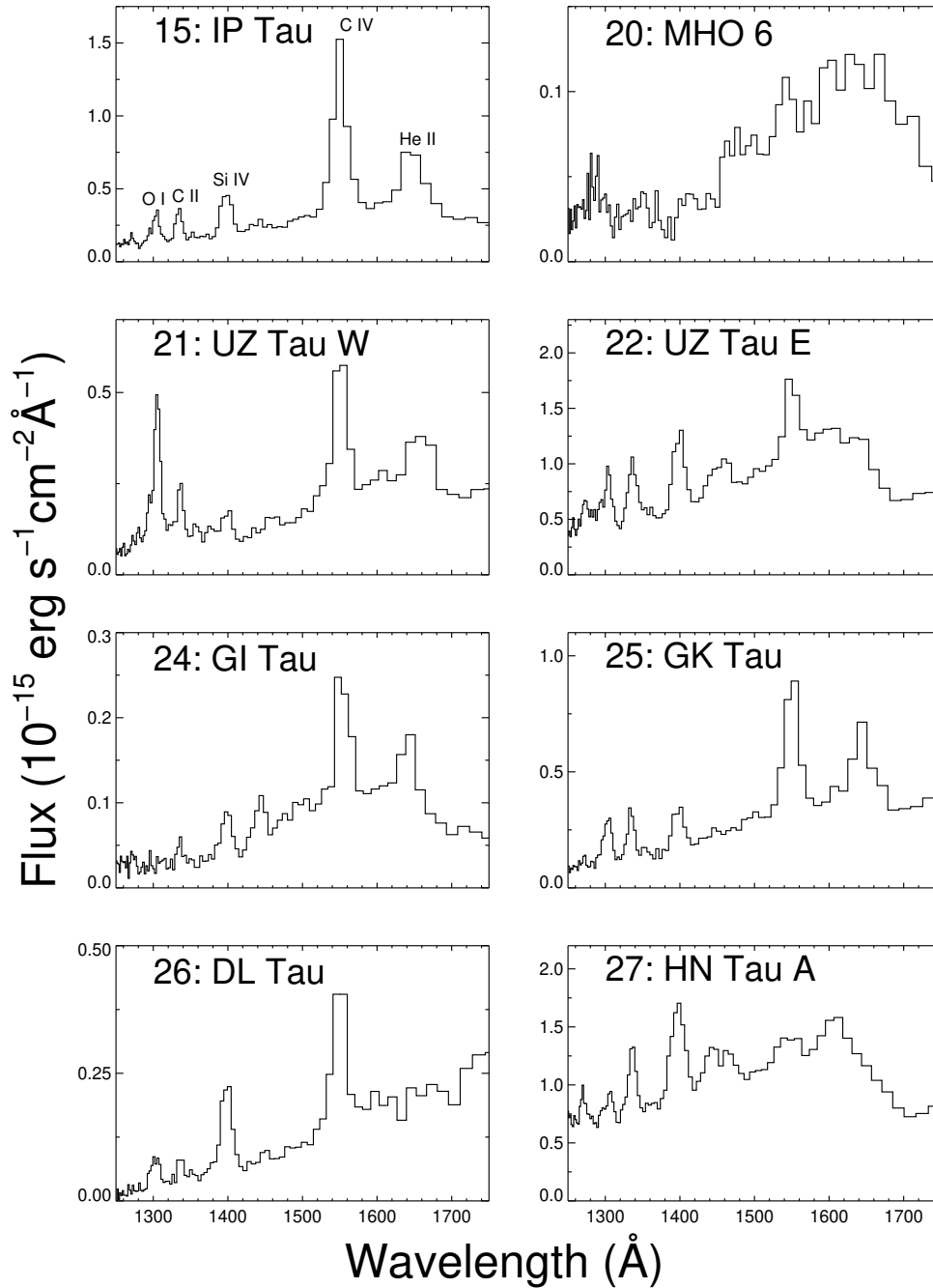


Fig. 24.— *Online-only figure ACS plot 2.*

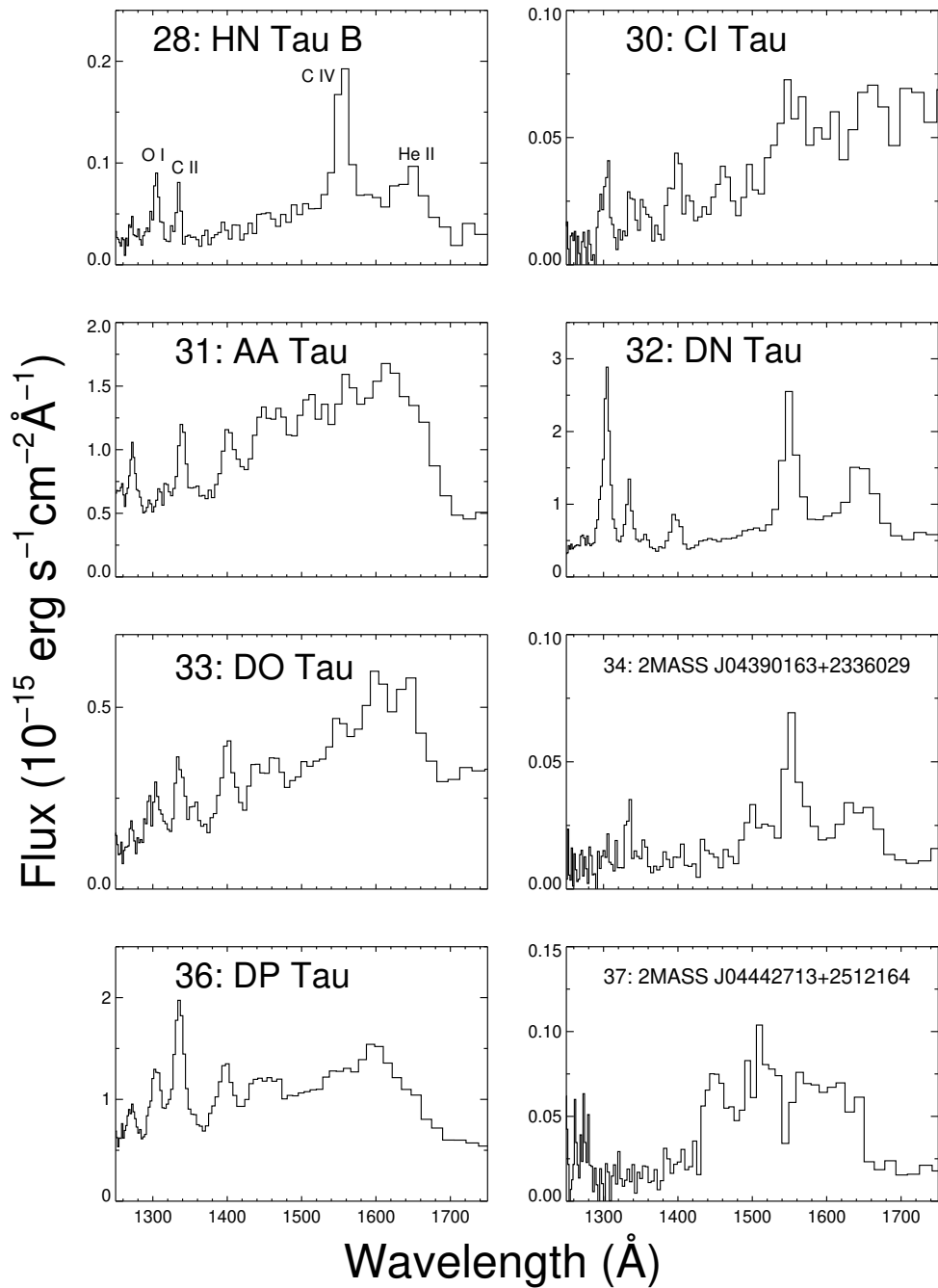


Fig. 25.— *Online-only figure ACS plot 3.*

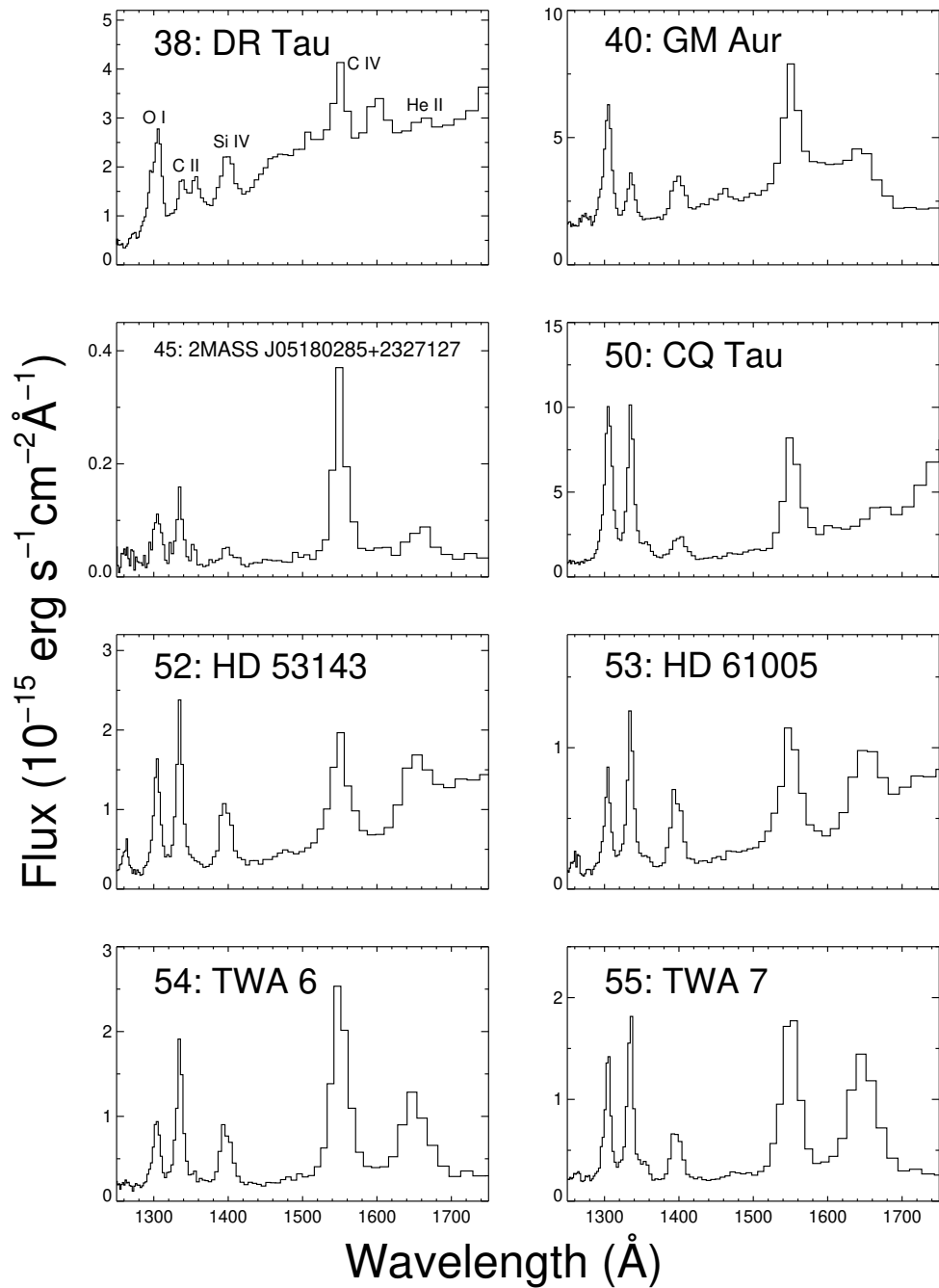


Fig. 26.— *Online-only figure ACS plot 4.*

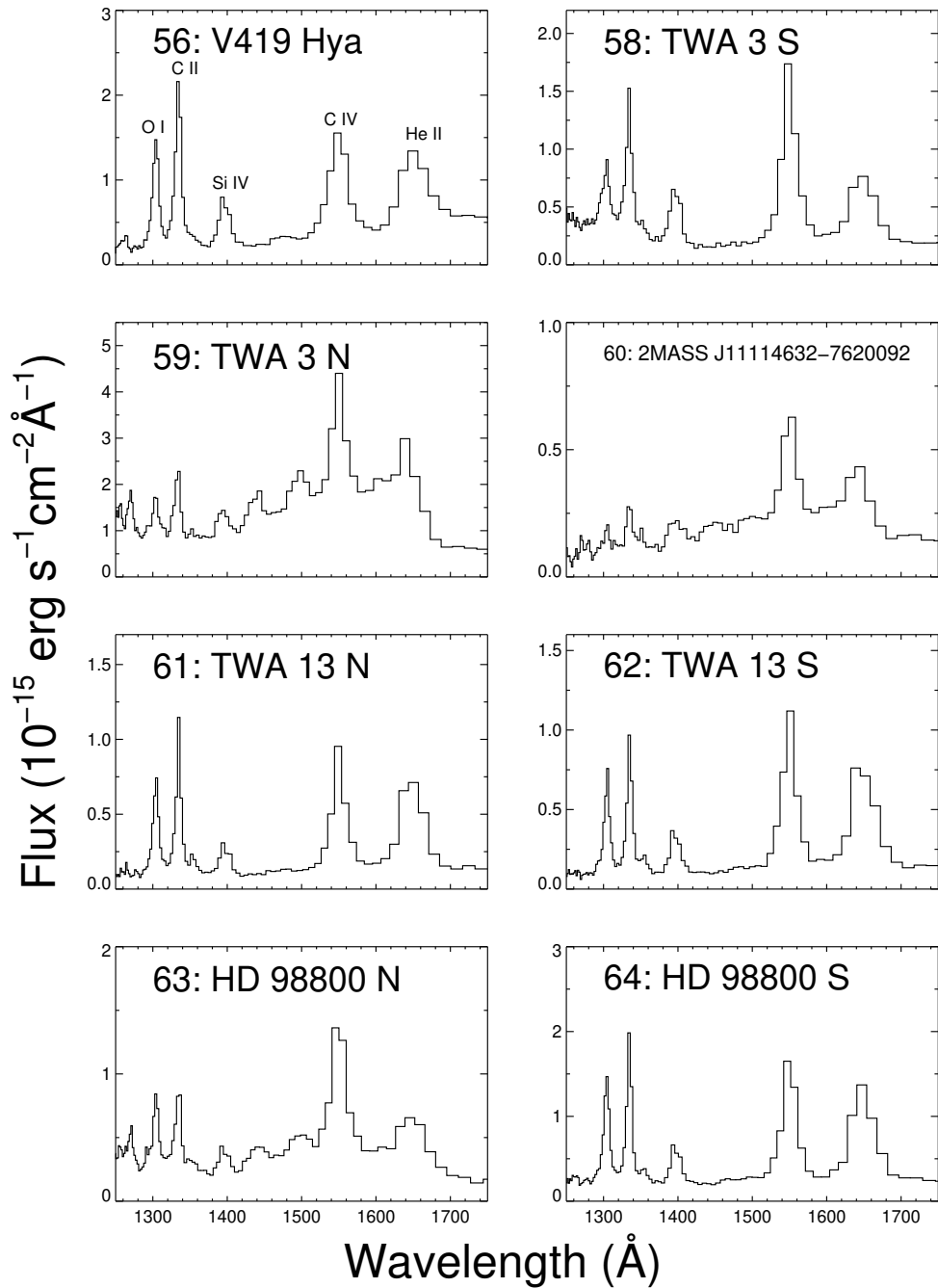


Fig. 27.— *Online-only figure ACS plot 5.*

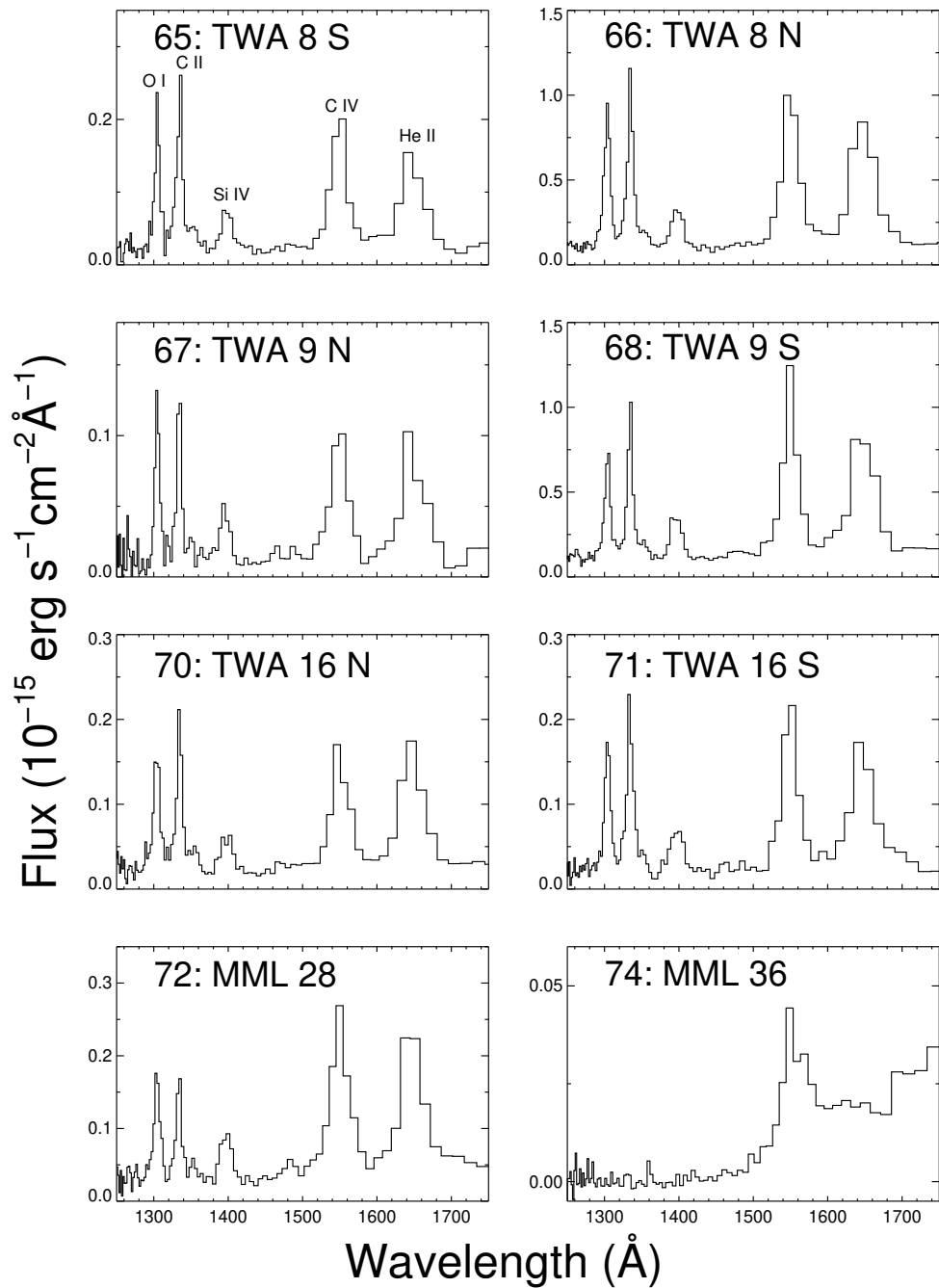


Fig. 28.— *Online-only figure ACS plot 6.*

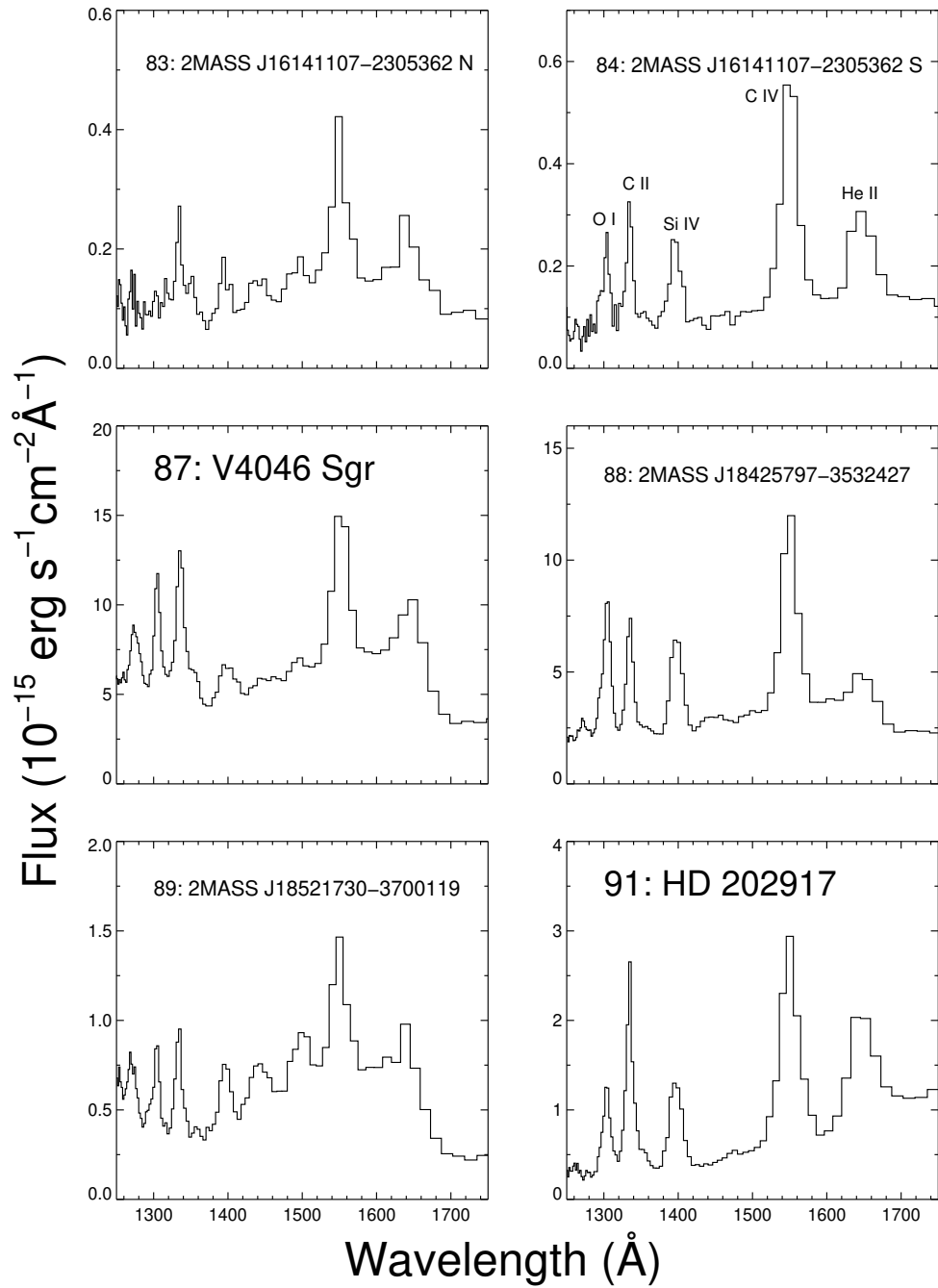


Fig. 29.— *Online-only figure ACS plot 7.*

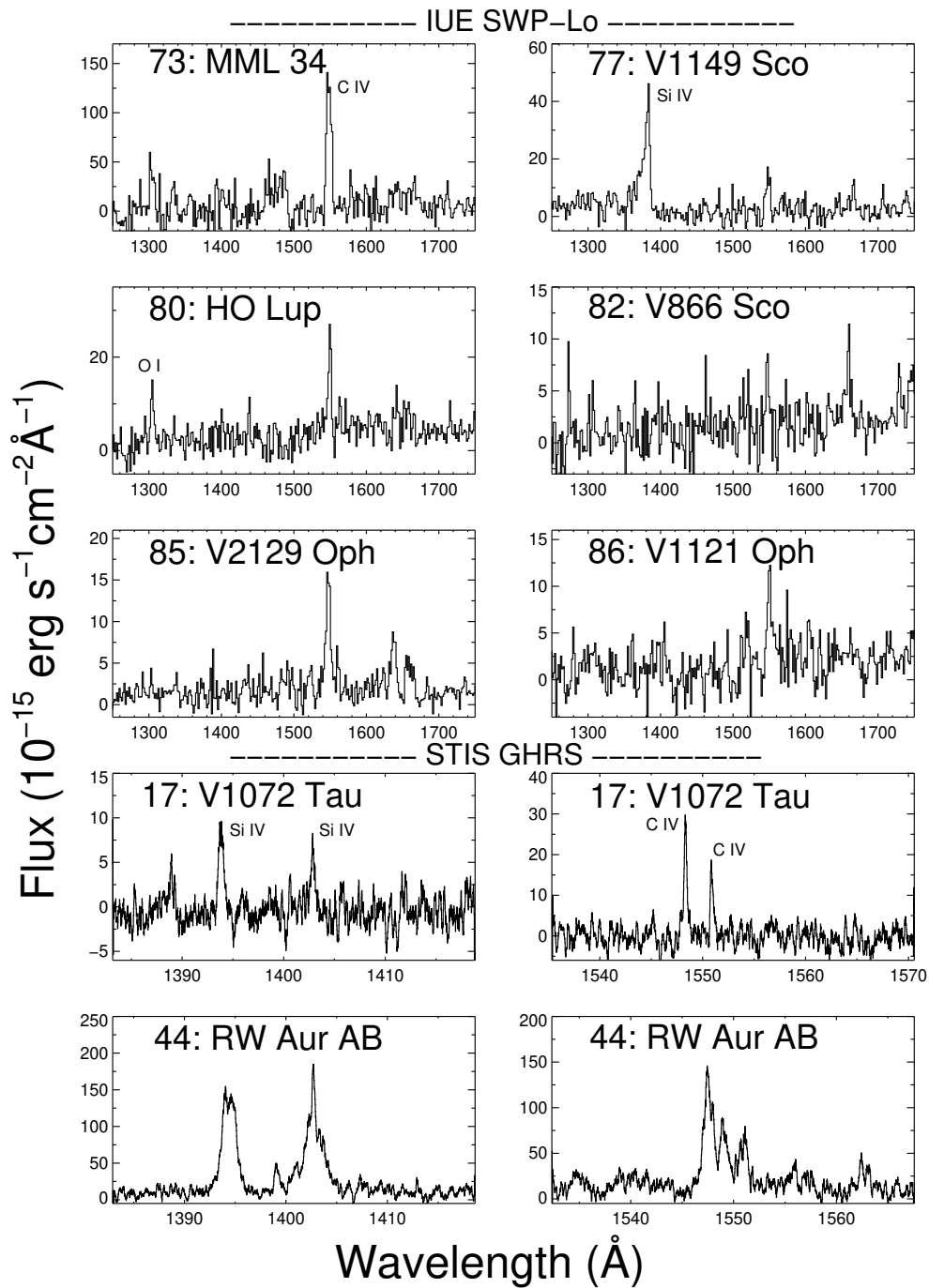


Fig. 30.— *Online-only figure* IUE and GHR5 plot.